AN INVESTIGATION OF PROTON PAIR CORRELATIONS RELEVANT TO THE NEUTRINOLESS DOUBLE BETA DECAY OF ^{76}Ge

David R. Ticehurst

A dissertation submitted to the faculty at the University of North Carolina at Chapel Hill in partial fulfillment of the requirements for the degree of Doctor of Philosophy in the Department of Physics.

Chapel Hill
2016

Approved by:

Calvin R. Howell

Arthur E. Champagne

Jonathan Engel

Reyco Henning

Sheila J. Kannappan

ABSTRACT

David R. Ticehurst: An Investigation of Proton Pair Correlations Relevant to the Neutrinoless Double Beta Decay of ^{76}Ge
(Under the direction of Calvin R. Howell)

The observation of neutrinoless double beta decay ($0\nu\beta\beta$) would demonstrate that the neutrino is a Majorana particle and allow determination of its mass by comparing the measured decay rate to the calculated rate. The main uncertainty in the calculation of the $0\nu\beta\beta$ rate is due to uncertainties in the nuclear structure models used in the computation of the nuclear matrix elements for the decay process. This project tested the validity of using wavefunctions for the nuclear states involved in the $0\nu\beta\beta$ process that are based on a first-order application of the Bardeen−Cooper−Schrieffer (BCS) theory of superconductivity. In the BCS approximation, most of the strength for two-nucleon transfer reactions should be for transitions to the 0^+ ground state of the final nucleus (i.e., little strength should go to the 0^+ excited states). This experiment measured the strength to the first 0^+ excited state for the ^{74}Ge(^3He,n)^{76}Se and ^{76}Ge(^3He,n)^{78}Se reactions relative to the strength for transition to the 0^+ ground state in selenium. For both nuclei, and at ^{3}He beam energies of 15 and 21 MeV, the observed relative strength for transfer to the first 0^+ excited state was less than 13%. This result supports the validity of using the BCS approximation to describe the ground state of both ^{76}Se and ^{78}Se and is consistent with the results of recent (^3He,n) cross section measurements on ^{74}Ge and ^{76}Ge. In addition, the magnitude and shape of the measured angular distributions suggest that contribution of the sequential two-nucleon transfer process, which is an indicator of long-range nucleon-nucleon correlations, is over-predicted by the DWBA code FRESCO.

To Lynne Lazar Ticehurst, my very own mother.

“E pala ma'a, 'ae lē pala 'upu.”

(Stones rot, but words remain.)

- Samoan Proverb

ACKNOWLEDGEMENTS

Nine years is a long time. Although my name stands alone on the title page, this work has *many* coauthors who have helped bring this 9-year project to fruition.

It would seem I was both born with a scientific mind and had science thrust upon me. My father, a virologist, was always eager to talk science and have me around his lab. One of my earliest memories is of a broken centrifuge on the loading dock of building 7 at the National Institutes of Health. It was fascinating to me because the covering was removed and I could see all the inner workings. Thus, despite my father's efforts to impress upon me the wonders of biology, even from an early age it was the physical and the mechanical that captured my attention. Nonetheless, my father is primarily responsible for watering the seed of scientific thought. He has and always will be first among my heroes.

On several occasions, I came quite close to expulsion from middle school but for the extraordinary foresight of my headmaster, Mr. James "Skeeter" Lee. Though it remains a family joke, it is no exaggeration that Mr. Lee literally had a separate disciplinary notebook devoted to me. Even after leaving his academic purview, Mr. Lee continued to both support my interests and advocate for me. He is also most responsible for my love of the outdoors. When considering all of the fine educators I have thus far encountered, Mr. Lee tops the list.

As a child I read voraciously and tinkered with every piece of machinery I could get my hands on. But my first formal physics class was not until 9^{th} grade. I was quickly enamored of this pairing of mathematics and physical intuition by my logical and subtly humorous teacher, Mr. Kurt Sinclair. I was also to take high school physics classes with Dr. Richard Brockhaus. Where Mr. Sinclair was thorough, patient, focused, and exact, "Doc Brock" was cut-to-the-chase, quick-witted, diverse, and approximating. Though different, I greatly

value the two philosophies these men taught me for doing science. I am also indebted to them both for the interest they had in me back in high school, and the interest they both continue to show in me today.

I attended Williams College largely to work under Dr. Jay Pasachoff. Dr. Pasachoff is a born and bred New Yorker with the personality to match, and a warm, generous man with a true passion for experimental astronomy. These qualities were immediately evident by his willingness to meet with me for an entire afternoon when I was (still a high school student) touring colleges, and a complete unknown to him. Under Dr. Pasachoff, I completed my first published scientific investigation (Elliot et al. [2003]), and I am deeply appreciative of his extreme patience and understanding during that difficult process. I am also grateful for his continued interest in my life and frequent communications with me, despite my pursuance of a PhD outside of astronomy.

In addition to Dr. Pasachoff, Dr. Marek Demianski and Dr. Protik Majumder recommended me for entrance into a PhD program. I am grateful for their confidence in me and for their guidance during the several courses I took with them[1]. Dr. Steven Sousa was also a wonderful source of support and guidance during both my time both at Williams and in graduate school. During the summer following my first year at Williams, I had the fortune to work under Mr. Rui Rita, from whom I learned the difference between knowledge and experience. This lesson has stuck with me throughout graduate school, because a lack of experience is the difference between a graduate student and an independent scientist. In my junior year at Williams, I enrolled in a proof-based mathematics course, real analysis, taught by Dr. Thomas Garrity. Having had no experience with this type of math, I found myself immediately over my head and with a "C-" on a math test for the first time in my life! I would have dropped this course were it not for Dr. Garrity's patience and tutelage outside of class, for many hours each week. I achieved a perfect score on the final exam. Thank you, Dr. Garrity, for proving that I can accomplish the seemingly impossible.

[1]An apology is also due to Dr. Demianski for the time I accidentally routed us through the center of New York City while he was driving us to Washington, D.C. for Thanksgiving.

Following college I had the privilege to teach physics and astronomy at Christ School, a boys' boarding school, for three wonderful years. I am particularly grateful to Mr. Erich Cluxton, the academic dean during these years, not in the least for recommending my entrance into a PhD program. Mr. Cluxton stood as a shining example of academic propriety and provided much guidance throughout my teaching years and as I transitioned to graduate school. I would also like the acknowledge the friendship and support of Mr. James Queen, the father of a student, a BBQ aficionado, a tireless conversationalist, and a brilliant chemical engineer. He has been a great friend and resource both during my teaching years and throughout graduate school.

My first year of graduate school in the fall of 2007 was a rude awakening back into the world of advanced physics. I did have an unexpected edge with a solid foundation in high school physics from both my excellent education and my teaching experience. Still, I believe my success that year came through the new friendships I developed with my peers. Many problem sets and exams were successfully completed only with the assistance of my officemate, Ms. Martina Astrua[2]. During this year I also worked frequently Dr. Raghav Chhetri and Dr. Emily Ray. My friendship with Raghav and Emily extended outside of the office and I am pleased to enjoy their friendship to this day.

I intended to continue my astronomical studies in graduate school, but I wanted experience in an outside field, and so joined the ranks at the Triangle Universities Nuclear Laboratory (TUNL) the summer after my first year. I am thankful to Dr. Hugon Karwowski for accepting me as a master's student at TUNL, and for his guidance through that project. Another peer who shared his first year of graduate school with me, Dr. Jeromy Tompkins, also joined TUNL at the same time. Jeromy's prior experience at TUNL (as his willingness to share it) proved invaluable to me as I began work in an unfamiliar field. I shared an office at TUNL for a time with Dr. Alex Couture, who wins the award for the "most redneck" nuclear physicist. Alex would frequently regale me with accounts of his

[2]This is not an admission of cheating, Ms. Astrua and I did not converse *during* examinations!

weekend activities, which largely consisted of either clearing brush or pickling and canning vegetables. Nonetheless, Alex had an excellent understanding of the tandem accelerator lab and is primarily responsible for "showing me the ropes." He also had an uncanny ability for finding mistakes in source code I had written, which prevented me from destroying several computers. My thanks goes to Alex both for the light conversation and the technical know-how.

There is widespread anecdotal evidence of the (sometimes extraordinary) efforts undertaken by PhD students to secure a desired adviser. However, after completing my master's project, Dr. Calvin Howell, a member of my master's committee, stopped me outside of the lab on a sunny fall day to praise my work and ask if I would complete my PhD under his guidance (frankly, I had not thought myself a student of high enough caliber to request his advisership). That simple act is revealing of Dr. Howell's character; he is an astoundingly patient, humble, and selfless man. He is also a consummate experimentalist and a superb teacher with a genuine, unquenchable interest in science. Despite the normal demands made of a Full Professor compounded with the additional duties of lab directorship, Calvin could frequently be found working in the lab alongside his students. On many occasions, I was the frustrated student who Calvin was aiding. I can honestly recall several times when I would have quit out of confusion or frustration were it not for Calvin's passion and perseverance. There is no other person more responsible for my completion of this project. I can only hope that someday I will positively impact another to an extent approaching the positive impact that Calvin has had on me.

I also wish to thank the rest of my PhD committee for the time and effort they each put into conducting my oral examinations, reading this dissertation, and providing helpful feedback. Dr. Art Champagne was also of great assistance with the various bureaucratic procedures required of a graduate student. And since his office was next to mine, I would find myself immediately relaxed on the frequent occasions when Art would play his guitar. Dr. Jon Engel also endured numerous discussions of quantum and nuclear theory with me,

from frequent office visits during first-year quantum mechanics to emails and phone calls during the writing of this dissertation. Dr. Reyco Henning also served on my master's committee and made a particular effort to help improve the clarity of this document. I want to especially thank Dr. Sheila Kannappan. As an astronomer, she was the only member of my committee without a nuclear physics background, and I greatly appreciate her willingness to dive into an unfamiliar subject.

Dr. Albert Young and his student Mr. (Dr. in a few months...) Dustin Combs from NC State University joined the (^3He,n) group in 2011, rounding out the team as a true collaboration between the major triangle universities. Albert has been a source of many new ideas and much assistance during this project. Dustin led the design and construction of the ^{3}He recovery system and the neutron detector efficiency measurements. He is responsible for much of chapters 4 and 6, which pertain to these topics. I also owe Dustin an immense debt of gratitude for taking up the slack when I became too frustrated or exhausted to continue on. In the late hours of the night when I found myself no longer able to follow Calvin around the lab, Dustin was right behind him. When I threw up my hands in exasperation while tuning the accelerator and went outside for a walk, I would return to find Dustin at the controls.

Dr. Alex Brown from Michigan State University performed the DWBA calculations for the ^{74,76}Ge(^3He,n)^{76,78}Se reactions. I am well aware that this was no simple task: both Dustin and I found ourselves completely and utterly lost while attempting these calculations.

Many other people made direct contributions to this project: Mr. Ron Malone, Mr. Forrest Friesen, and Mr. Brent Fallin are all graduate students who "took shifts" on the accelerator while data was accumulating for my experiment. Because the accelerator is run around the clock during experiments, most of these shifts took place in the late hours of the night. I especially appreciate the interest these three had in my work; instead of simply "babysitting" the accelerator, they took the time to understand the "how" and "why" behind my experiment. Dr. Alex Crowell, Dr. Mohammad Ahmed, and Mr. Bret Carlin

were primarily responsible for setting up and maintaining CODA on my DAQ. Each of them has also provided invaluable computing advice during my time at TUNL. Dr. Werner Tornow provided advice and assistance with the neutron detectors, particularly the efficiency measurements. Werner has also been a great source of general nuclear physics knowledge since the very beginning of my graduate career. Dr. Tom Clegg lent us his expertise in ion particle sources, particularly the helium-ion source (HIS), on several occasions. Dr. John Wilkerson of the MAJORANA Collaboration donated a piece of enriched ^{76}Ge which was used to produce targets for the ^{76}Ge(^{3}He,n)^{78}Se measurements. Mr. Kris Vorren, also of the MAJORANA Collaboration, provided a large amount of neutrino-related information that I used in chapter 1. The design for my target storage box was based on a design by Dr. Johnny Cesaratto.

The technical staff is the backbone of any laboratory, and this project wouldn't have had a leg to stand on without the technicians at TUNL. The entire technical staff provided general assistance throughout this project, but I would like to acknowledge several individuals. Mr. Chris Westerfeldt has, by far, received the greatest number of requests I've made in my time at TUNL. From providing the lab with cold drinks when the air conditioning broke in the summer of 2008, to digging up old documentation on the HIS in 2011, to ridding my office of ants in the fall of 2016, Chris has always responded to the multitude of requests he receives with prompt attention and zero complaint. Mr. John Dunham spent countless hours maintaining and improving the HIS, and always with good humor. Mr. Paul Carter and Mr. Mark Emamian were instrumental in surveying the new 70-degree beamline. Mark also provided assistance with CAD software. Mr. Richard O'Quinn installed many new water lines and electrical outlets. Mr. Bret Carlin is primarily responsible for the new cable runs made. Mr. Marty Johnson made several difficult welds on the beamstop assembly and capacitive pickoff unit. It was always a pleasure to work with the guys in the Duke and UNC instrumentation shops. Mr. Steve Medlin, Mr. Bernie Jelinek, Mr. Richard Nappi, and Mr. Phil Lewis not only built all the various components I designed to make this experiment

possible; they taught me how to use machine tools and were always ready for a conversation about graduate school, motorcycles, or life in general.

I am much obliged to staff assistants Mr. Matthew Paul and Ms. Brenda West for not only the parking passes, reimbursements, photocopier assistance, etc. Their bonhomie brightened many of my days.

I had the pleasure of working with Dr. Moshe Gai in 2015 both at TUNL and at the Hebrew University in Jerusalem. For a number of reasons, Moshe is a living legend. Moshe has remained in communication with me and advocated for me since our work together. Simply put, it is a tremendous honor to receive advocacy from a legend.

Much of my LaTeX knowledge along with the template for this document comes from many communications with Dr. Keegan Kelly, who earned his PhD earlier this year. Thank you, Keegan, for passing along your knowledge, samples of your dissertation, and the inspiration for the style of these acknowledgments.

So far I have acknowledged the people who have directly played a part in my training as a scientist. Many others have indirectly supported me through the 9 long, frequently difficult years of graduate school.

By some twist of fate, my time in graduate school has been characterized by an extraordinary group of roommates. At the top of this list is Mr. Francois Budin, with whom I lived for more than 5 years. Francois is the most honest person I know; in our time living together I never observed him to take a single mean or remotely dishonest action, despite the slings and arrows of life. His friendship and considerate nature got me through many tough times, and I sincerely look forward to a life-long friendship with him. I owe a debt of thanks for the friendship and daily support of several other roommates: Thank you to Dr. Adrian Serohijos; I will never forget watching the election of Barack Obama with you in 2008. Thank you to Dr. Manuel Fischer; I will always remember our epic fondue party. Thank you to Dr. Steffen Wohlgemuth; if I ever forget you running around the apartment wearing a Mardi Gras mask and a red headlamp, there are plenty of pictures to remind me.

Thank you to Dr. Jean Tyrell; I will continue to impress others with the many Irish drinking songs we learned together. Thank you to Mr. John Clark; your pep talks and understanding made a real difference. Thank you to Dr. Jay Stringer and Ms. Candy Stringer;, I will always treasure the wild times we had with Mango, particularly sledding in the street after the ice storm of 2016. Thank you to Ms. Sofia Tenorio Fenton; I'm sure we'll both always remember traveling to work together on my scooter, right up to the front door of the Environment Hall! Thank you to Mr. Zaheer Abbas; who I first met when we were both starting graduate school, and with whom I've had the pleasure of reuniting as we both finish our PhDs.

I entered graduate school at UNC-Chapel Hill along with two of my former high school students, who were entering as undergraduates. Over the years, my association with Mr. Austin Eschenbach and Mr. James Locke II (the son Mr. James Locke, a highly generous and affable man himself) transitioned from a student-teacher relationship to the closest, most love-filled friendship I've ever had. We have been through life, death, and many good times together. These men have seen me at my lowest point and never failed to help lift me back up.

Many other friends have helped to bear the burden of graduate school. Mr. Bill Massengale and Ms. Sally Massengale, the parents of another student of mine, have been dear friends and advocates from my teaching years to the present. In addition, they selflessly gave their time to proofread this dissertation. Dr. David Pickar has been a dependable source of caring with honesty and honesty with humor. My fellow nuclear physicist and friend Mr. Kris Vorren has shared many river adventures, traveled with me on many road trips, and always stood by me through many rough times. Ms. Ava Pope has been a fierce friend for the past five years and I so admire her cheerful, adventurous nature. I also admire a person who is willing to confront a friend who is in the wrong, and for this reason I hold Mr. Mike Newsome in high regard. Mr. David Iberkleid was a constant companion and conversationalist during his master's program at UNC-CH, with whom I seriously considered

quitting graduate school to open a fast-food restaurant. Ms. Melissa Witmer has been a continual source of caring and support over the past three years. I thank Dr. Beth Knight for her unwavering resolve in my ability to complete this dissertation- and her reminders of it when completion was obscured from my sight. Dr. Mike Gammon and Dr. Pat Gammon, the latter my mother's childhood friend, generously opened their house and their hearts to me throughout the PhD process. Writing this dissertation has been infinitely easier with the friendship and strength of Ms. Sasha Green.

Family. It has been said that in life, there are only two certainties: death and family; and in death, there is only family. I believe this to be a basic truth, though my family is more than blood relations.

My life-long relationship with Francis and Yvonne Perry began as would be common between nephew and aunt/uncle, but evolved to that of trusted confidants with great mutual respect. One might even say "consigliere."

Al and Cathy Kapikian have been in my life from the beginning through my father's work. Through them I have learned of the wonderful juxtaposition of science, art, and family. I greatly miss Al, but I hold his memory in my heart (and his baseball) and cherish my continuing relationship with Cathy.

My Godmother and aunt, Karen Callan, has always given her full support and never forgotten me on Christmas, my Birthday, or any other important occasion in my life.

My grandparents have been tremendous sources of wisdom and love, and I feel tears well up in my eyes as I write this. From the day of my birth, Helen devoted her very existence to my success and happiness (though I must concede that later on I had to share her with her other grandchildren). I did not know Joseph well, but I always felt his love and knew that he had continual faith in me. To Robert and Alice I owe my valuation of knowledge, wisdom, and independent thought. Ken and Dorothy are my pillar, the foundation on which I was raised. Oveta is the very embodiment of selflessness, generosity, and blind, unconditional love.

"Family" immediately brings to my mind an image of Lynne, my mom; John, my dad; Kathryn, my sister; and Michael, my brother. They are the core of my being and my reason for existing against the absurdity of life. Thank you for being my family, for being the people that make my life worth living.

B.B. King once wrote "Nobody loves me but my mother." From a mathematical standpoint, my mother's love is so great (i.e., $\gg$), that this might as well be true for me as well[3]. Everything else pales in comparison. In recognition of her love, and the innumerable actions by which it has been demonstrated, I dedicate this entire work of 9 years to my mother.

Nine years is a long time, but nine pages is sufficient to give only cursory acknowledgments to a small subset of all the excellent people I have known over that time. I hope that this section adequately acknowledges those who have made a contribution to my training as a scientist. I sincerely apologize to anyone I have forgotten.

This work was supported in part by the US Department of Energy under grants DE-FG02-97ER41033 and DE-FG02-97ER41041.

[3]And even considering a brief teenage flirtation with the notion that my mother was attempting to poison me, I have never suspected a false pretense.

TABLE OF CONTENTS

LIST OF TABLES

LIST OF FIGURES

LIST OF ABBREVIATIONS

#× Cs	(PH expressed as a multiple of 477 keV, the maximum energy of an electron recoiling after Compton scattering with a 662 keV gamma from ^{137}Cs. Typically used to express a threshold.)
$0\nu\beta\beta$	neutrinoless double beta decay (see chapter 1)
$2\nu\beta\beta$	double beta decay (see chapter 1)
ADC	analog to digital converter (measures the height of a continuous signal, output is a discrete value)
BCI	beam current integrator (a fancy ammeter)
BCS	Bardeen, Cooper, and Schrieffer (refers to 3 scientists and their microscopic theory of fermion pairing)
BNC	Bayonet Neill-Concelman (a common type of coaxial cable connector)
BOT	beam on target (the electrical current generated when a beam of charged particles hits a conducting beamstop)
CAD	computer assisted design (used to make virtual models of stuff)
CFD	constant fraction discriminator (generates a logic pulse at the time when a signal reaches a fixed fraction of its maximum)
CM	center of mass (frame of reference commonly used for nuclear reaction calculations)
CODA	CEBAF Online Data Acquisition (software used to acquire data at TUNL)
DAQ	data acquisition system (generally refers to VME electronics and the PC that interfaces with them)
DWBA	distorted wave Born approximation (see chapter 2)
ECL	emitter-coupled logic (a standard for voltage levels of logic pulses)

F Fermi (used as a subscript, refers to a transition where the emitted particles couple to a singlet state)

FRESCO (a coupled-channel reaction code by Ian Thompson)

FWHM full width at half maximum (a typical statistic for quoting the width of a peak)

GT Gamow-Teller (used as a subscript, refers to a transition where the emitted particles couple to a triplet state)

HIS helium-ion source

i,f initial, final (used as a subscript)

KSUEFF Kent State University efficiency (a Monte-Carlo efficiency code)

LEMO (a common type of coaxial cable connector, named after Leon Mouttet)

MCA multi-channel analyzer (same as an ADC)

NEEF7 neutron efficiency (a Monte-Carlo efficiency code)

NIM nuclear instrumentation module (an electrical and mechanical standard for electronic modules, also a standard for voltage levels of logic pulses)

NIS negative ion source (generally refers to an inflection magnet on the low-energy beam line)

NSM nuclear shell model (see chapter 1)

OR (a logic gate; output is TRUE if any input is TRUE)

P/S Phillips Scientific® (an electronics company)

PAW Physics Analysis Workstation (somewhat obsolete Fortran-based software for analyzing data; still used by aging scientists)

PH pulse height (corresponds to the energy deposited in a detector)

PMT	photomultiplier tube (a vacuum tube device that generates a relatively large pulse of charge when hit with a few photons)
PSD	pulse shape discrimination (technique to distinguish between gammas and neutrons by a detectors signal shape)
QRPA	quasiparticle random phase approximation (see chapter 2)
RGA	residual gas analyzer (measures the molecular composition of a gas)
ROI	region of interest
ROOT	(C++ based software for analyzing data)
sccm	standard cubic centimeters per minute
TDC	time to digital converter (a fancy stopwatch)
stat, sys	(used as a subscript, refers to statistical or systematic errors)
TOF	time-of-flight (typically measured to determine neutron energy)
TTL	transistor-transistor logic (a standard for voltage levels of logic pulses)
TUNL	Triangle Universities Nuclear Laboratory ('tis a silly place)
VCR	vacuum coupling radiation (a type of flat-face seal vacuum fittings)
VDC	volts, direct current
VME	Versa Module Europa (a computer bus standard)

LIST OF SYMBOLS

ϵ	detector efficiency or a small number used to do complex integration
$\|\Phi\rangle$	bound state
$\|\psi\rangle$	total system state or nuclear state
$\|0\rangle$	vacuum state
$\|BCS\rangle$	BCS state
$\|J^{\pi}\rangle$	state with total angular momentum J and parity π
λ	decay rate
μ	mean of a Gaussian function
Ω	solid angle
σ	width of a Gaussian fucntion or standard deviation or cross section
θ	angle relative to beam axis or scattering angle
A	amplitude of a Gaussian function
$a/a^{\dagger}$	single particle annihilation/creation operator
BCI	number of pulses from the beam current integrator
$c/c^{\dagger}$	quasiparticle annihilation/creation operator
charge state	charge of a particle in units of electron charges
e	electron charge
E	energy

F	area of crystal face
f	general function or form factor/scattering amplitude
f_0	natural frequency of a crystal oscillator
G	propagator or phase space factor or (constant) pairing interaction matrix elements
h	vertical distance between targets and boat in evaporator (i.e., height of targets above boat)
H	Hamiltonian or Hamiltonian operator
H_o	bare Hamiltonian
I	electric current
k	constant or magnitude of momentum
$\vec{k}$	momentum vector
K	kinetic energy
l	distance or flight path
LT	fraction of total run time that the DAQ was live
m	mass
$M^{2\nu/0\nu}$	matrix elements for two-neutrino/zero-neutrino double beta decay
N	neutron number or number of particles or frequency constant
n	target thickness with units of mass/area or an integer
P	power or pressure

P_q	density of quartz
PO	fraction of expected beam pickoffs recorded by the capacitive pickoff unit
Q	Q-value
r	radius or magnitude of position
$\vec{r}$	position vector
t	time coordinate
T	transition matrix
$T_{1/2}$	half-life
U	amplitude for single-particle annihilation
V	interaction term or amplitude for single-particle creation or voltage
w	transition rate
W	transition probability
x	general dependent coordinate or position coordinate
Y_n	neutron yields
Z	proton number

CHAPTER 1: Introduction

This work was primarily motivated by ongoing studies of the neutrino, a quite extraordinary fundamental particle. Neutrinos passing through a normal solid have a mean free path on the order 10 light-years (Krane [1987]). There are 3 types of neutrinos and any given neutrino changes between these types at random as time elapses (Zuber [2012]). Neutrinos might be used as a probe of large dense objects (which more common forms of radiation cannot penetrate) such as planets (Learned et al. [2008]) or stars (Davis [2003]). Neutrinos could also be used as a highly effective means of communication (Stancil et al. [2012]). More importantly, the properties of neutrinos and how they interact with matter can potentially provide new insights about the source of the matter and antimatter asymmetry in the universe (McKeown et al. [2014]) and processes for synthesizing the heaviest nuclei in supernova explosions (Woosley and Heger [2007]). The emphasis of this work is on nuclear structure issues relevant to the search for the undiscovered rare weak decay mode of nuclei in which two beta particles are emitted from the decaying nucleus without the associated neutrinos as constrained by lepton-number conservation in the Standard Model of particle physics. The observation of this decay mode would be direct evidence for violation of lepton number conservation.

Section 1.1: Overview of Neutrinos

The existence of neutrinos, light and electrically neutral Fermions, was first proposed in 1930 by Wolfgang Pauli to conserve energy and momentum in nuclear beta decay (Reines and Cowan [1997]). This particle, later named electron neutrino, was experimentally detected in 1956 by Fred Reines and Clyde Cowan (Reines and Cowan [1956]). Two other types or

"flavors" of neutrinos have been discovered: the muon neutrino in 1962 by Leon Lederman, Melvin Schwartz, and Jack Steinberger (Danby et al. [1962]) and the tau neutrino in 2000 by the DONUT collaboration (Kodama et al. [2001]).

Because the neutrino is an electrically neutral lepton and has no discernable magnetic moment, it is unaffected by the electromagnetic force. Also, the neutrino does not couple directly to gluons or quarks, therefore, they do not interact with matter via the strong nuclear force. The gravitational force is extremely weak, so only via weak interactions can neutrinos be detected. These interactions act over a very short range, so typical cross sections for weak interactions are on the order of femtobarns (Zuber [2012]).

Some fundamental properties of neutrinos have yet to be determined, including their masses and their symmetry features, e.g., whether they are Dirac fermions (left-handed chirality) or Majorana fermions (mixture of left-handed and right-handed chirality). In the Standard Model of particle physics, neutrino masses were set to zero, allowing left-handed neutrinos and right-handed anti-neutrinos. However, experiments conducted during the last decade have unambiguously observed that neutrino flavors oscillate, confirming that neutrinos have mass.

Electron neutrinos are a common product of nuclear reactions involving the weak interaction, and as such there is an enormous neutrino flux from the Sun, $\sim 10^{10}\ {}^{\nu_e}/_{cm^2 \cdot s}$ on Earth (Zuber [2012]). Observations of solar neutrinos began in 1968 (Davis et al. [1968]). The early studies consistently measured a lower flux than predicted by standard solar models. This discrepancy was called the "solar neutrino problem". In 1998, measurements of atmospheric neutrinos (neutrinos produced by interactions of cosmic rays in earth's upper atmosphere) at the Super-Kamiokande neutrino observatory (Fukuda et al. [1998]) and measurements of solar neutrinos at the Sudbury Neutrino Observatory (SNO) in 2002 (Ahmad et al. [2002]) provided clear evidence for spontaneous neutrino flavor change. This phenomenon is called neutrino oscillation and solves the solar neutrino problem; of all the electron neutrinos produced in the Sun, only $\sim {}^1/_3$ are electron neutrinos after traversing the earth-sun distance.

The remainder have oscillated into either muon or tau neutrinos.

Neutrino oscillation implies a non-zero neutrino mass (Zuber [2012]). In 2014, an estimate of the summed neutrino mass, given below, was calculated using observations of the cosmic microwave background (Battye and Moss [2014]),

$$\sum m_\nu = 0.320 \pm 0.081 \ eV.$$

A large number of direct neutrino mass searches have been conducted and are discussed in chapter 6 of Zuber [2012]. However, the masses of the individual neutrino flavor states remain unknown.

Another unknown property of neutrinos is their particle/antiparticle nature. All other fundamental fermions in the Standard Model are clearly distinguished between particles and antiparticles by their electric charge. Since neutrinos have no charge, it is unclear whether the particle and antiparticle are distinguishable (i.e. Dirac particles) or identical (i.e. Majorana particles) (Majorana [1937]). However, the small upper limit on neutrino mass suggests that neutrinos are Majorana particles (Mohapatra and Senjanović [1980]).

The existence of a Majorana lepton would violate lepton number conservation, a fundamental tenet of the Standard Model. Such an observation will provide potential mechanisms for explaining the origin of the matter and antimatter asymmetry in the universe. A type of nuclear decay called neutrinoless double beta decay ($0\nu\beta\beta$) may proceed via several mechanisms, including the exchange of a light Majorana neutrino or much heavier particles ($\gtrsim 1$ TeV). The simplicity of Majorana neutrino exchange makes it the favored process (Avignone et al. [2008]). Regardless of mechanism, $0\nu\beta\beta$ may only proceed if neutrinos are Majorana particles (Racah [1937] and Schechter and Valle [1982]). Therefore, the $0\nu\beta\beta$ process is considered the gold-standard for probing the nature of neutrinos.

Section 1.2: Neutrinoless Double Beta Decay

Double beta decay is a rare form a nuclear decay that can occur in certain isotopes in which single beta decay is energetically forbidden but double beta decay is allowed (Fig. 1.1). Two-neutrino double beta decay ($2\nu\beta\beta$) is a normal Standard Model process in which two neutrons simultaneously transform into two protons, emitting two beta particles and two antineutrinos.

$$(Z, A) \rightarrow (Z + 2, A) + 2e^- + 2\overline{\nu}_e$$

This decay was first proposed in 1935 by Maria Goeppert-Mayer (Goeppert-Mayer [1935]) and first observed in 1987 by Steve Elliot (Elliott et al. [1987]). Another double beta decay mode, $0\nu\beta\beta$, was first proposed in 1937 by Giulio Racah (Racah [1937]), in which two neutrons transform into two protons via the exchange of a Majorana neutrino and only two beta particles are emitted.

$$(Z, A) \rightarrow (Z + 2, A) + 2e^-$$

This mode of double beta has yet to be observed. A list of some isotopes that decay via $2\nu\beta\beta$ along with their decay half-lives are given in Table 1.1.

Table 1.1: Examples of isotopes that double beta decay along with their half-lives. The results are listed by year of publication. Also included are the phase factors ($G^{2\nu}$) and the nuclear matrix elements ($M^{2\nu}$) from equation 1.3. This table was taken from Albert et al. [2014].

Nuclide	$\mathbf{T}^{test}_{1/2}$ **± stat ± sys** [y]	**rel. uncert.** [%]	$\mathbf{G}^{2\nu}$ [10^{-21} y^{-1}]	$\mathbf{M}^{2\nu}$ [MeV^{-1}]	**rel. uncert.** [%]	**Experiment (year)**
^{136}Xe	$2.165 \pm 0.016 \pm 0.059 \cdot 10^{21}$	±2.83	1433	0.0218	±1.4	EXO-200 (2014) Albert et al. [2014]
^{76}Ge	$1.84^{+0.09+0.11}_{-0.08-0.06} \cdot 10^{21}$	$^{+7.7}_{-5.4}$	48.17	0.129	$^{+3.9}_{-2.8}$	GERDA (2013) Agostini et al. [2013]
^{130}Te	$7.0 \pm 0.9 \pm 1.1 \cdot 10^{20}$	±20.3	1529	0.0371	±10.2	NEMO-3 (2011) Arnold et al. [2011]
^{150}Nd	$9.11^{+0.25}_{-0.22} \pm 0.63 \cdot 10^{18}$	$^{+7.4}_{-7.3}$	36430	0.0666	$^{+3.7}_{-3.7}$	NEMO-3 (2009) Argyriades et al. [2009]
^{100}Mo	$7.11 \pm 0.02 \pm 0.54 \cdot 10^{18}$	±7.6	3308	0.250	±3.8	NEMO-3 (2005) Arnold et al. [2005]

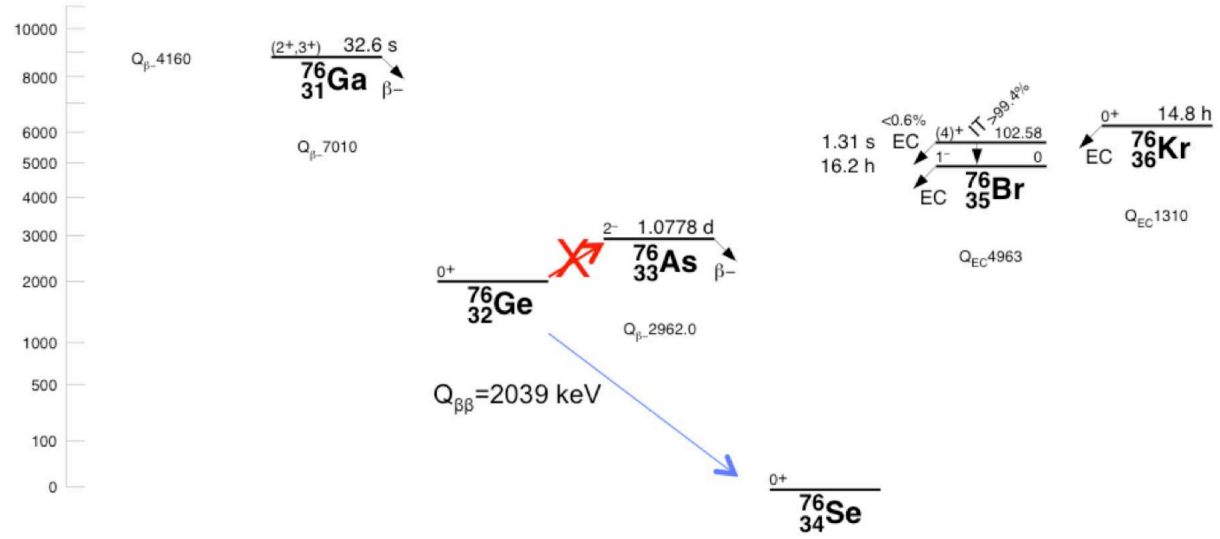

Figure 1.1: Decay scheme for isotopes of with A = 76. Energy scale is keV. The ^{76}Ge is energetically forbidden from single beta decay to ^{76}As, but can double beta decay to ^{76}Se with a Q-value of 2039 keV. This figure was adapted from Ekstrom and Firestone [2004].

1.2.1: Relationship Between $0\nu\beta\beta$ and Neutrino Mass

Fermi's Golden Rule (Fermi [1950]) describes the transition rate between an initial state $|i\rangle$ and a final state $|f\rangle$. In the notation of Zuber [2012],

$$\frac{dW}{dt} = \frac{2\pi}{\hbar} |\langle f \,|\, H_{if} \,|\, i\rangle|^2 \delta(E_f - E_i) \tag{1.1}$$

where W is the transition probability, H_{if} is the weak Hamilton operator, and $E_{i/f}$ is the initial/final state energy. For double beta decay, the transition nuclear matrix element must include virtual states $|m\rangle$ in the intermediate nucleus (e.g., ^{76}As in the decay of ^{76}Ge) so,

$$\langle f \,|\, H_{if} \,|\, i\rangle \rightarrow \sum_m \frac{\langle f \,|\, H_{if} \,|\, m\rangle \langle m \,|\, H_{if} \,|\, i\rangle}{E_i - E_m - E_\nu - E_e}. \tag{1.2}$$

For $2\nu\beta\beta$, the transition probability, expressed as the decay rate λ or the half-life $T_{1/2}$ is

$$\lambda_{2\nu}/\ln 2 = \left(T^{2\nu}_{1/2}\right)^{-1} = G^{2\nu}(Q,Z)|M^{2\nu}_{GT} + M^{2\nu}_{F}|^2 \tag{1.3}$$

where $G(Q, Z)$ is an easily-calculable phase factor and $M_{GT/F}$ are the Gamow-Teller/Fermi contributions to the total nuclear matrix element. For $0\nu\beta\beta$ mediated by a light Majorana neutrino, the finite neutrino mass, $\langle m_{\nu_e} \rangle$ must be accounted for and the phase space is much larger (by $\sim 10^6$) because the virtual neutrino in the intermediate state is confined to the volume of the nucleus. The half-life is

$$\lambda_{0\nu}/\ln 2 = \left(T^{0\nu}_{1/2}\right)^{-1} = G^{0\nu}(Q, Z)|M^{0\nu}_{GT} - M^{0\nu}_{F}|^2 \left(\frac{\langle m_{\nu_e} \rangle}{m_e}\right)^2 \tag{1.4}$$

Therefore, a confirmation of $0\nu\beta\beta$ via light Majorana neutrino exchange and measurement of the decay half-life, would permit direct calculation of the electron neutrino mass if the $0\nu\beta\beta$ nuclear matrix elements can be calculated accurately. However, there is considerable dispersion in the values of the nuclear matrix elements calculated for each isotope using various methods. This dispersion may be representative of the theoretical uncertainties in the calculations arising from incomplete nuclear structure modeling. Although, as shown in Fig. 1.2, there are several methods used to calculate $M^{0\nu}$. The two most common are the nuclear shell model (NSM) and the quasiparticle random phase approximation (QRPA). These two methods are A briefly discussed next.

The NSM method is straightforward, using a Hamiltonian matrix built from a core and a valence space of single-particle orbitals (see Fig. 1.3). The main issue with this approach is that the dimensions of the Hamiltonian matrix increase geometrically with the included orbitals. Consequently, important orbitals are typically truncated from the valence space to make calculation feasible. The QRPA method uses quasiparticles, which are a superposition of single-particles and single-holes. Pairing interactions between like nucleons are explicitly accounted for with the BCS model. The QRPA is discussed further in chapter 2 and details on both methods may be found in (Vogel [2008] and Avignone et al. [2008]). The QRPA approach is considered more accurate than the NSM because of the uncertainty created by truncating the valence space in NSM calculations (Avignone et al. [2008]). On the other hand, a concern with QRPA calculations is the limited number of valence nucleon configurations

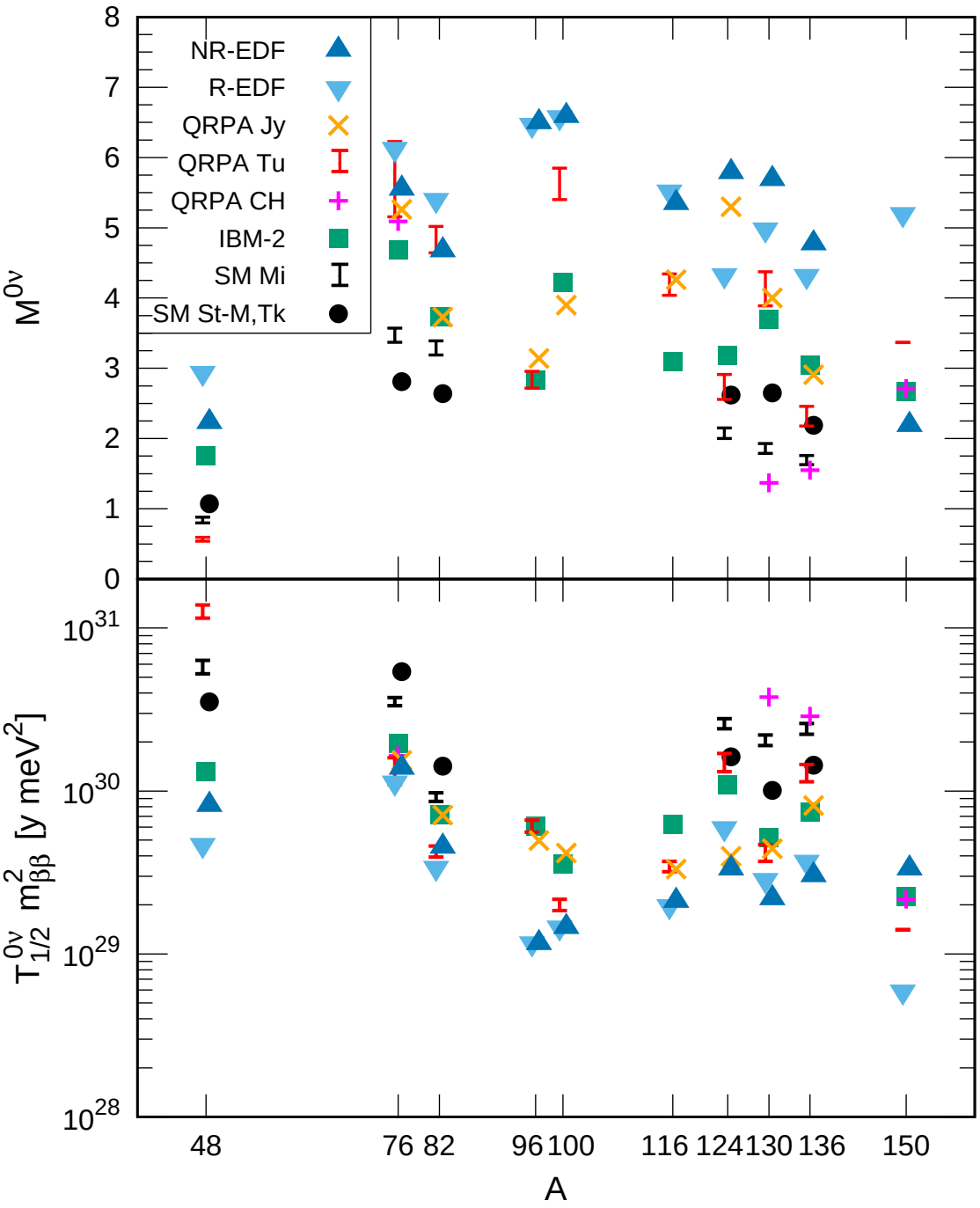

Figure 1.2: Plots of the nuclear matrix elements for $0\nu\beta\beta$ and the corresponding predicted half-lives for various nuclei, computed using a variety of theoretical methods: non-relativistic and relativistic energy density functional theory (EDF), QRPA from several groups, the interacting boson model (IBM-2), and the nuclear shell model (SM) from several groups. These plots were taken from Engel and Menéndez [2016].

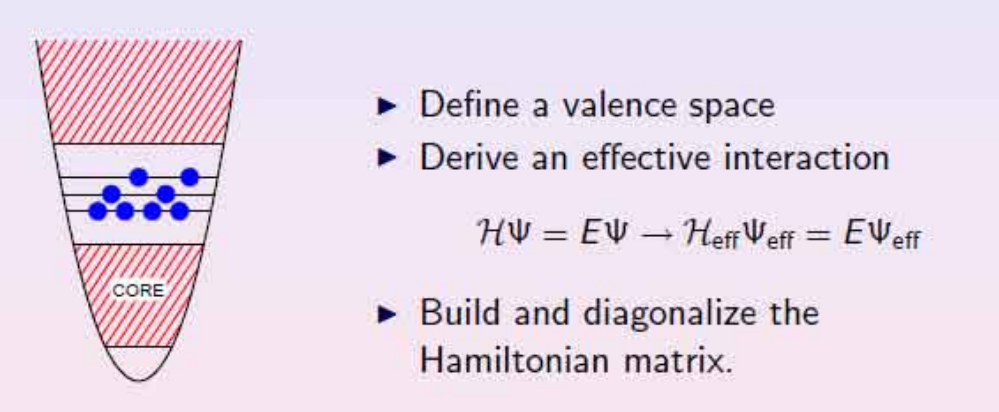

Figure 1.3: A schematic of the basic procedures in the NSM. This figure was taken from Vogel [2009]

used to model the nuclear wavefunctions.

A large amount of nuclear structure information is required to make precise calculations of $M^{0\nu}$, including single-nucleon valence populations and details regarding the effects of nucleon-nucleon pairing interactions in both the parent and residual nuclei. Valence orbital occupancies are measured using single-nucleon transfer reactions. The effects of pairing interactions are investigated using light-ion induced two-nucleon transfer reactions, e.g., (t,p), (p,t), $(^3He,n)$ and $(n,^3He)$. As further discussed in chapter 2, the need for $(^3He,n)$ reaction data is the motivation for this dissertation.

Section 1.3: Prior Measurements of the $(^3He,n)$ Reaction

Most of the existing data relevant to examining the importance of nucleon-nucleon pairing interactions in nuclei used in searches for $0\nu\beta\beta$ are from two-neutron pickup (p,t) and two-neutron dropoff (t,p) reactions. The amount of data on proton-pairing interactions from the analogous $(^3He,n)$ and $(n,^3He)$ reactions is considerably less because of the technical challenges in obtaining the required energy resolution for detecting neutrons and the lack of facilities with the capabilities required to measure these reactions (Freeman and Schiffer [2012]).

Differential cross sections for the $(^3He,n)$ reaction were measured on ^{130}Te by Alford

et al. [1979b], ^{100}Mo by Fielding et al. [1976], and ^{136}Xe by Alford et al. [1979a]. As of 2012, no studies of the (^3He,n) reaction had been conducted on ^{150}Nd or ^{76}Ge (Freeman and Schiffer [2012]).

The choice of ^{76}Ge as the first nucleus to be studied is because of the work of research groups at the Triangle Universities Nuclear Laboratory (TUNL) in the MAJORANA Collaboration, an experimental collaboration that is searching for $0\nu\beta\beta$ in this isotope (Abgrall et al. [2014]). In 2013, scientists at the Notre Dame University tandem accelerator measured differential cross sections for the ^{74,76}Ge(^3He,n) reactions at a beam energy of 16 MeV (Roberts et al. [2013]). Their measurements covered the angle range between 6° and 22°, relative to the beam axis, using 16 vertically-mounted plastic scintillator bars with dimensions 1.5 m $\times$ 0.15 m $\times$ 0.05 m. The results of that work are discussed in chapter 8.

This work also consisted of measurements of the ^{74,76}Ge(^3He,n) reactions, but improved upon the measurements made by Roberts et al. [2013]. Using liquid scintillator detectors, PSD techniques were used to exclude nearly all gammas from the measured time-of-flight (TOF) spectra. This enabled a foreground-to-background ratio sufficiently high to measure the cross section for transfer to the first excited 0^+ state, in addition to the 0^+ ground state, in both nuclei. Measurements were made between 0° and 18° in order to use the shape of the differential cross section for clear identification of the two-proton transfers that involved zero angular momentum transfer (i.e., transfer to 0^+ states). Such transfers have a strong enhancement at small angles. Measurements were made at two beam energies as a consistency check. A beam energy of $E_{3He} = 15$ MeV was chosen to maximize TOF energy resolution while exceeding the Coulomb barrier. A second beam energy of $E_{3He} = 21$ MeV was used to confirm the results obtained at 15 MeV and to have measurements at an energy close to the $E_{3He} = 25.4$ MeV of Alford et al. [1979b] (25.4 MeV was not used due to limitations of the tandem accelerator at TUNL).

1.3.1: The Search for $0\nu\beta\beta$ in ^{76}Ge

So far, the only observed form of double beta decay is $2\nu\beta\beta$. In this decay process, a portion of the decay energy is carried off by the neutrinos. While beta particles are easily detected with 100% efficiency, neutrino detection efficiency is effectively 0% due to their extremely small interaction cross section. However, for $0\nu\beta\beta$, only two beta particles are emitted. In this case, the full decay Q-value would be split equally between the beta particles' kinetic energies, neglecting the nuclear recoil. Therefore, as shown in Fig. 1.4, $2\nu\beta\beta$ produces a broad pulse-height (PH) spectrum between $0 < K_e < Q$ and $0\nu\beta\beta$ would produce a narrow PH spectrum at $K_e = Q$ (where K_e is the total kinetic energy of the two emitted beta particles). Because $\lambda_{0\nu} \ll \lambda_{2\nu} \approx 10^{-20}$ yr^{-1}, the primary experimental challenges in attempting to observe $0\nu\beta\beta$ are resolving the $K_e = Q$ peak from the high-energy tail of the $2\nu\beta\beta$ continuum and reducing backgrounds (from cosmic rays and natural radioactivity) in the ROI to acceptable levels.

Efforts are underway worldwide to observe $0\nu\beta\beta$ in various isotopes and confirm the Majorana nature of neutrinos (Henning [2016]). $0\nu\beta\beta$ in ^{76}Ge motivates our measurements of the Ge(^3He,n)Se reaction. The MAJORANA DEMONSTRATOR is a ^{76}Ge $0\nu\beta\beta$ experiment currently running at the Sanford Underground Research Facility (SURF), located in the old Homestake gold mine in Lead, SD. This experiment will use up to 30 kg of 86% enriched ^{76}Ge in modular arrays of P-type point contact (PPC) high-purity germanium (HPGe) detectors refined from either natural or enriched Ge and placed in custom ultra-low background cryostats. These detectors are ideal for studying $0\nu\beta\beta$ mainly because of their high energy-resolution characteristics and low radioactive contaminants. The DEMONSTRATOR makes use of passive and active shielding along with a radon purge in order to reduce backgrounds. To reduce the cosmic ray background, the experiment is located at the 4850 ft level of the mine. The goal of the MAJORANA collaboration is to demonstrate that a future 1-tonne experiment can achieve a background sensitivity of 3 counts per tonne-year in a 4-keV wide window around the ^{76}Ge $Q_{\beta\beta}$-value of 2039 keV (Abgrall et al. [2014]).

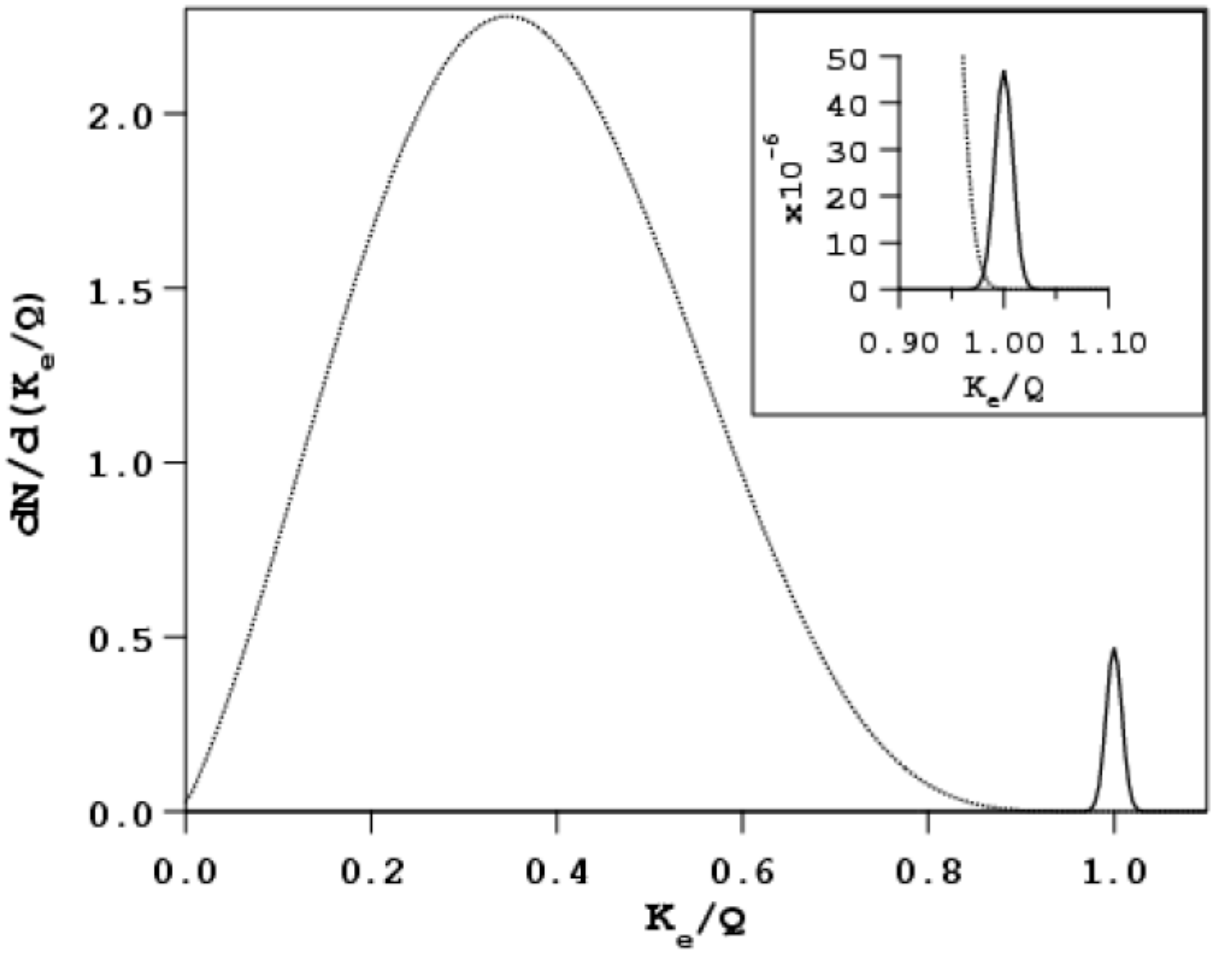

Figure 1.4: A calculated PH spectrum for beta particles emitted in the double beta decay of a nucleus. The continuum between $0 < K_e/Q < 1$ is due to the $2\nu\beta\beta$ mode and the narrow peak at the full Q-value is due to the $0\nu\beta\beta$ mode. The amplitude of the $2\nu\beta\beta$ continuum is arbitrary. This example includes 2% energy resolution smearing. The figure is for $\lambda_{0\nu}/\lambda_{2\nu} = 1/100$ and the insert is for (the predicted value of) $\lambda_{0\nu}/\lambda_{2\nu} = 1/10^6$. This figure was taken from Vogel [2008].

Section 1.4: Summary of Research Infrastructure Improvements at TUNL

Substantial enhancements to the research capabilities at TUNL were required to carry out the measurements in this dissertation. These were the first (^{3}He,n) reaction measurements to be performed in the tandem laboratory at TUNL since studies of the C(^3He,n) reaction in 1973 (Rhea [1973]). The infrastructure has been optimized for (α,n) and (^3He,n) reaction measurements that require pulsed beams for neutron-energy spectroscopy via the TOF technique. The new capabilities implemented in this project include: (1) construction of a dedicated beam line for charge-exchange reaction measurements with neutrons emitted in the exit channel, e.g., (α,n) and (^3He,n) reactions, (2) installation of a ^{3}He gas recovery system on the helium-ion source, and (3) development of beam-pulsing capabilities for ion beams from the helium-ion source (HIS). Descriptions of these technical developments are given in chapters 3 and 6.

CHAPTER 2: Theoretical Considerations

The primary goal of measuring the ^{74,76}Ge(^3He,n)^{76,78}Se cross section was to assess the validity of using the BCS approximation for wavefunctions of the initial and final ground states in QRPA calculations of $M^{0\nu}$. In addition, the cross section data for ground state to ground state transfer enables an investigation of the reaction mechanism for two-proton dropoff at low projectile energy (i.e., ∼10 MeV), namely the relative contributions from simultaneous and sequential particle transfer. The features of the BCS model relevant to evaluating its validity in QRPA calculations of $M^{0\nu}$ are discussed below. Also, the formalism for using the distorted-wave Born approximation (DWBA) to calculate the cross section for two-nucleon transfer reactions is discussed below.

Section 2.1: Nuclear Matrix Element Calculations

The QRPA simplifies the inclusion of pairing correlations for calculation of nuclear matrix elements by the using quasiparticles instead of single particles(Vogel [2008]). A quasiparticle is a linear combination of a single-particle and a single-hole. The quasiparticle creation and annihilation operators are given by

$$c_k^\dagger = U_k a_k^\dagger - V_k a_k \tag{2.1}$$

$$c_k = V_k a_k^\dagger + U_k a_k \tag{2.2}$$

where $a^\dagger/a$ are the single-particle creation/annihilation operators in the second quantization. The coefficients U_k and V_k are amplitudes related to the occupancy of single-particle state k.

Within the QRPA framework, the $0\nu\beta\beta$ matrix element is given by (Suhonen and Civitarese [2010]and Vogel [2008])

$$M_K^{0\nu} = \sum_{J^\pi, k_i, k_f, J'} \sum_{pnp'n'} (-1)^{j_n + j_{p'} + J + J'} \times$$
$$\sqrt{2J'+1} \begin{Bmatrix} j_p & j_n & J \\ j_{n'} & j_{p'} & J' \end{Bmatrix} \langle pp' : J' \parallel O_K \parallel nn' : J' \rangle \times$$
$$\left\langle 0_f^+ \left\| [c_{p'}^\dagger c_{n'}]_J \right\| J^\pi k_f \right\rangle \langle J^\pi k_f \mid J^\pi k_i \rangle \left\langle J^\pi k_i \left\| [c_p^\dagger c_n]_J \right\| 0_i^+ \right\rangle \tag{2.3}$$

where K = Fermi or Gamow-Teller. The final term in equation 2.3 is of interest for this work because it contains the wavefunctions for the 0^+ ground states of the initial and final nuclei, $\left|0_i^+\right\rangle$ and $\left|0_f^+\right\rangle$. These states are approximated using the BCS model.

Section 2.2: The BCS Model and Two-Nucleon Transfer Strengths

The wavefunctions of the initial and final nuclei used in QRPA calculations of $M^{0\nu}$ are described by the BCS model (Bloxham et al. [2010]). The BCS state is given by (Brink and Broglia [2005])

$$|BCS\rangle = \prod_{k>0}^{\infty} (U_k + V_k a_k^\dagger a_{-k}^\dagger) |0\rangle \tag{2.4}$$

where k represents the particle's state and $-k$ represents the time-reversed state. The coefficients U_k and V_k represent the amplitudes for the occupation of state k with a particle pair. Specifically, state k is occupied with probability V_k^2 and empty with probablility U_k^2. These amplitudes are determined by single-particle transfer reactions. Because the BCS state only contains particle pairs, it is necessarily $J^\pi = 0^+$.

The Hamiltonian in the BCS model is split into single-particle and pairing terms

$$H = H_{sp} + H_p \tag{2.5}$$

$$H_p = -G \sum_{k>0}^{\infty} a_k^\dagger a_{-k}^\dagger a_k a_{-k} \tag{2.6}$$

which has constant matrix elements G that describe the strength of the pairing interaction.

A simple two-level system demonstrates the key predictions of the BCS model (Brink and Broglia [2005]). Though the two-level or Högaasen-Feldman system (Högaasen-Feldman [1961]) is a grossly simplified application of the BCS model it has all the main features of the model and allows for first-order estimates of nuclear excitation spectra and probabilities for nucleon pair transfer. In this two-level system, there are n pairs of particles distributed between two single-particle levels and each level has a pair degeneracy of Ω. The separation between the two levels is D. The strength of the pairing interaction relative to the level separation is given by the parameter

$$x = 2G\frac{\Omega}{D}. \tag{2.7}$$

In the limit $x \to 0$ (i.e., no pairing), the ground state of the model is represented by the lowest single-particle-energy configuration (i.e., pairs occupy the upper level only if the lower level is completely full) and the "i-th" excited state is represented by the promotion of i pairs from the ground state configuration to the upper level. As pairing strength increases, states are increasingly represented by mixtures of multiple pair-configurations. (To avoid confusion, please note that in this section "level" refers to a group of single-particle occupancies, akin to an orbital in the nuclear shell model. The term "state" refers to an energy eigenstate of the entire system.)

The energies of states and pair-transfer cross sections have been calculated (by Brink and Broglia [2005]) for a two-level model with $\Omega = 20$, an initial number of pairs $n = 20$, and $x = 0.5$ (Fig. 2.1) or $x = 2.0$ (Fig. 2.2). The initial nucleus with $n = \Omega$ is analogous to a

closed-shell nucleus (e.g., the proton shell in $^{A}_{32}$Ge).

As shown in Figs. 2.1 and 2.2, the two-level model predicts the pair transfer strength from the ground state of a closed-shell nucleus to an excited state of the residual nucleus should be no more than about 10% of the corresponding ground state to ground state pair transfer cross section. These results generalize to more complex BCS models with multiple levels and differing level degeneracy. In particular, the two-level model is a useful approximation when valence single-nucleon levels are separated by a gap, such as around a closed shell. The validity of the BCS model for even-even nuclei may be tested by two-nucleon transfer reactions. If more than about 10% of the two-nucleon transfer strength goes to a 0^+ excited state of the residual nucleus, equation 2.4 is no longer a valid approximation of the ground state of the residual nucleus (Freeman and Schiffer [2012] and Bloxham et al. [2010]).

The application of the BCS model to the 0^+ ground states in the $0\nu\beta\beta$ candidate ^{76}Ge and residual ^{78}Se is questionable because of the Te(^3He,n)Xe cross sections shown in Table 2.1. Tellurium has 52 protons, just past the $1g_{9/2}$ shell closure and should not have more than about 10% proton pair transfer strength to 0^+ excited states. The measurement of transfer strength to 0^+ excited states that greatly exceeds 10% indicates a break down of the BCS approximation for ^{130,132}Xe. This work, cross section measurements of ^{74,76}Ge(^3He,n)^{76,78}Se, was conducted to search for the possibility of a similar break down of the BCS approximation for these isotopes.

Table 2.1: Proton Pair Addition Strengths in Tellurium Isotopes by Alford et al. [1979b]

Target Nucleus	E_{ex} (MeV), $J^\pi = 0$	Normalized Cross Section
^{128}Te	0.0	1.00
	2.13	0.39 ± 0.08
^{130}Te	0.0	1.00
	1.85	0.38 ± 0.08
	2.49	0.24 ± 0.05

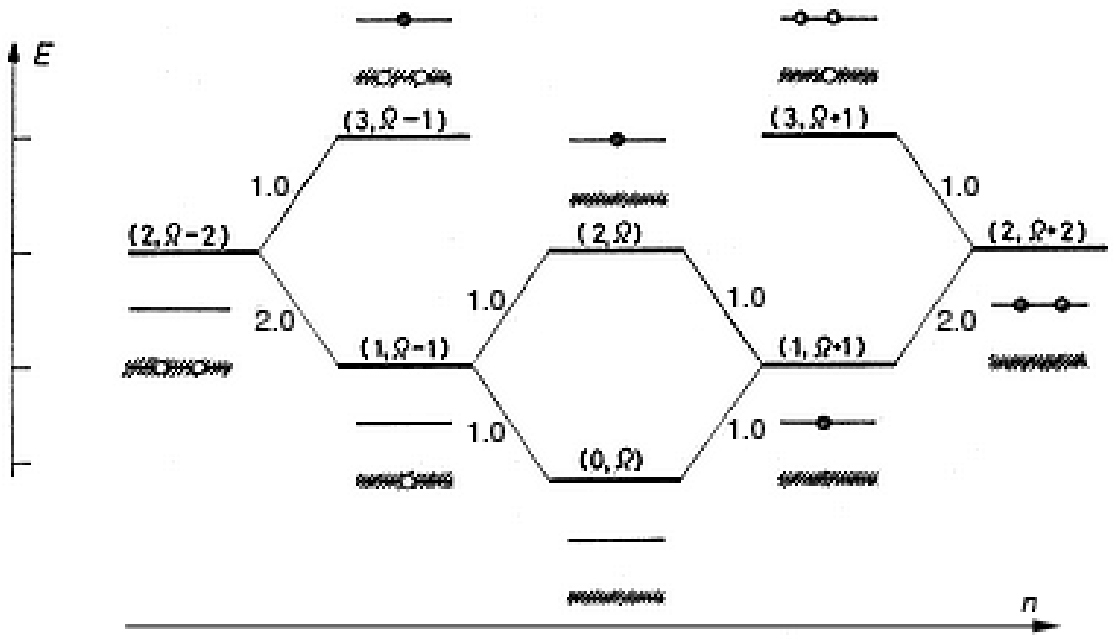

Figure 2.1: Schematic representation of the two-level model for $\Omega = 20$ and $x = 0.5$ (weak pairing). Each energy eigenstate is drawn as a horizontal line and labeled directly above with (E, n), where E is the normalized energy of the state and n is the number of pairs in that state. Sub-schematics of the pair-configuration corresponding to each state are drawn either above or below each state (note that each closed/open circle corresponds to a pair occupancy/hole. Diagonal lines are drawn connecting states with a significant pair transfer strength and labeled with the normalized cross sections. There is zero cross section for transfer from the ground state of the $n = 20$ nucleus to excited states in either the $n = 19$ or $n = 21$ nuclei. Because the uniform spacing of states resembles that of a simple quantum oscillator, this energy scheme is commonly referred to as a pairing vibrational band. This figure was adapted from Brink and Broglia [2005]

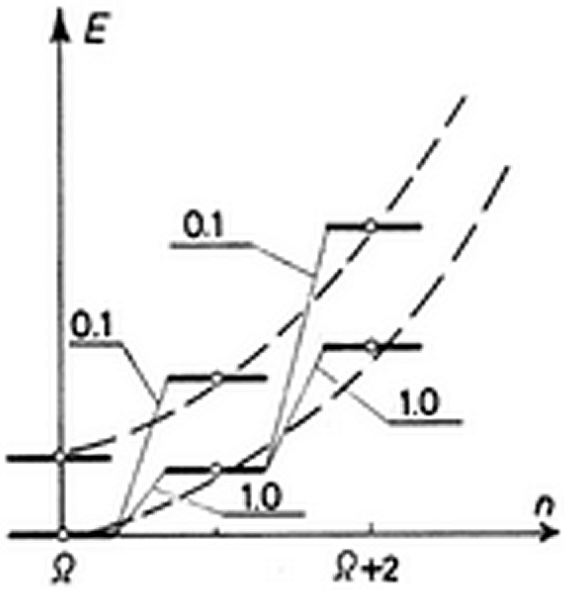

Figure 2.2: Schematic representation of the two-level model for $\Omega = 20$ and $x = 2.0$ (strong pairing). Each energy eigenstate is drawn as a bold horizontal line. Diagonal lines are drawn connecting states with a significant pair transfer strength and labeled with the normalized cross sections. Pair transfer may proceed from ground state to excited state, but with an order of magnitude less strength than the corresponding ground state to ground state transfer. Because the quadratic spacing of states with identical excitation resembles a simple quantum rotor, this energy scheme is commonly referred to as a pairing rotational band. This figure was taken from Brink and Broglia [2005]

Section 2.3: Two-Proton Transfer Reactions

The relative contributions of simultaneous and sequential nucleon transfer to two-proton dropoff reactions provides clues about the roles of long-range and short-range pair interactions between identical nucleons in the valence orbitals of nuclei. DWBA calculations are used to investigate the reaction mechanism for two-nucleon transfer, which may proceed via the simultaneous transfer of the nucleon pair (characterized by short-range pair interactions) or a sequential transfer of the individual nucleons (characterized by long-range pair interactions). Differential cross sections for both mechanisms were calculated for the ^{74,76}Ge(^3He,n) reaction.

2.3.1: Basic Scattering Theory

The differential cross section ($d\sigma$) is defined as the transition rate (between initial state $|i\rangle$ and final state $|f\rangle$) divided by the flux of particles (Sakurai and Napolitano [2011]). The transition rate is given by Fermi's golden rule

$$w(i \to f) = \frac{2\pi}{\hbar}|T_{fi}|^2 \delta(E_f - E_i) \tag{2.8}$$

where E_i, E_f are the initial and final state energies and T_{fi} are transition matrix elements given by

$$T_{fi} = \langle f \,|\, T \,|\, i \rangle = \left\langle f \,\middle|\, V \,\middle|\, \psi^{(+)} \right\rangle \tag{2.9}$$

where V describes the interaction between the particles and $\left|\psi^{(+/-)}\right\rangle$ are the total system states an infinite time before/after the interaction. These states are given by the Lippmann-Schwinger equation

$$\left|\psi^{(\pm)}\right\rangle = |i\rangle + \frac{1}{E - H_o \pm i\epsilon}\left|\psi^{(\pm)}\right\rangle \tag{2.10}$$

where H_o is the bare Hamiltonian with energy eigenvalues E and ϵ is a small number added to carry out complex integration.

2.3.2: The Plane-Wave Born Approximation and DWBA

Determination of the transition matrix elements, T_{fi}, is complicated by the lack of a closed analytical form for either the transition operator, T, or the total system states $\left|\psi^{(\pm)}\right\rangle$. The first-order plane-wave Born approximation makes the simplifications

$$\begin{aligned} T &= V \\ \psi^{(\pm)} &= e^{i(\vec{k}\cdot\vec{r})} \end{aligned} \tag{2.11}$$

for incident/ejected particle momentum and position coordinates $\vec{k}$ and $\vec{r}$. That is, the initial and final system wavefunctions are taken to be plane waves (Sakurai and Napolitano [2011]and Bassel et al. [1962]).

The DWBA uses distorted plane waves to describe the elastic scattering of the projectile by the target nucleus. In the notation of Thompson [2013],

$$\begin{aligned} \psi^{(+)}(\vec{k},\vec{r}) &= e^{i(\vec{k}\cdot\vec{r})} + f(\theta)\frac{e^{ikr}}{r} \\ \psi^{(-)}(\vec{k},\vec{r}) &= e^{i(\vec{k}\cdot\vec{r})} + f^{*}(\pi-\theta)\frac{e^{-ikr}}{r} \end{aligned} \tag{2.12}$$

describe the distorted waves without Coulomb interaction (Bassel et al. [1962]) where f is the scattering amplitude or form factor and θ is the scattering angle. The form factor is typically determined using an optical model potential to reproduce experimental results.

2.3.3: DWBA with two-Nucleon Transfer Reactions

The DWBA is modified from a two-body to a three-body problem to calculate cross sections for two-nucleon transfer reactions. The core of the target nucleus and each of the transferred nucleons are considered separate bodies. For light projectiles, the distance between the core (e.g., a neutron in the case of ^{3}He) and the two nucleons is approximated to be zero (Thompson [2013]).

The two-nucleon transfer reaction may be modeled as either a simultaneous (historically termed direct) or sequential (also called successive) transfer of the nucleons (Potel et al. [2013]). First and second-order DWBA transfer amplitudes mathematically represent these two processes, respectively. The total transfer cross section is directly proportional to the square of the sum of these two complex amplitudes. The first-order DWBA transfer amplitude (describing the simultaneous process) is (Thompson [2013])

$$T_{fi}^{(1)} = \left\langle \psi_f^{(-)} \Phi_f \left| H - E \right| \Phi_i \psi_i^{(+)} \right\rangle \tag{2.13}$$

where $|\Phi_i\rangle$ / $|\Phi_f\rangle$ are the bound state of the projectile/residual nucleus and H is the Hamiltonian for the entire system with energy eigenvalues E. The second-order DWBA transfer amplitude (describing the sequential process) is (Thompson [2013])

$$T_{fi}^{(2)} = \left\langle \psi_f^{(-)} \left| \langle \Phi_f \,|\, H - E \,|\, \Phi_j \rangle \, G_j \, \langle \Phi_j \,|\, H - E \,|\, \Phi_i \rangle \right| \psi_i^{(+)} \right\rangle \tag{2.14}$$

where G_j is the propagator for some intermediate channel j. Sequential transfer of the two nucleons is expected to dominate the cross section because the pairing interaction between the two nucleons is expected to be weak (Potel et al. [2013]).

The code FRESCO (Thompson [1988]) was used to perform DWBA calculations of the Ge(^3He,n)Se reaction in this dissertation. A sample calculation is shown in Fig. 2.3.

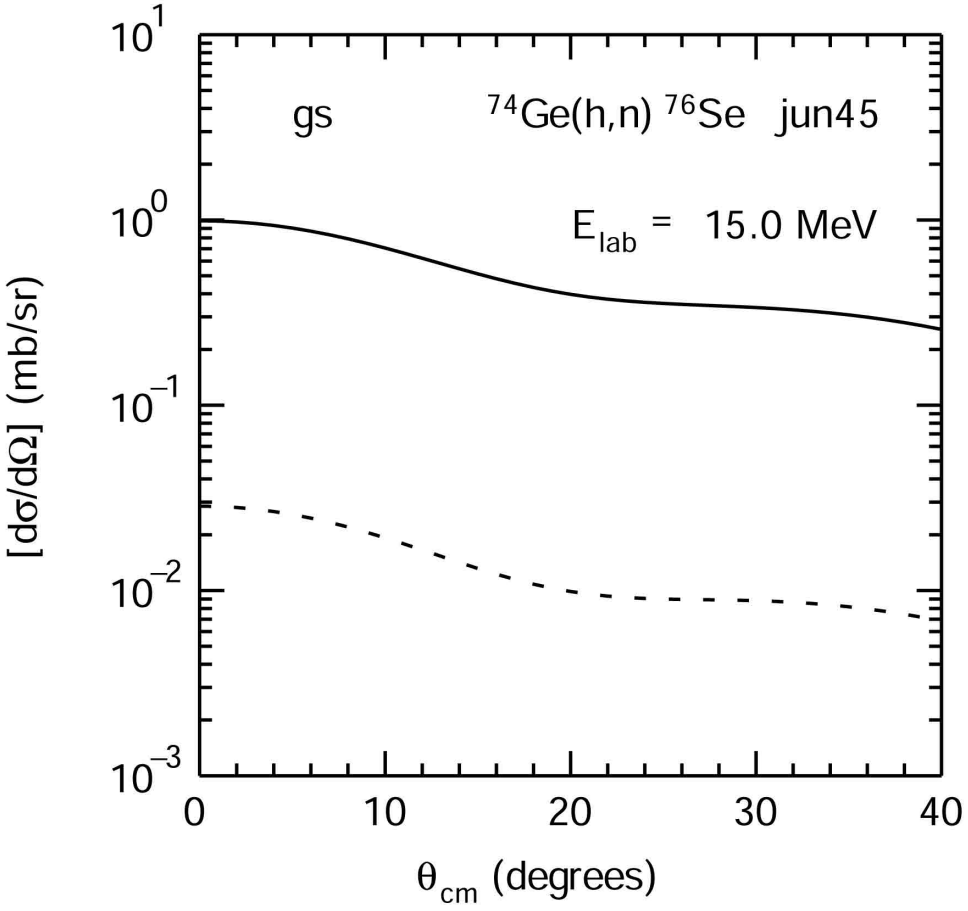

Figure 2.3: DWBA calculation of the differential cross section for ^{74}Ge(^{3}He,n)^{76}Se at 15 MeV for transfer to the ground state of ^{76}Se showing the contributions from the simultaneous and sequential processes. The solid curve is the total cross section (direct + sequential) and the dashed curve is for direct transfer only. Calculations were done by Dr. Alex Brown at Michigan State Univeristy.

CHAPTER 3: Experimental Details

The measurements reported in this dissertation were carried out in the tandem accelerator laboratory of the Triangle Universties Nuclear Laboratory (TUNL). This facility is located at Duke University in Durham, NC. The main accelerator in this facility is a FN tandem Van de Graaff that has a maximum terminal voltage of 10 MV. An overhead schematic of the tandem laboratory is given in Fig. 3.1. In this work, a 42 keV beam of $^3He^-$ ions was produced in the HIS. The DC $^3He^-$ beam was pulsed using the chopping and bunching systems before injection into the tandem. After acceleration, the pulsed $^3He^{++}$ beam at 15 MeV or 21 MeV was momentum analyzed by a high-precision dipole magnet (20-70 magnet) and directed down the 70-degree beamline to the germanium target. Targets were placed in a vacuum chamber at the end of the 70-degree beamline, located immediately before a shielding wall between the High-Energy Bay and Target Room 1. Neutrons leaving the target passed through the target chamber walls and an opening cleared in this shielding wall, and then traveled a distance of about 13 m to an array of neutron detectors. Detector signals were sent to data acquisition (DAQ) electronics in the Control Room. The HIS and accelerator were operated remotely from the Control Room.

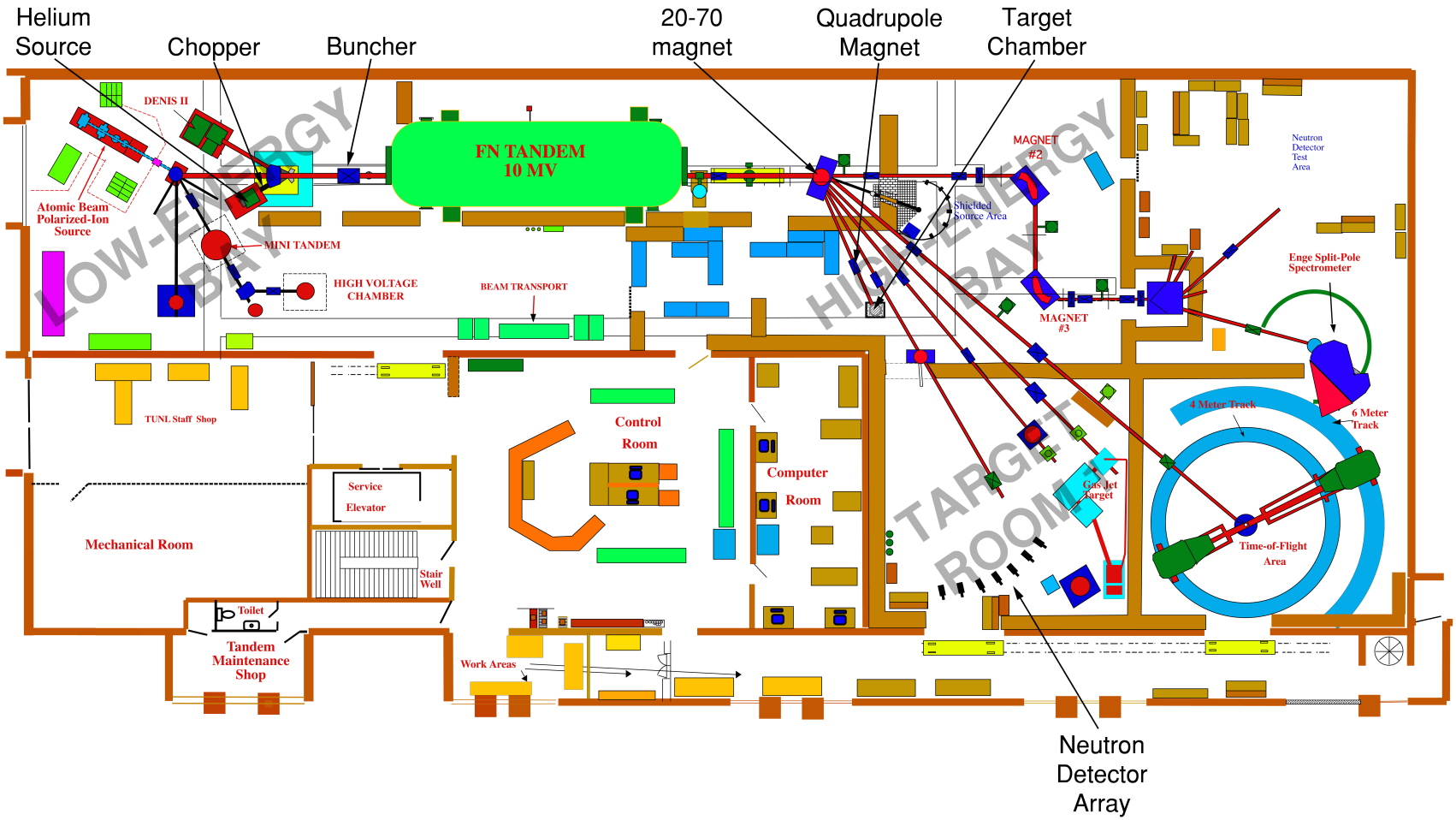

Figure 3.1: The floorplan of the FN tandem accelerator laboratory at TUNL. Key components of the experimental setup for this work are labeled.

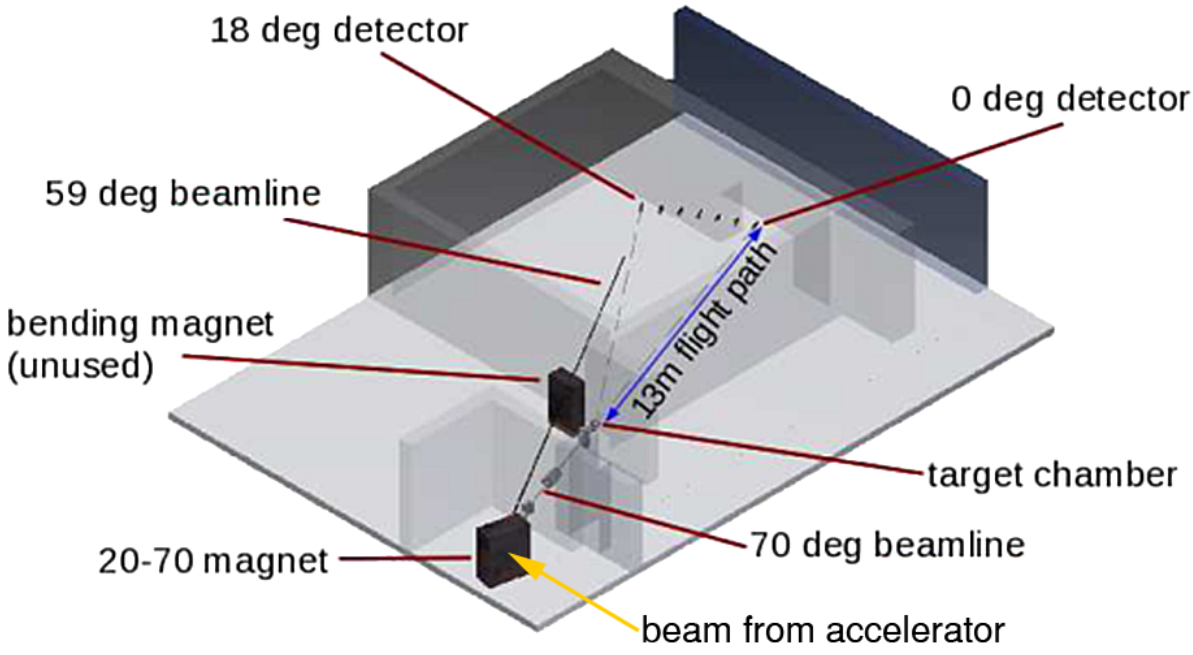

Figure 3.2: An isometric CAD rendering of the 70-degree beamline and neutron flight path. Shielding walls have been made translucent for clarity. A rough CAD model of this entire apparatus, including room dimensions, may be found with the online version of this document.

An isometric view of the high-energy portion of the $(^3He, n)$ experiment setup is shown in Fig. 3.2. The neutrons were detected by an array of liquid scintillators that spanned the angle range from 0° to 18° in 3° increments. The neutron energy was determined via TOF methods. To resolve the transition to the first 0^+ excited state from the ground state using this method at the beam energies of this experiment and with about 2 ns (FWHM) time resolution required a neutron flight path greater than 10 m. The options for setting up an experiment with such a long flight path in the tandem laboratory were very limited. This experimental layout utilized the open space in Target Room 1 and used the shielding wall between this room and the High-Energy Bay (where the target chamber was located) to reduce the background counts in the neutron detectors.

A flight path of 13 m was chosen to satisfy both the physical limitations of the accelerator lab and the energy resolution requirements of this experiment. A Monte-Carlo time-of-flight simulation (see Fig. 3.3) was developed to assess the total resolution of the system with this

flight path and the pulse width of the ^3He beam.

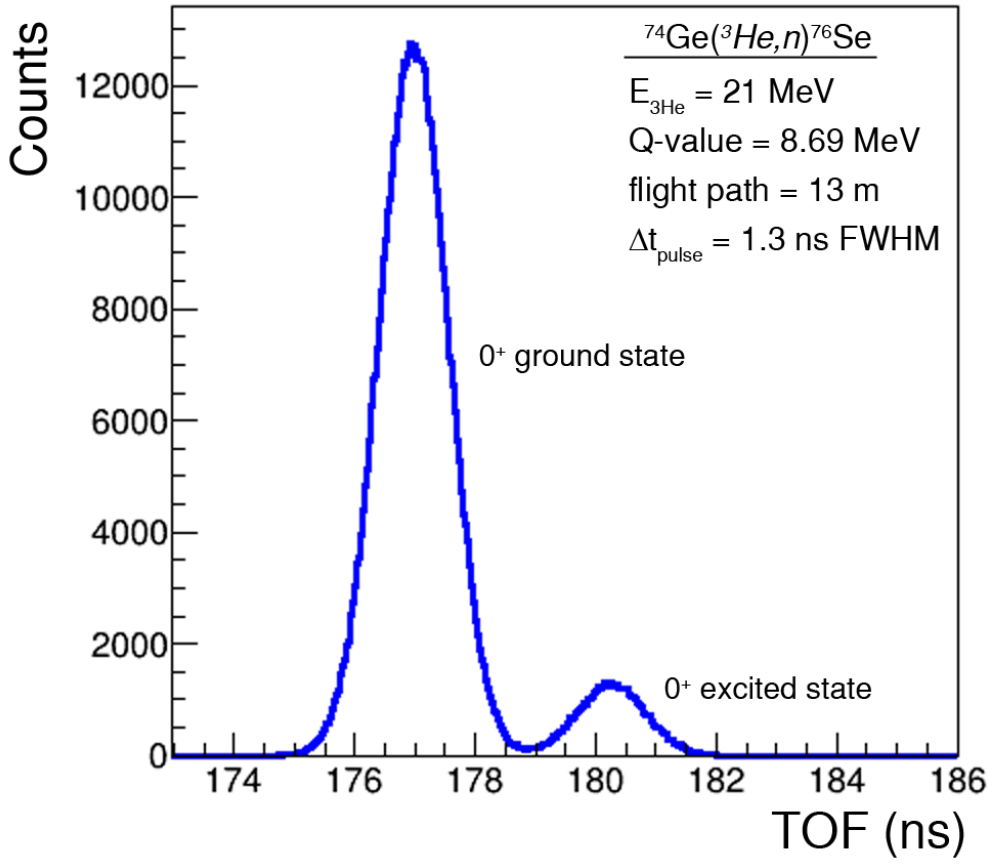

Figure 3.3: A TOF histogram for the ^{74}Ge(^3He,n)^{76}Se reaction from a Monte-Carlo simulation. The excited 0^+ state at 1.122 MeV was assumed to have 10% of the ground state strength. The source code for the simulation may be found in Appendix 8.3

This experiment required the design and fabrication of several new components. A gas recovery system was built onto the existing HIS (due to the cost of ^{3}He, discussed in chapter 6), a beam pulsing system was developed for the HIS, the 70-degree beamline was constructed with a specially modified target chamber, Ge and Te targets were fabricated (discussed in chapter 5), and an array of neutron detectors with DAQ electronics was assembled.

Section 3.1: Helium Beam Production and Pulsing

The ^{3}He-ion beam for this experiment was created using the HIS in the Low-Energy Bay of the tandem lab. The beam was pulsed using standard chopping and bunching techniques.

Typical average beam current on target was 15-50 nA with a beam pulsing repetition rate of 1.25 MHz and pulse width of about 2.5 ns.

3.1.1: HIS Operating Principles

The HIS at the TUNL tandem lab is a duoplasmatron-based ion source (Lejeune [1974a] and Lejeune [1974b]), which creates a beam of $^4He^-$ or $^3He^-$ ions for injection into the accelerator. Although the beam injection energy may be varied between 20-50 keV, maximum beam current is produced at an energy of approximately 30 keV (see below). In the course of this experiment maximum DC beam currents of 3 μA for ^{4}He and 1.5 μA for ^{3}He were obtained on the faraday cup in the Low-Energy Bay immediately before the tandem. However, a sustained beam current of 500 nA for ^{3}He was typical. A schematic diagram of the source is shown in Fig. 3.4. The HIS consists of three subsystems: the duoplasmatron and extractor, the attachment with a charge-exchange canal, and the electrostatic focusing lenses. A beam of *positive* ions is initially created by the duoplasmatron and extractor, which then pickup two electrons in the charge-exchange canal to produce the ultimately negative beam. The extractor, attachment, and focusing lenses are contained within an aluminum vacuum chamber, i.e., the source box. The source box is evacuated using an oil diffusion pump to a pressure of about 5×10^{-6} Torr.

The Duoplasmatron and extractor system has two functions. The first function is to create positive ions from an arc discharge through the helium gas. The second function is to extract these positive ions from the plasma region to form the primary ion beam. The duoplasmatron uses a hot cathode arc-discharge in an inhomogeneous magnetic field to produce ions. The probe is a pencil-shaped containment vessel made of soft iron, and is surrounded by the source head magnet. This causes an inhomogeneous, axial magnetic field to appear between the probe and the anode. (The anode is made of copper with a molybdenum insert, the plasma expansion cup is steel.) The filament is heated resistively and biased to an electric potential of +30 to +70 V relative to the anode electrode, which

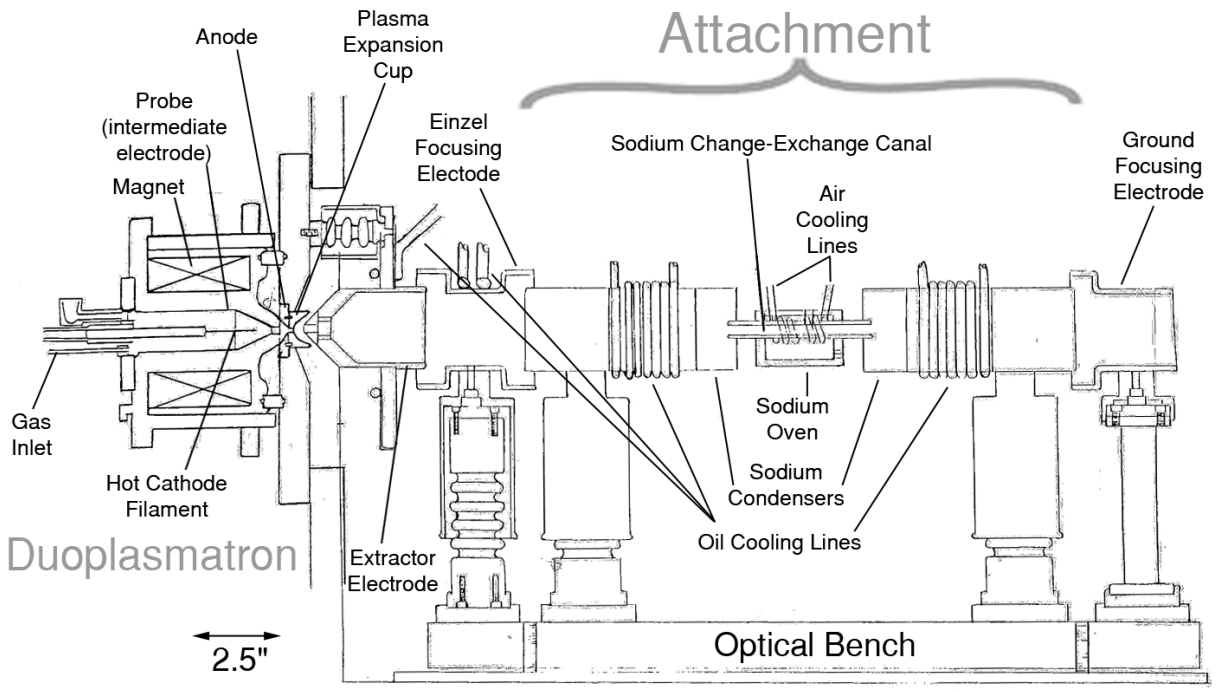

Figure 3.4: A schematic diagram of the HIS interior.

is held at ground potential. The probe is also biased to about half the electric potential difference between the filament and anode to serve as an intermediate electrode (Fig. 3.4). Gas flows through the duoplasmatron, entering at an inlet near the filament holder and exiting through the aperture in the anode electrode (Fig. 3.4). The anode and the source frame are held at ground potential, allowing the source to be operated directly from the lab AC power circuits. The arc in the duoplasmatron bottle is struck by establishing favorable conditions. A solenoidal magnetic field of nominal strength ($I \approx 0.75$ A in the bottle magnet coils) is applied, the helium gas flow to the source bottle is adjusted to have a pressure of about 500 mTorr, the bias between the filament and anode is set to about 50 V, and the filament current is slowly increased until the arc is struck, usually at filament current less than 60 A. This arc produces a weak plasma in the region around the filament, and a strong plasma sphere forms on the cathode side of the probe (see Fig. 3.6). This plasma sphere acts as a virtual cathode, and is the main source of the ionizing electrons. The majority

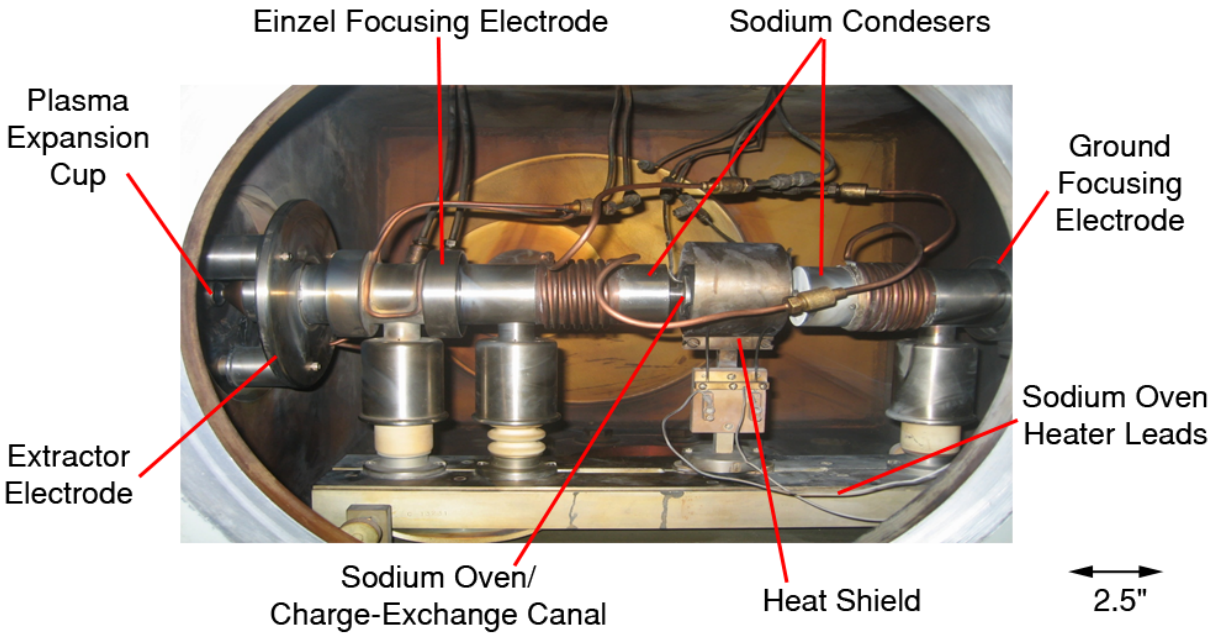

Figure 3.5: A photograph of the acceleration and focusing electrodes and the sodium oven assembly inside the HIS. The oil cooling lines are 1/4" copper tubing and the air cooling lines are 1/8" stainless steel tubing

of the ionization occurs in this region. Electrons from the virtual cathode are accelerated toward the anode and constrained to spiral along the magnetic field lines. Along this path the electrons encounter the source gas atoms and ionize them. When the ionization occurs, the electrons' energy is given up to the ionized atom, allowing the electron to migrate across the magnetic field lines. This electron migration produces a net positive potential in the field region because of the residual ions' space charge, and the potential pushes the ions out of the anode. Once through the anode the ions expand in the plasma expansion cup and are extracted from the cup by the electric field created by the voltage applied to the extractor electrode.

The attachment (which refers to the combination of the sodium condensers and charge-exchange canal/oven) also has two functions. The first function is to provide two electrons per ion inside the charge-exchange canal to make the ion beam sent to the accelerator negative. The second function is to accelerate the ion beam out of the source. The energy

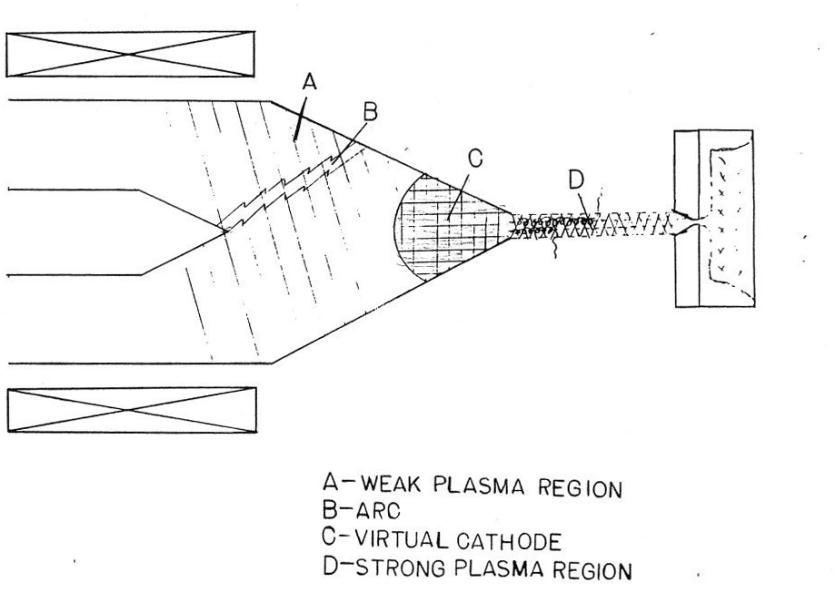

Figure 3.6: A diagram of plasma production inside the HIS duoplasmatron. (not to scale)

of the negative helium ions from the source is determined by the voltage applied to the attachment. The attachment consists of two oil-cooled condensers and the sodium charge-exchange canal/oven, which are held at a constant negative potential (see schematic diagram of the source in Fig. 3.4 and a photograph of the attachment area in Fig. 3.5).

The beam from the extractor is accelerated into the charge-exchange canal by the attachment potential after having been focused by an Einzel focusing element held at about +4 kV. In traversing the total distance from the duoplasmatron to the charge-exchange canal, the beam moves through a net potential difference equal to the attachment bias and thus enters the charge-exchange region with an energy equal in magnitude to the attachment potential (i.e., for -20 kV attachment potential, the beam energy in the canal is 20 keV) (Fig. 3.7). After passing through the first condenser, the beam enters the exchange canal, which is filled with sodium vapor from the oven. The oven is heated by the surrounding radiative heating element, which is itself surrounded by a thin steel heat shield (see photograph in Fig. 3.5). Both the heating element and the heat shield are kept at ground. In the canal, the ions can undergo a double charge-exchange with the sodium atoms. Once the charge-exchange has occurred, the beam is negatively charged and undergoes another potential change equal

in magnitude to the attachment bias in passing to the ground potential focusing element. Thus the beam exits the source with double the energy it had in the exchange canal. The sodium oven must be refilled periodically. A full load of about 6 g of unoxidized sodium lasts approximately 200 hours of source operation.

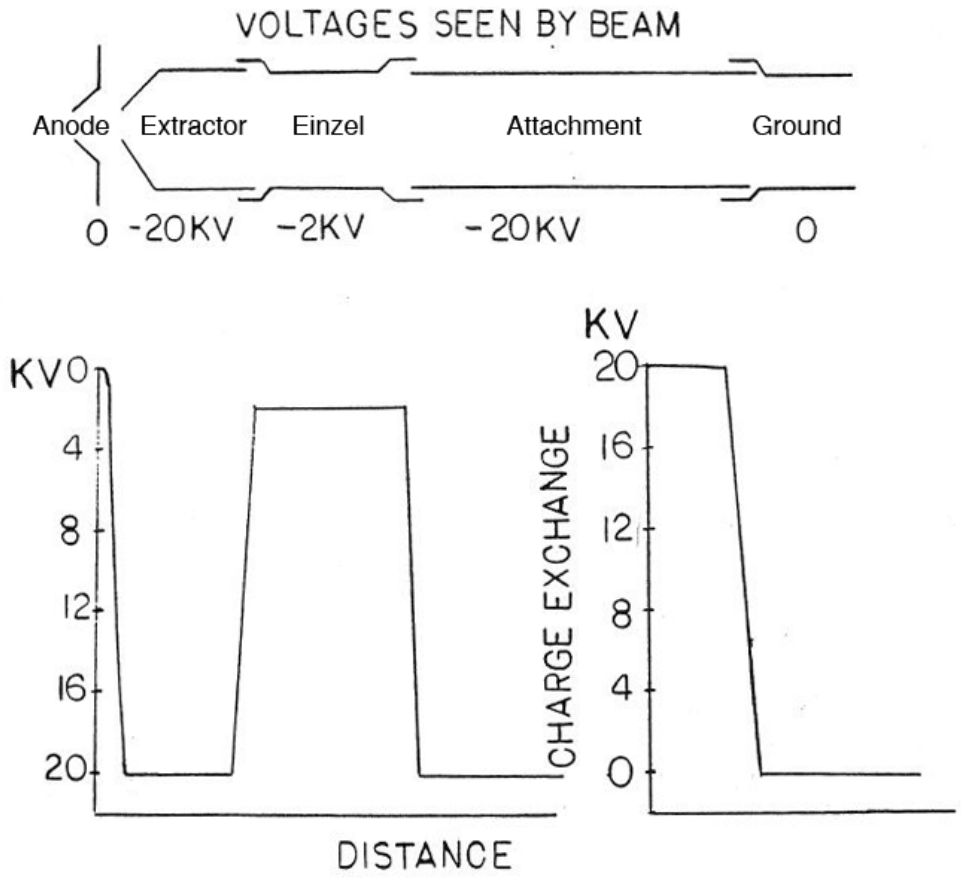

Figure 3.7: The potentials seen by the beam inside the HIS, as it passes through the acceleration and focusing electrodes.

The cross section for double charge-exchange with sodium is maximum at a ^{4}He energy of 12 keV, thus the maximum amount of beam is produced with a final energy of about 24 keV (Fig. 3.8). Double charge-exchange occurs with sodium vapor in the exchange canal in the following two-stage process (D'yachkov and Zinenko [1971]):

$$He^+ + Na^0(1s^2 2s^2 2p^6 3s^1) \rightarrow He^0(1s^1 2s^1) + Na^+(1s^2 2s^2 2p^6) \quad (3.1)$$

$$He^0 + Na^0(1s^2 2s^2 2p^6 3s^1) \rightarrow He^-(1s^1 2s^1 2p^1) + Na^+(1s^2 2s^2 2p^6) \quad (3.2)$$

The probability of electron transfer is maximized when the velocity of the helium atoms is matched to the orbital velocity of the $3s^1$ valence electron in sodium. The energy which maximizes charge-exchange for ^{3}He should therefore be lower than the ^{4}He energy by a factor of the square root of the mass ratio, $\sqrt{4/3}$. Therefore, maximum ^{3}He beam current should be produced when ^{3}He ions pass through the exchange canal with an energy of 10.4 keV (e.g. 10.4 kV attachment bias).

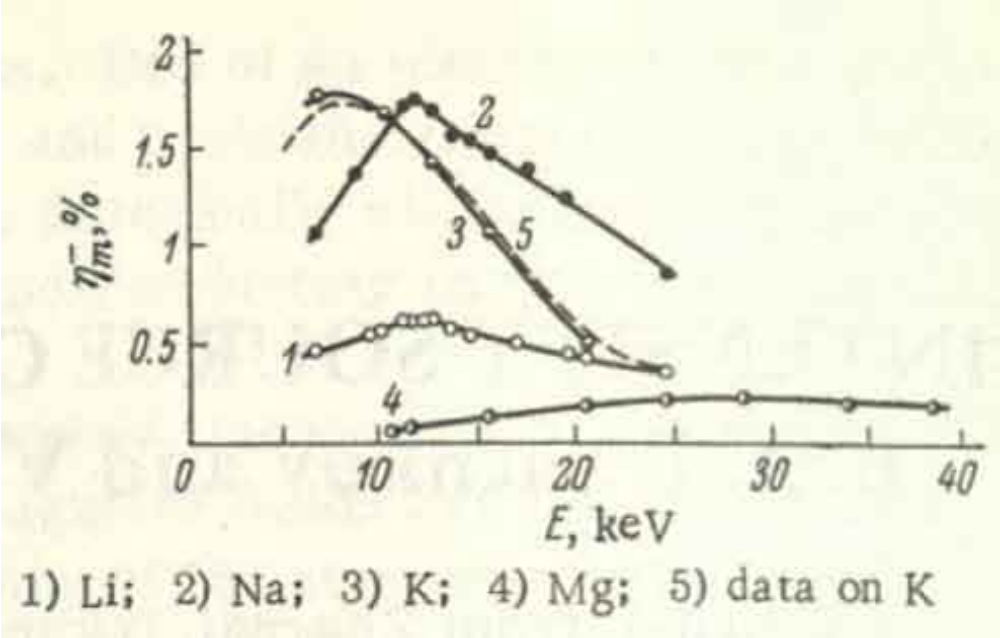

Figure 3.8: A plot of η_m^-, the percentage yield for double charge-exchange between helium and different target materials. (Image photocopied from D'yachkov and Zinenko [1971])

For this experiment the attachment bias was considerably higher than 10.4 kV to improve the time resolution of the beam pulsing. Tests conducted on the beam pulsing system with the HIS indicated that the main factor contributing to the finite width of beam pulses was the energy spread in the beam emerging from the source. By increasing the attachment bias

and thus the beam energy from the source, the fractional energy spread in the beam was reduced, producing more tightly bunched beam pulses (Wender et al. [1980]). An attachment bias of -21 kV (beam energy 42 keV) was chosen in optimizing the tradeoff between the beam pulse width and magnitude of the beam current on target.

The function of the focusing elements is to electrostatically focus the ion beam before transport to the accelerator. There are two focusing elements in the HIS, the Einzel focusing element which is adjustable and the grounded element which at the exit of the source, shown in Figs. 3.4 and 3.5.

DC voltages are applied to the extractor, focus, and attachment electrodes through the respective oil cooling lines for each. More information, including operating and maintenance procedures, may be found in the HIS operations manual.

3.1.2: Optimum Source Parameters for Beam Pulsing

This experiment required the beam to be pulsed with a width no greater than 3 ns FWHM on target. Tests were conducted using a ^{4}He beam to determine the settings for source components, including the electrode biases and filament current, that minimize the width of beam pulses. A minimum pulse width of 1.1 ns FWHM was achieved.

Several elements of the HIS may be adjusted to vary the beam it produces. It was determined that a high filament heating current, a low filament/probe bias, a high source gas pressure, and (as mentioned before) a high attachment bias generally results in the best beam pulsing on target. A comparison of the standard HIS parameter settings with the values that produced 1.1 ns pulse width is shown in table 3.1. These settings are thought to reduce energy spread by creating a cooler plasma in the duoplasmatron, e.g., a smaller spread in the Maxwell-Boltzmann distribution of ion energies.

Of note, about 2 ns FWHM is the minimum pulse width achieved with a chopped and bunched ^{3}He beam during this experiment. Undetermined changes within the HIS that occurred during the frequently required sodium reloads and source cleanings made recorded

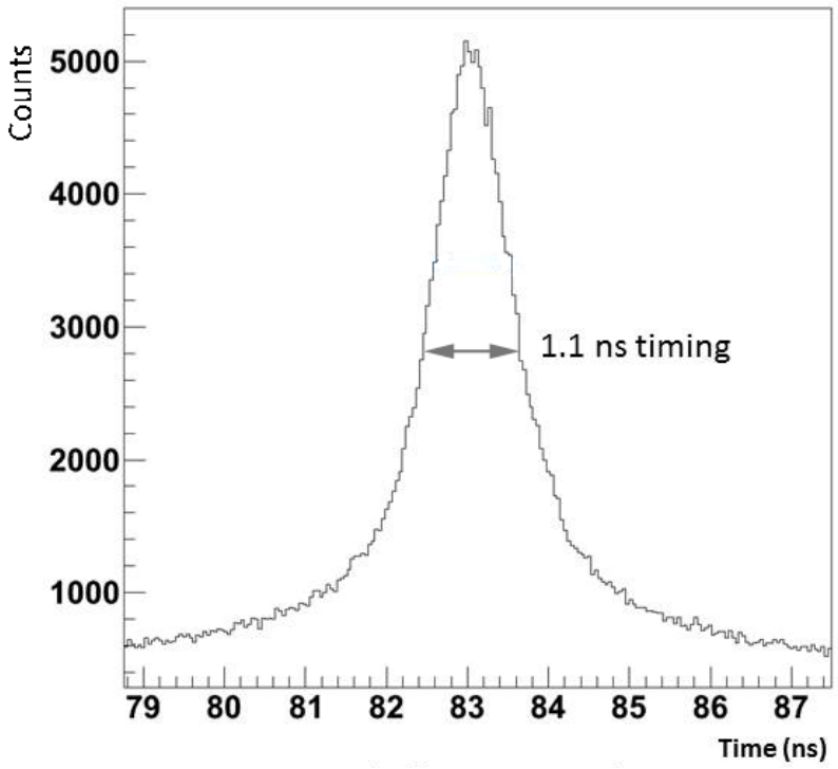

Figure 3.9: A measured TOF histogram for the detected alpha particles scattered elastically from a gold foil. This histogram represents an example of the best pulse width achieved with a ^{4}He beam. The beam was pulsed using bunching only, e.g., without chopping the beam. Chopping the beam removes the grass (i.e., the symmetric tails) on either side of the timing peak (discussed in section 3.1.3). While chopping reduces the average beam-on-target (BOT), it should not decrease the amount of charge in any given beam burst. However, the minimum beam pulse width with chopping was observed to be greater than without. In general, a higher beam current produced narrower timing peaks.

source settings non-transferable between maintenance cycles. Continual sparking on the biased oil cooling lines caused wide variation in the BoT. This necessitated the insertion of a veto that prevented the DAQ from accumulating data when the BoT dropped below a set level, about 20% below the average BoT.

3.1.3: Beam Pulsing

This section describes the particle beam pulsing system at TUNL, which is necessary for measuring the time-of-flight of the detected neutrons in the measurements carried out for this experiment.

Table 3.1: HIS Parameter Settings

Source Parameters	Standard	1.1 ns timing
filament heating current (A)	62.5	75.0
filament/probe bias (V)	80/36	20/19
Arc current (A)	2.1	2.0
Source magnet current (A)	1.5	1.675
Focus bias (kV)	2.4	4.4
Extractor bias (kV)	16.5	22.5
Attachment bias (kV)	15.0	24.0
Source gas pressure (Torr)	0.25	4.0
Beam Parameters		
BoT (nA)	925	650
Pulse width (ns)	3.8	1.1

The continuous stream of ions (i.e. DC beam) leaving the ion source passes through two sets of deflection plates which have a periodic time-dependent voltage applied between the plates of each set. The applied voltage produces a time-dependant electric field between the plates that is perpendicular to the beam axis, causing a deflection in the beam, i.e., adding a transverse component to the velocity of the beam particles. Particles deflected beyond a certain amount do not pass through an aperture downstream, resulting in periodic segmenting of the beam.

The two sets of chopper plates are termed the main chopper and the auxiliary chopper. One plate on the main chopper is driven by a sinusoidally-oscillating voltage at 2.5 MHz and the other plate is held at ground. This produces a chopped beam with a frequency of 5 MHz (a beam segment passes through the beam limiting aperture every time the voltage on the driven plate crosses zero, every 200 ns). The peak to peak voltage ($\sim$1 kV) on the main chopper is adjusted to discard 80% of the beam, resulting in 40 ns (i.e. 0.2 $\times$ 200 ns) long beam segments. This is important to ensure that the chopped beam segments fit fully into the phase acceptance of the double-gap buncher.

The auxiliary chopper functions to regularize the periodicity of the beam segments created by the main chopper. Because the velocity of the beam particles entering the main chopper

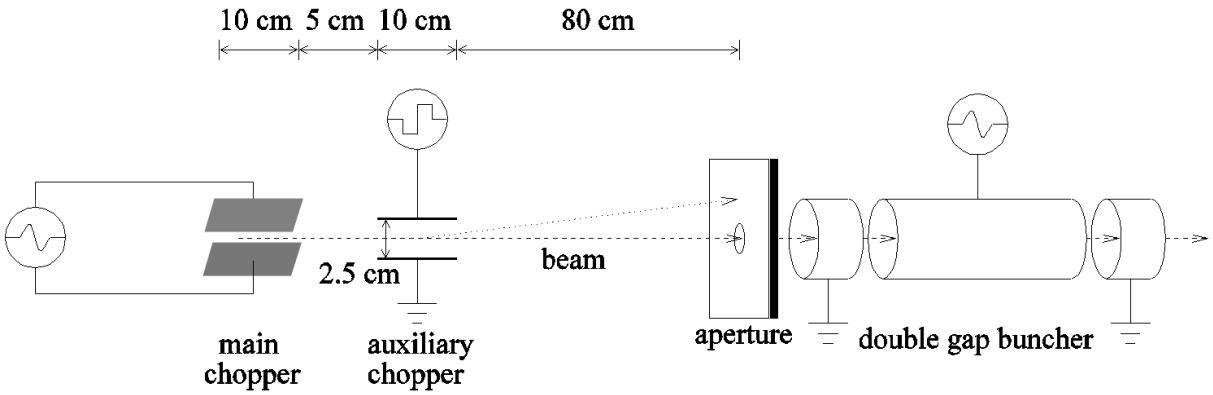

Figure 3.10: A diagram of the system for producing a pulsed beam in the tandem lab at TUNL. The chopper removes sections of the DC beam at regular intervals. Each resulting beam segment then enters the double-gap buncher, which slows the head and speeds up the tail of the segment, causing it to become spatially compressed by the time it reaches the target. Details of the system are explained in the text.

plates can be in a different direction than the optical axis through the center of the plates, the effective zero-crossing of the electric field may not coincide with the zero-crossing of the voltage applied to the driven plate. This condition results in a bimodal pattern in the time separation between sequential beam segments. A net voltage with a rectangular waveform is applied across the plates of the auxiliary chopper to selectively discard the beam segments created by the main chopper. The auxiliary chopper allows one out of every 2^n beam segments to pass through the beam limiting aperture, where n is an integer with a value $n \geq 1$. This selectively produces beam pulses with a single period between sequential pulses. This mechanism for regularizing the beam pulsing period reduces the beam current by some power of two, i.e., allowing through every second, fourth, eighth beam segment. Both plates of the auxiliary chopper are driven by a rectangular waveform voltage, 180° out of phase, at a frequency of $5/2^n$ MHz. For this experiment, the auxiliary chopper was operated at 1.25 MHz (passes every fourth beam segment from the main chopper) with an acceptance time window of about 100 ns.

To keep the choppers independent, the conducting plates of the main chopper are oriented orthogonal to the auxiliary chopper plates (i.e., the main chopper deflects the beam

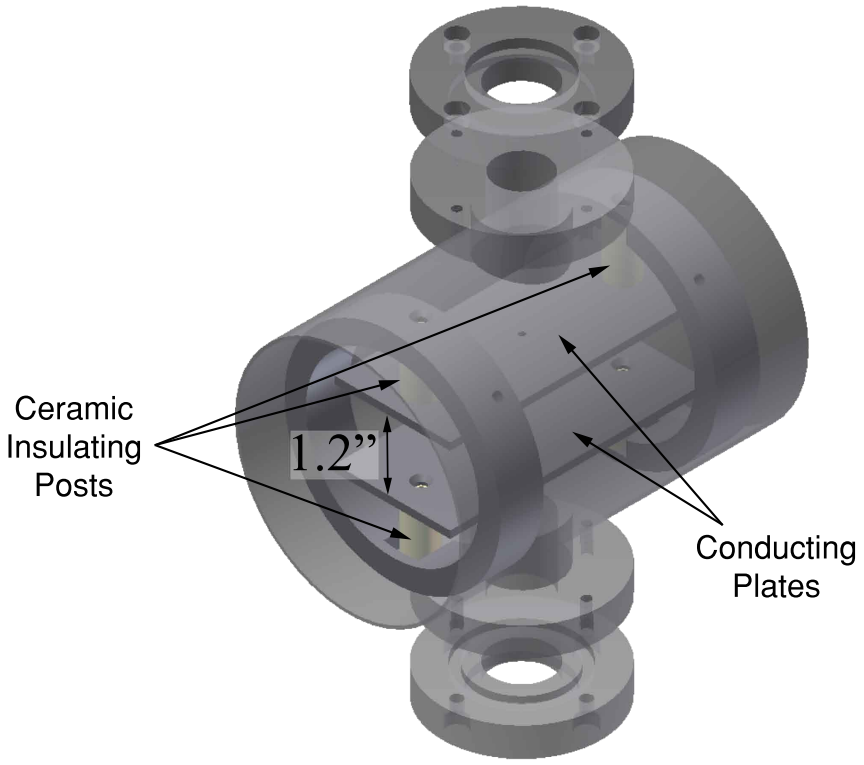

Figure 3.11: A CAD rendering of the chopper plate assembly, which consists of a pair of electrically-isolated parallel conducting plates. One plate is driven by an oscillating voltage, and the other plate is either driven with an oscillating voltage that is 180 degrees out of phase or kept at ground potential. The chopper plate assembly was designed and fabricated at TUNL. See online version for CAD file.

horizontally and the auxiliary chopper vertically).

The double-gap buncher serves to spatially compress each beam segment that passes through the aperture. It does this by speeding up the second half and slowing down the first half of a each beam segment. The buncher consists of three sequential and coaxial conducting cylinders. A long cylinder in the middle is driven by a sinusoidally-varying voltage at 5 MHz and two shorter cylinders on either end are held at ground potential. The ions in the beam segments are accelerated by the time-varying electric field in the gaps between the cylinders. Because the ions are negatively charged, an electric field parallel to the beam's velocity will decrease the ions' speed and an electric field anti-parallel to the beam's velocity will increase the ions' speed. Therefore, the applied voltage must be phased so each beam segment enters

the first gap while the voltage is negative and increasing such that it reaches zero when the first half of the segment has just passed the gap. Furthermore, the length of the central cylinder must be adjusted so that $n + 1/2$ periods of the applied voltage have passed in the time it takes a segment to traverse the cylinder, where n is an integer with $n \geq 0$. That way, when a beam segment first enters the second gap the applied voltage is positive and decreasing such that it reaches zero when this segment is halfway through the second gap. Thus the velocity of each beam segment is continuously modulated along its length and when the peak to peak voltage applied to the central cylinder is tuned correctly, the time focus of the charge in each beam segment will occur at the location of the capacitive pickoff unit (see section 3.1.4) immediately before the target chamber.

A quantitative examination of the bunching process explains the choice of a sinusoidally-varying driving voltage. Consider a beam segment of particles with energy E_o and a length such that a time τ elapses for the entire segment to pass any one point. Let the bunching plane (i.e. the point where the velocity modulation occurs) be located at $x = 0$, the position of the "head" of the beam segment be at $x = 0$ at time $t = 0$, and the target be located at $x = x_o$. The condition for proper bunching is to have every particle in the segment located at $x = x_o$ at a time $t = t_o$. Let the speed of particles at the head of the segment be

$$v_o = \sqrt{\frac{2E_o}{m}} = \frac{x_o}{t_o} \tag{3.3}$$

(using $E = \frac{1}{2}mv^2$). Particles behind the head of the segment have less time to reach x_o and must move faster. Specifically, these later particles have $0 < t < \tau$ less time to reach x_o. Therefore, particles crossing the bunching plane at time t must have their velocities modulated from v_o to

$$v(t) = \sqrt{\frac{2E(t)}{m}} = \frac{x_o}{t_o - t} \tag{3.4}$$

where

$$E(t) = \frac{1}{2} m x_o^2 \left(\frac{1}{t_o - t} \right)^2$$

$$= \frac{1}{2} m \left(\frac{x_o}{t_o} \right)^2 \left(\frac{1}{1 - {}^{t}/_{t_o}} \right)^2 \tag{3.5}$$

$$= \frac{E_o}{\left(1 - {}^{t}/_{t_o}\right)^2}$$

For a 42 keV ^{3}He particle, $v_o = 0.164$ cm/ns. Since a particle spends the bulk of the total time-to-target going the $\sim$2 m between the buncher and the tandem, $t_o \gtrsim 1.2\ \mu s$. Since the main chopper discards 80% of the beam at 5 MHz, $\tau = 40$ ns. Therefore, $t_o \gg \tau$, and equation 3.5 is well-approximated by the Taylor expansion

$$\frac{1}{\left(1 - {}^{t}/_{t_o}\right)^2} \approx 1 + 2\frac{t}{t_o}$$

Therefore,

$$E(t) \approx E_o \left(1 + 2\frac{t}{t_o} \right) = E_o + \Delta E_o \tag{3.6}$$

where

$$\Delta E_o = \frac{2 E_o t}{t_o} = q V_{buncher}(t) \tag{3.7}$$

where q is the charge of a particle in the beam segment (1 unit of electron charge in this work) and $V_{buncher}$ is the velocity-modulating voltage applied by the buncher.

Equation 3.7 implies that the buncher voltage should be linearly ramped and that the peak buncher voltage for this work is $V_{buncher} \lesssim 2.8$ kV. Unfortunately, producing such a "sawtooth" voltage waveform is technically arduous. However, a sinusoidal waveform is sufficiently linear within a time-window centered on the zero-crossing with a width equal

to ∼20-30% of the waveform's period (i.e., ∼40 ns for a 5 MHz waveform) (Milner [1979]). In addition, it is straightforward to produce a sinusoidal voltage waveform with ∼10 kV amplitude and 200 ns period using a common laboratory rf amplifier. Therefore, the buncher was driven by a 5 MHz sinusoidally-varying voltage that was phased such that a 40 ns long beam segment entered the first buncher gap 20 ns before the waveform's postive-sloped zero-crossing. For further details see Wender et al. [1980] and Howell [1984].

3.1.4: Measuring Neutron ToF Using a Capacitive Pickoff Unit

The neutron ToF from target to a given detector is measured using a TDC. The start signal to the TDC is generated by the CFD (i.e. gate) output of the MPD-4 module for the detector and the stop signal is the delayed signal from the capacitive pickoff unit located on the beamline immediately before the target chamber.

As a beam bunch enters the pickoff unit, charge is induced on the tube and current flows through the attached BNC connector. When the bunch leaves the pickoff unit, the induced charge is released, and current flows in the opposite direction. This creates a bipolar signal, where the zero-crossing corresponds to the time when the center of the beam bunch is at the center of the pickoff.

It would be logical to use this as the start signal for measuring neutron time-of-flight. However, because signals from the pickoff are generated at a MHz rate, using them to start the TDC would create excessive deadtime (since most beam bunches do not produce a signal in any detectors). To avoid this problem, the detector CFD signal is used to start the TDC and the delayed pickoff signal is used to stop it. This creates a time-of-flight histogram in which time decreases with increasing channel number (i.e., time runs backwards).

The raw bipolar signal from the pickoff unit is amplified and converted to a logic signal for use as the TDC stop signal in the neutron time-of-flight measurements. Two preamplifiers (Phillips Scientific model 6954 x10 and x50, bandpass 100 kHz - 1.5 GHz) were connected directly to the pickoff unit, providing a factor of 500 amplification. The signal is then

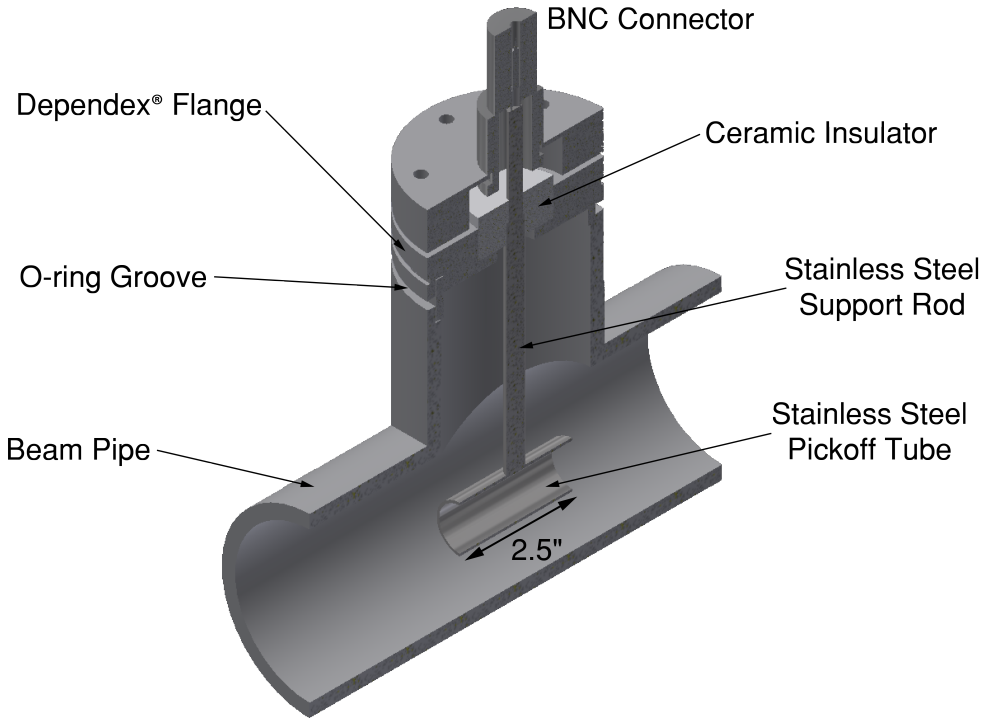

Figure 3.12: A CAD rendering of the capacitive pickoff unit on the 70-degree beamline in cross-sectional view. It consists of an electrically-isolated steel tube centered inside the beam pipe through which the beam passes. Vacuum seals are made between the steel rod and insulator (using Armstrong A-12 epoxy, a general purpose adhesive manufactured by Loctite®), the insulator and the Dependex® flange (A-12 epoxy), and the Dependex® flange and the beam pipe (Viton™ o-ring). The pickoff unit was designed and fabricated at TUNL. See online version for CAD file.

sent to the Control Room via a low-loss cable. The signal is then amplified again using a linear amplifier (LRS model 133B dual linear amplifier) by a factor of 2 or 3 amplification (depending on the magnitude of the beam current). The amplified signal is inverted using a linear fan and sent to a zero-crossing discriminator (EG&G model T140/N quad zero-crossing discriminator), which produces a NIM logic pulse.

Section 3.2: 70-Degree Beamline and Target Chamber

A new beamline was constructed off the 70-degree port of the vacuum chamber of the 20-70 magnet (see Fig. 3.15). To establish the 70-degree line, 2-inch etched-glass optical targets were placed on both the front and back 70-degree ports of the 20-70 magnet and

Figure 3.13: An oscilloscope trace (yellow) of the pickoff signal from a pulsed ^{3}He beam on the 70-degree line at TUNL. Amplifier noise is apparent at times beyond the signal. The blue trace is the logic timing pulse corresponding to the zero-crossing of the pickoff signal; it is used to stop the TDC. For this experiment, the beam was pulsed at 1.25 MHz.

sighted using optical levels. The separation between these ports is 134±1 cm and the glass targets were found to have less than 1 mm of wiggle on the Dependex® fittings of the 20-70 magnet. (Dependex® is a vaccum flange standard designed by the now defunct High Voltage Engineering Corporation. See Stockli [1989].) Thus the beamline and fiducial markers were aligned to well within ±0.1° of the line defined by the two 70-degree ports on the magnet. Since the 12.7 cm diameter neutron detectors at a distance of 13 m subtend an angle of 0.56°, this alignment was more than adequate. (For future reference, an etched glass target mounted to the wall behind the 20-70 magnet was found to be in vertical but not horizontal

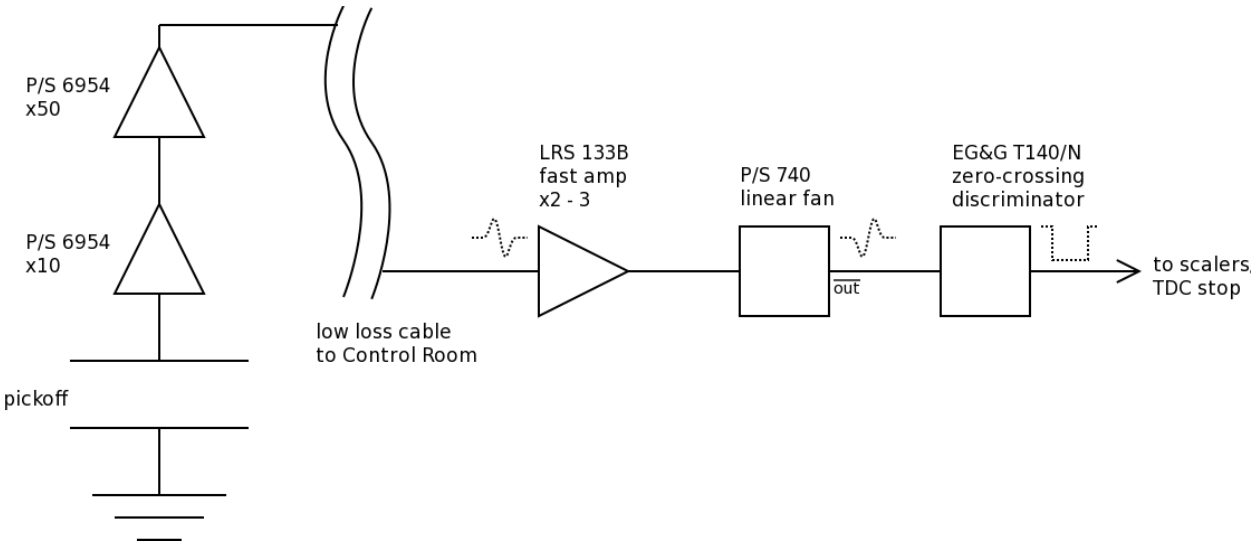

Figure 3.14: A schematic diagram of the electronics used to process the raw pickoff signal.

alignment with the 70-degree line.)

Several fiducial markers were installed while surveying this beamline. Two round brass plates (4 cm diameter) were epoxied to the floor, one in the High-Energy Bay and one in Target Room 1, along the 70-degree line. A center punch was used to make a mark on the plates directly under the level. Three plumb bob holders were installed, one in the High-Energy Bay on the wall between Target Room 1. The other two were placed in Target Room 1, one on the wall between the High-Energy Bay and the other on the wall between the hallway in a position just above the doorway.

Many components on the new beamline were obtained from the TUNL equipment inventory. Several components were designed and fabricated at TUNL, including the table and mount for the target chamber. CAD files for these components may be found with the online version of this document.

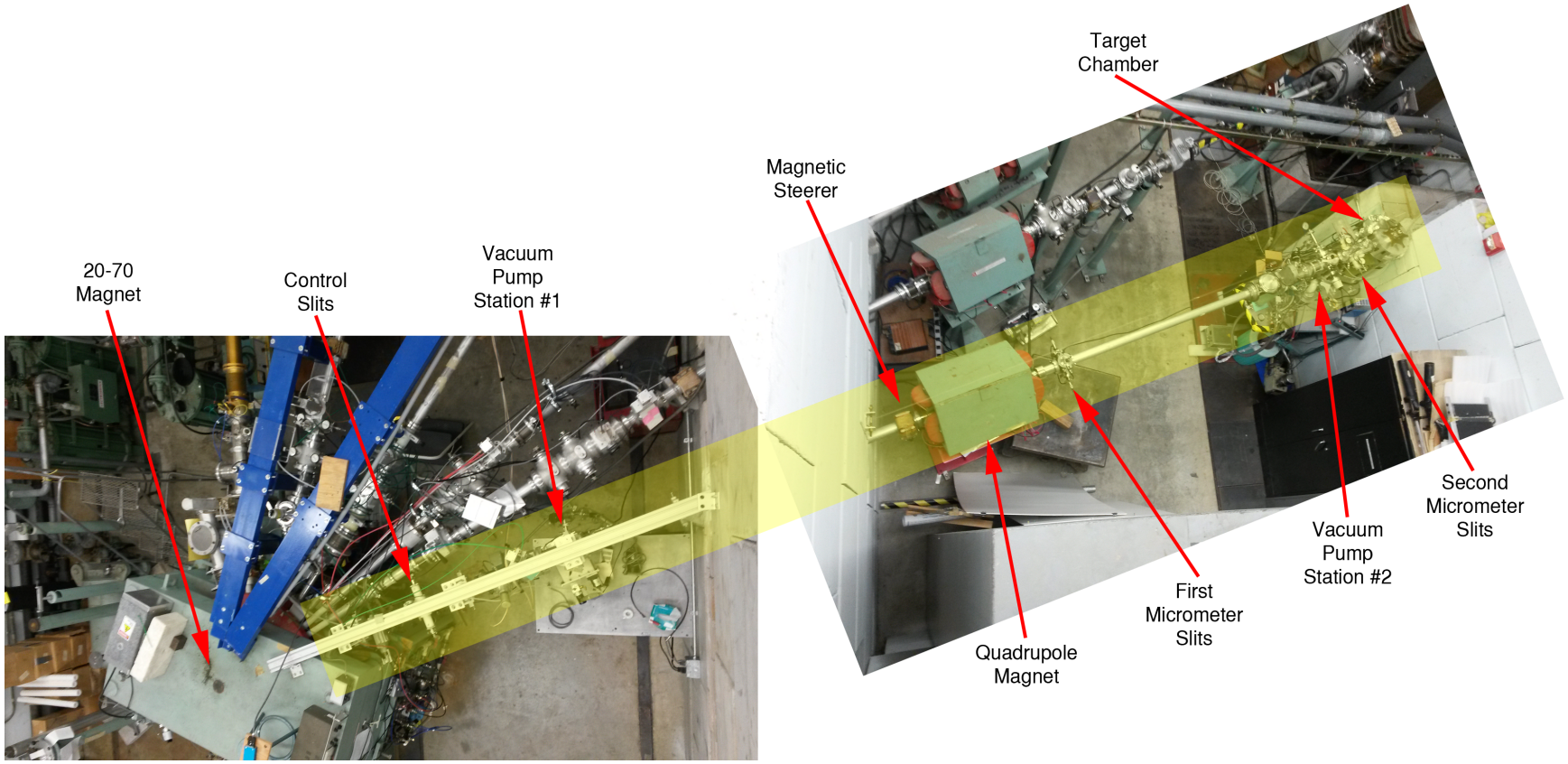

Figure 3.15: A composite photograph showing an overhead view of the 70-degree beamline, which has been highlighted in yellow for clarity. The distance from the center of the 20-70 magnet to the center of the target chamber is about 7.6 m. The first half of the beamline is supported from above by a piece of 80/20® extruded aluminum. At a later date, the support structure for other beamlines was changed to an overhead design using a piece of steel channel (painted blue in the left photograph), which was found to be more structurally robust than the 80/20®.

The 70-degree beamline was the first beamline at TUNL to be supported from above (as opposed to using steel posts to provide support from below). A piece of 80/20® extruded aluminum was bolted to the yoke of the 20-70 magnet on one end and anchored to a concrete shielding wall on the other end (see Fig. 3.15). Beamline components were then hung from this support using steel rods. Two high-vacuum pumping stations maintained a vacuum of at least 10^{-5} Torr in the beamline and target chamber. The first pump station, approximately 2 m beyond the 20-70 magnet, consists of a Varian® Model TV-301 Navigator turbomolecular pumped backed by a Trivac® Model D8A rotary-vane pump. The second pump station, just before the target chamber, consists of a Pfeiffer-Balzers® Model TPH-170 turbomolecular pump, also backed by a D8A rotary-vane pump. At both pump stations, a Balzers® Model PKR 250 full range gauge measures the absolute pressure.

Two sets of aperture slits were installed on the beamline downstream from the accelerator control slits. These two micrometer slits define the beam axis to target. There are no steering devices beyond the first set of micrometer slits to ensure the beam axis passes through the target. When tuning beam to target, the first steerer is used to minimize beam on the first micrometer slits, and the second steerer is then used to minimize beam on the second set while maximizing beam on target. Each slit was fabricated from tantalum sheet (0.020-0.062 inches thick, CAD files available online) and had approximately 50 μm of lead evaporated onto the beam-facing surface to reduce the neutron background. A lead collimator with a circular aperture was installed immediately before the target chamber entrance to reduce beam spray from the slits. Because lead melts at a low temperature, great care must be taken when tuning beam down the 70-degree leg. No single component on this leg may be exposed to more than 1.5 W of beam power and less than 0.5 W is recommended all slits. Excessive heating of the lead coating will rapidly melt this protective layer. Damage to the lead coating is indicated by a sudden unexpected spike in radiation levels. The beam power is given by

$$P = I \times E \times \frac{1}{charge\ state} \tag{3.8}$$

where P is the beam power in W, I is the beam current in μA, E is the beam energy in MeV, and "*charge state*" is the charge of a single beam particle in electron charges. For example, if 0.1 μA of doubly-ionized ^{3}He at 30 MeV is incident on a beamstop, that beamstop experiences 1.5 W of heating.

An existing target chamber was modified for this experiment and installed at the end of the 70-degree beamline, just before the wall between Target Room 1 (Fig. 3.16). Concrete blocks in this wall were removed to create a passageway through which neutrons could pass to reach the detectors in Target Room 1. This wall served to shield the detectors from beam-correlated neutron background. The chamber had turntables on the top and bottom for mounting charged particle detectors and a thin steel window which allowed neutrons to pass through with negligible attenuation.

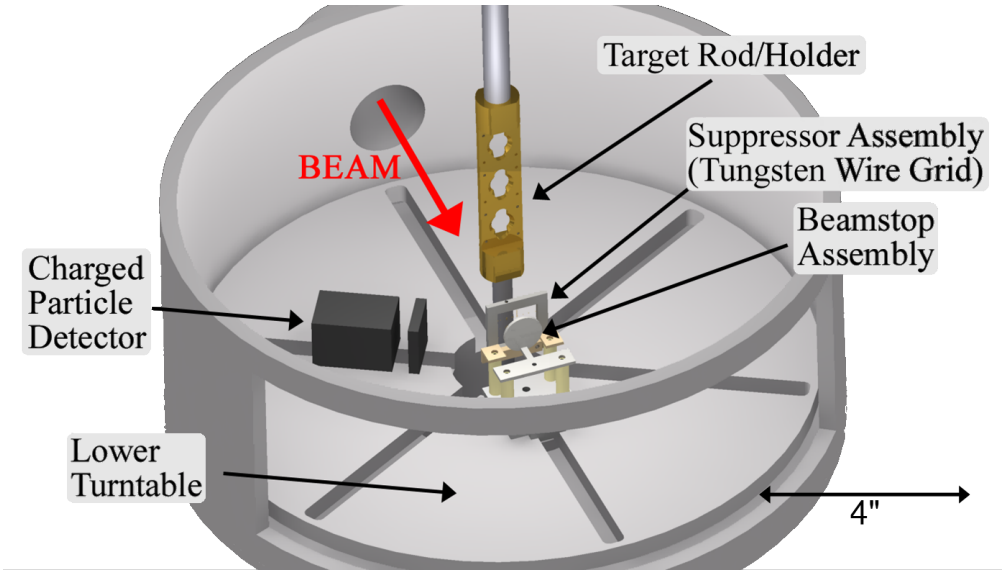

Figure 3.16: A CAD rendering of the target chamber at the end of the 70-degree beamline. The chamber was modified by machining the large neutron window behind the beamstop. A piece of 20 mil stainless steel was attached with A-12 epoxy to make a vacuum seal. The remainder of the chamber was made from aluminum and the target holder was made of brass. The upper turntable has been removed in this visualization. See online version for CAD file.

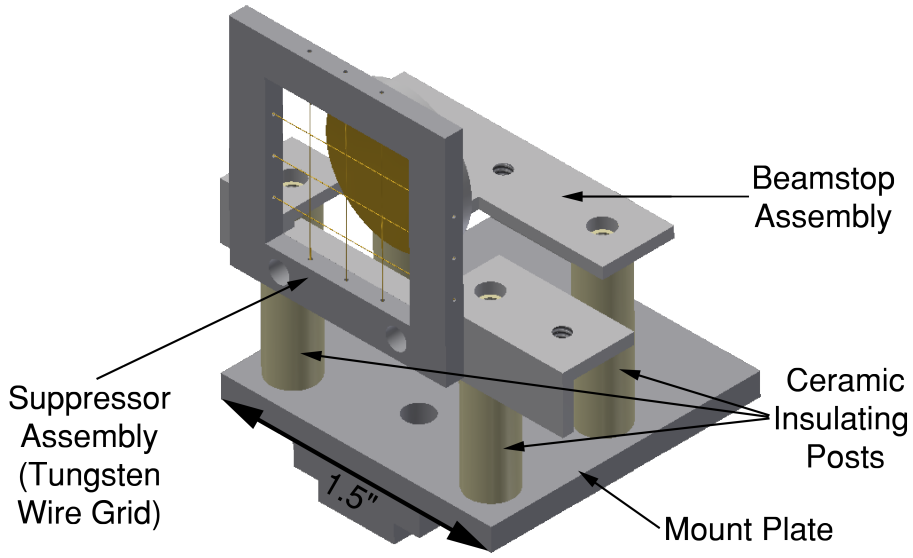

Figure 3.17: A CAD rendering of the beamstop and suppressor inside the 70-degree target chamber, which was designed and fabricated at TUNL. The suppressor grid was biased to -175 VDC. The beamstop and suppressor were electrically isolated from the chamber by cylindrical ceramic posts. Other components in the assembly were made of aluminum. A piece of lead was attached to the beamstop to reduce background neutrons. The beamstop was placed within 2.5 cm of the target to ensure that all neutrons between 0° and 18° passed through it. See online version for CAD file.

Section 3.3: Detectors

Three types of detectors were used for this work. Liquid-scintillator neutron detectors were positioned at 13 m from the target to measure neutron yields from the target (see Fig. 3.18). A CsF scintillator detector was placed just below the target chamber to assess the timing characteristics of the pulsed beam. An E-ΔE silicon charged particle detector telescope was placed in the chamber at 120° to monitor the target thickness and assess beam timing.

Figure 3.18: A photograph of the liquid-scintillator neutron detector array. 21 detectors were positioned between between 0° and 18° in 3° increments. Three detectors were placed at each angle to increase the solid angle coverage. The middle detectors are placed at beam height, approximately 69.5" from the floor.

3.3.1: Neutron Detectors

NE-213/BC-501A[1] liquid-scintillator detectors manufactured by Bicron/Saint-Gobain[2] were chosen for their relatively high neutron efficiency and excellent PSD capability (see Fig. 3.19). The application of PSD reduced the number of counts in the ROI by about a factor of 30. These detectors were biased with a LeCroy model HV 4032A high voltage power system.

[1]Data sheet may be found at www.crystals.saint-gobain.com/sites/imdf.crystals.com/files/documents/sgc-bc501-501a-519-data-sheet_69711.pdf

[2]Currently manufactured by Saint-Gobain Crystals under the name "Bicrocell." A data sheet may be found at www.crystals.saint-gobain.com/sites/imdf.crystals.com/files/documents/organics-brochure.pdf

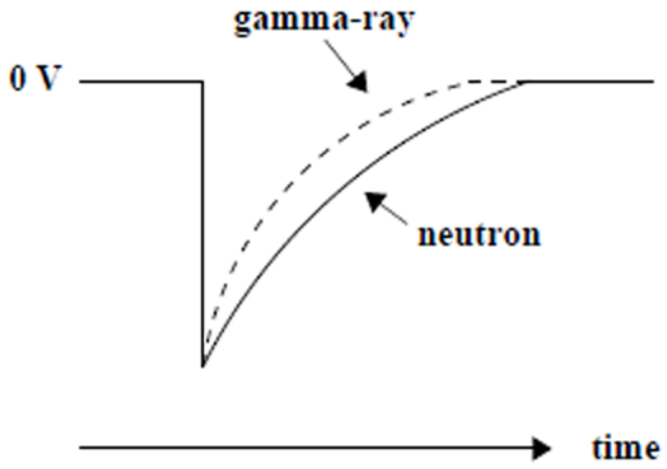

Figure 3.19: An example of detector signals corresponding to a neutron and a gamma-ray with the same pulse height in a liquid organic scintillator that has good PSD properties. The differences in the decay times of the signals make particle identification possible. This figure was taken from Crowell [2001].

Table 3.2: Neutron detector geometry

Angles	0°-18° $\pm$ 0.1° in 3° steps
Detector Size	5 inch diameter $\times$ 2 inch thick active volume
Flight Path	13.025$\pm$0.005 m target-to-center of active volume

The pulse height signal of each neutron detector was calibrated using ^{137}Cs and ^{22}Na sources. time-of-flight histograms were produced with a PH cut at 1x Cs (i.e., 477 keV, the maximum energy attainable by the Compton scattering of an electron by a 662 keV gamma from the decay of ^{137}Cs) and a PSD cut set visually to exclude as many gammas as possible without substantial loss of neutron detector efficiency. A second PH cut was made to exclude high PH gammas, which had overflow PSD into the neutron regime.

Detectors were placed in Target Room 1 at lab angles between 0° and 18° in increments of 3°. Detector positions were determined using Invar rods and a theodolite. Paper targets were glued to the floor 13 m from the center of the germanium target at each angle. To increase the solid angle, a stack of 3 identical detectors was used. One detector was placed at the beam height, one above, and one below. The distance between the centers of adjacent detectors was 17.3 cm.

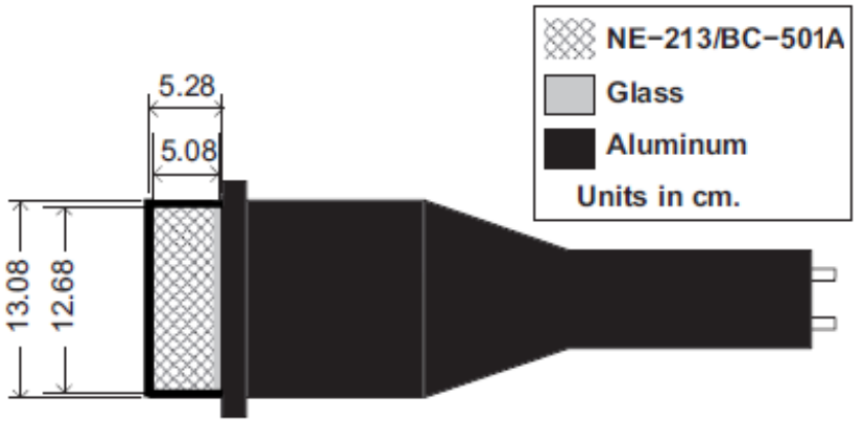

Figure 3.20: Cross-sectional diagram of a neutron detector used to record neutrons from the (3He, n) reaction. An aluminum cell, filled with BC-501A liquid scintillator, and a glass window is optically coupled to a Hamamatsu R1250 type PMT. This figure was taken from Gonzlez-Trotter et al. [2009].

3.3.2: Solid State Detectors

Silicon barrier detectors are reverse-biased diodes that produce a pulse of charge directly proportional to the energy deposited by charged particles in the depletion region of the silicon. A thin "ΔE" detector allows particles to pass through while producing a signal proportional to the particle's energy loss (i.e., ΔE). Particles with differing charge and/or mass experience differing energy loss in a given thickness of silicon. A thick "E" detector completely stops charged particles and therefore produces a signal proportional to each particle's energy. The combination of a ΔE detector followed by an E detector (an E-ΔE telescope) enables charged particle identification by comparing the ratio ΔE:E for each particle. Furthermore, sub-nanosecond rise times in thin silicon barrier detectors permit the signal to be used for timing purposes as well.

A silicon barrier E-ΔE telescope was placed in the target chamber at 120° beam-right to monitor the beam pulse timing and target thickness by elastically scattered $^{3}He^{++}$. The ratio of $^{3}He^{++}$ yields to integrated beam current was constant for each target throughout the experiment. This indicated a negligble change in the target thickness. The E detector was an ORTEC model BR-020-050-2000 and serial number 26-346I. It was biased to -500

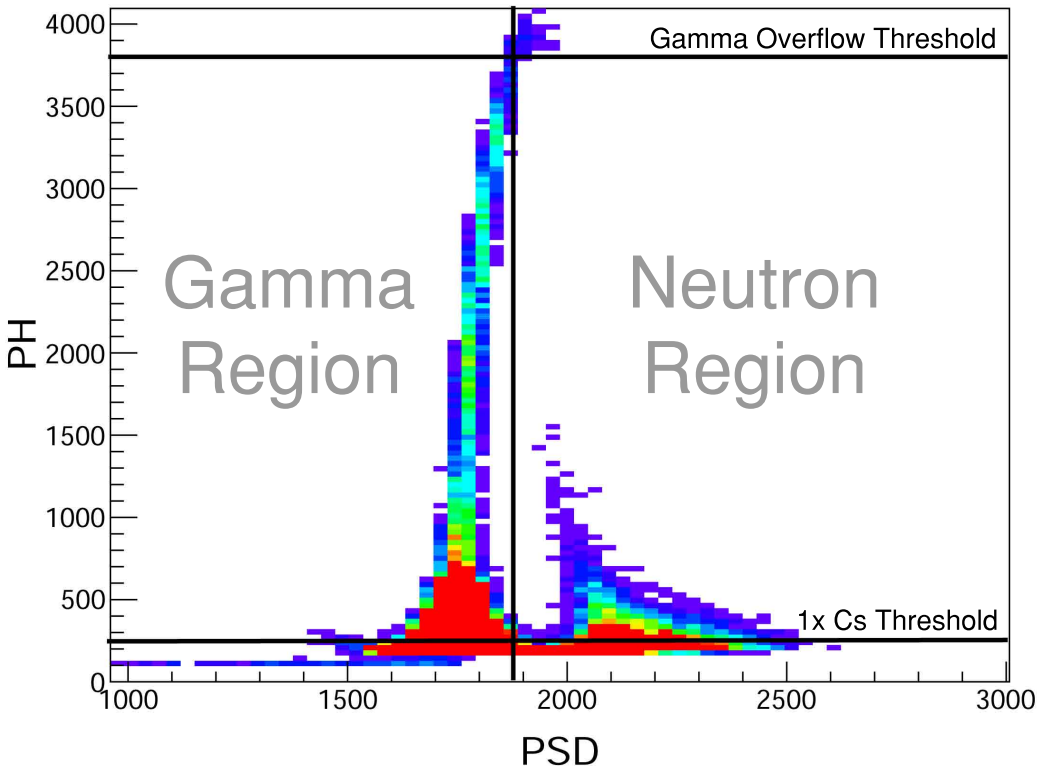

Figure 3.21: A sample PH vs PSD histogram showing the location of the 1x Cs, gamma overflow, and PSD cuts.

V. At this voltage the dark current was about 1.5 μA. Using a ^{241}Am HIS, the detector's energy resolution was measured to be 65 keV FWHM. The ΔE detector was an ORTEC model 025-50 and serial number 8-181C. It was biased to +10 V and had a dark current of about 0.06 μA at this bias voltage. Using a ^{241}Am HIS, the detector's energy resolution was measured to be 35 keV FWHM.

3.3.3: CsF Detector

A CsF scintillator detector (2.5 cm diameter, serial number MA 957) was positioned beneath the target chamber to observe gamma-rays produced by inelastic scattering off the target and beamstop to monitor the beam pulse timing. The detector was carefully shielded from other sources of beam-induced radiation such as activation of collimators or slits. The detector was biased to +1500 V. Further information on solid state and scintilator detectors

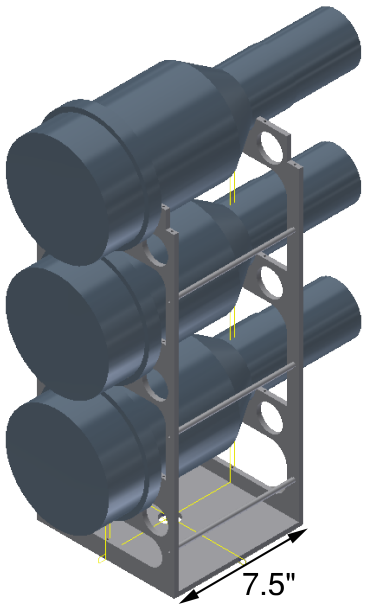

Figure 3.22: A CAD rendering of an array of three neutron detectors used for this experiment. The detector mount was designed and fabricated at TUNL. Hose clamps were modified to fit over the front and back of each detector to hold it securely in place. Each mount was made from aluminum and designed to attach to the standard 1-inch bolts on most TUNL beamposts. See online version for CAD file.

may be found in Knoll [2010].

Section 3.4: Electronics and DAQ

An overview of the electronic setup for this experiement is shown in Fig. 3.23. Circuit diagrams for the detector front-end electronics, the DAQ trigger, and the pickoff front-end electronics are shown in Figs. 3.24, 3.25, 3.26, and 3.27. The anode signals from the PMTs of the scintillator detectors were sent from Target Room 1 to the Control Room through RG-8 equivalent 50Ω low-loss cables. Signals from detectors and other diagnostic equipment around the target chamber were sent to the Control Room through the cables listed in Table 3.

For this experiment two sets of cables were run. One set, for the neutron detector anode signals, was 21 RG-213/U (low-loss 50Ω RG-8 equivalent) cables. These were run from the

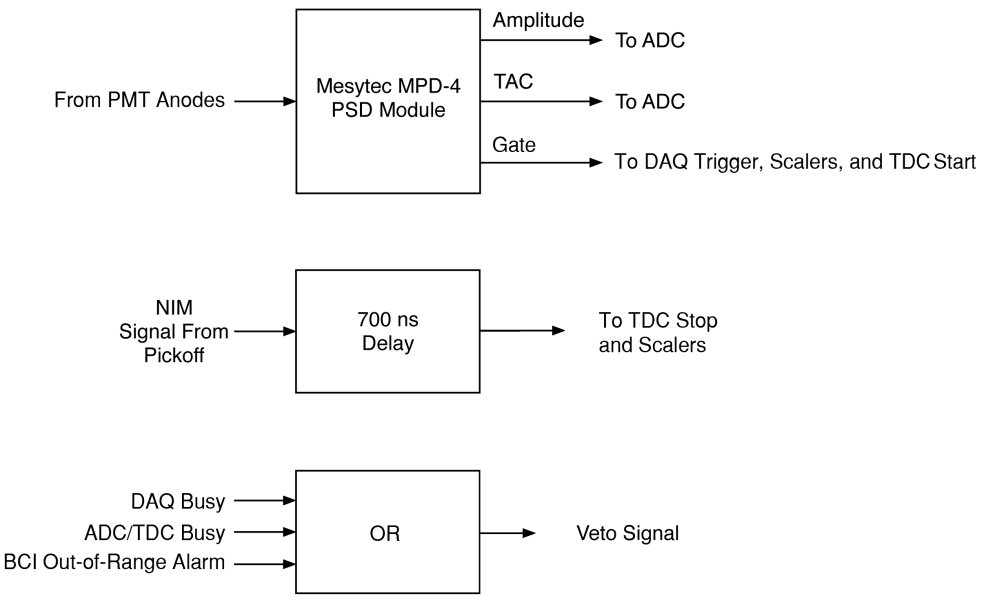

Figure 3.23: A grossly simplified schematic diagram of the DAQ electronics for this work. Detailed schematics are given for the neutron detector circuit in Fig. 3.24, the veto circuit in Fig. 3.25, the E-ΔE and CsF circuit in Fig. 3.26, and the pickoff circuit in Fig. 3.27.

neutron detector area in Target Room 1 to a patch panel in the Control Room in cabinet CP-R-17. The other set was a variety of cable types, run from a patch panel below the target chamber to a patch panel in the Control Room in cabinet CP-R-04. The cables run in this set are detailed in Table 8.3.

NIM bins and a VME crate held the DAQ electronics. The VME crate held a Motorola®) MVME 5100 single board computer, a Struck®) SIS 3610 input/output register, 2 CAEN®) V785 32-channel peak-sensing ADCs, a CAEN V775 32-channel TDC, and a Struck®) SIS3800 VME scaler/counter (select technical specifications are given in Table 3.4). The TDC was operated in common start mode with an 800 ns range. The anode signal from each detector PMT was processed with a Mesytec®) MPD-4 module to produce PH, PSD, and timing logic (gate) signals. PH and PSD signals were read directly by the ADCs. The gate signal was split; one signal was sent to a TDC stop and the other was ORed together with all other detectors to create the ADC gate and TDC common start (Fig. 3.24). This ORed signal was vetoed by (Fig. 3.25) the logic OR of the DAQ busy signal and a BOT

Table 3.3: VME electronics technical specifications

V785 ADC	12 bit resolution 10 mV - 4 V input range
V775 TDC	12 bit resolution NIM input 140 - 1200 ns full scale range
SIS3800 scaler	200 MHz count rate NIM/TTL input

not acceptable logic signal. The DAQ busy signal was the logic OR of the ADC, TDC, and DAQ trigger module busy signals. The BOT not acceptable signal was produced by a current comparator circuit. When the BOT went outside the acceptable range (set by the experimenter), the state of the output signal from the current comparator circuit was a logic true. Two other circuits processed the E-ΔE detector (Fig. 3.26) and the pickoff signals (Figs. 3.27 and 3.14).

The VME scaler module counted gate signals from each group of 3 neutron detectors and the CsF and E-ΔE detectors combined. It also counted BCI, pickoffs scaled down by a factor of 1000, total triggers and vetoed (i.e. live) triggers, and a 60 Hz clock and vetoed clock. The VME crate was read out by a PC running Scientific Linux v.6 using the CODA software from Jefferson Laboratories (Ahmed et al. [2003]). Data visualization and analysis was conducted using PAW (Johnstad [1989]) and ROOT (Brun and Rademakers [1997]).

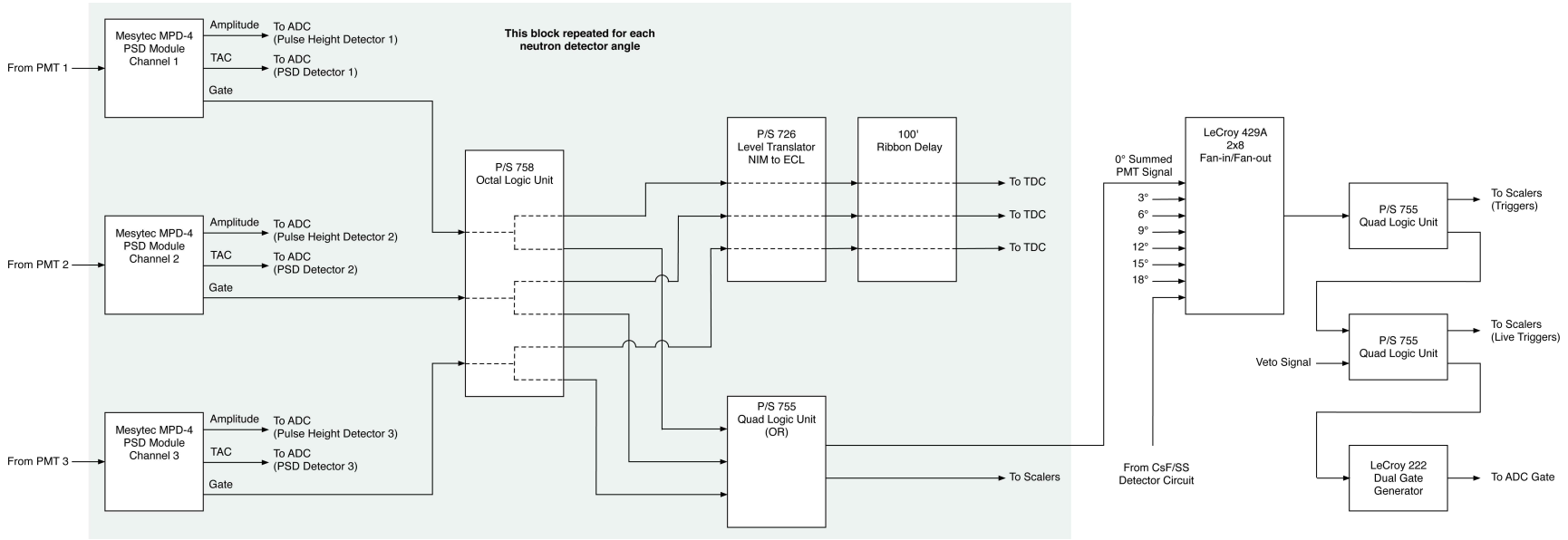

Figure 3.24: A flow diagram of the main circuit used to handle neutron detector signals. All Phillips Scientific® (P/S) 755 quad logic units were set to coincidence level 1.

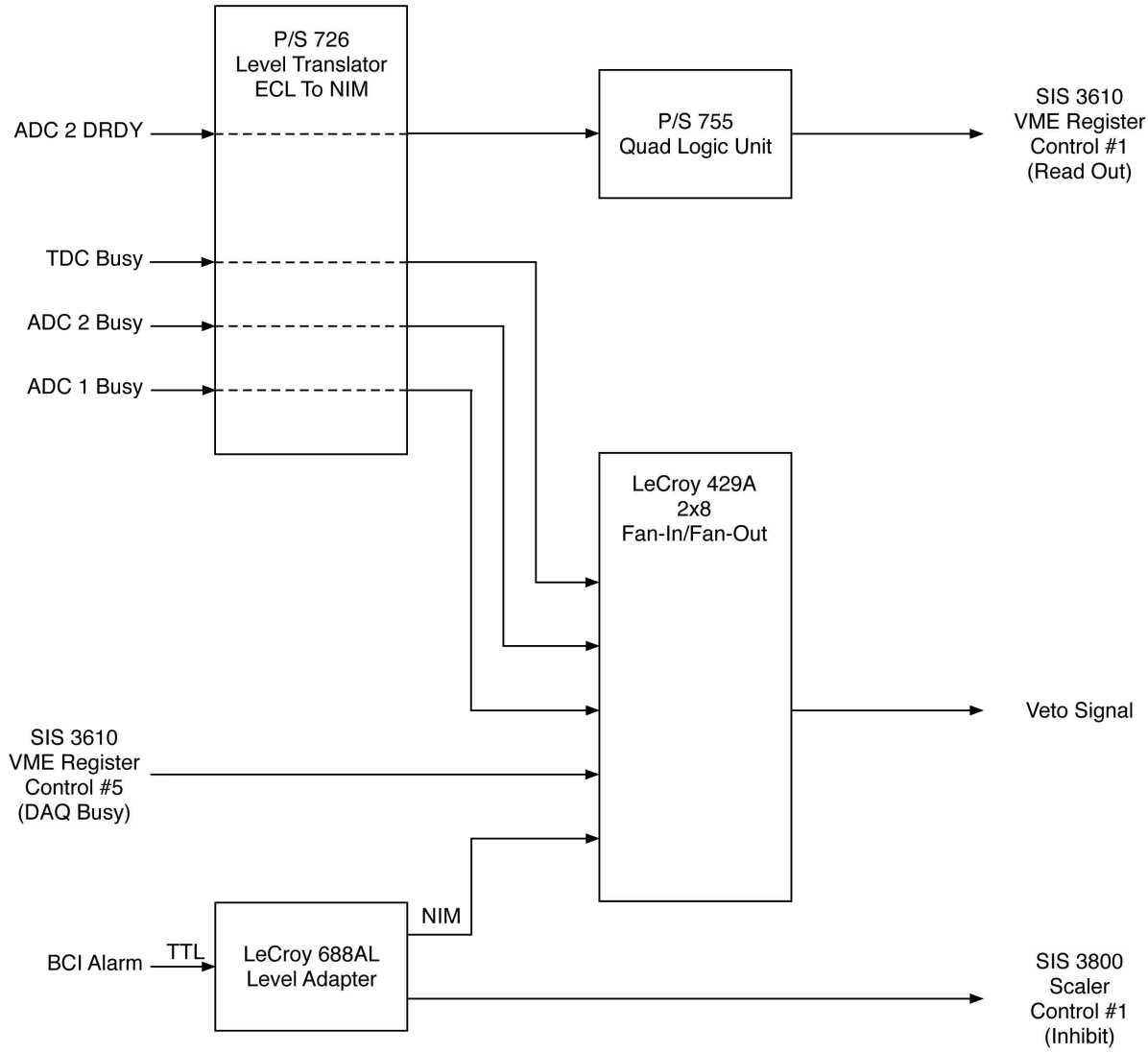

Figure 3.25: A flow diagram of the circuit used to produce the veto and read out signals. All P/S 755 quad logic units were set to coincidence level 1.

Some of neutrons from $(^3He, n)$ had energies beyond the range of the ADCs. However, by setting a bit within each ADC (c792overrange), counts from such neutrons were retained. These counts appeared in a single bin near the upper end of the ADC range.

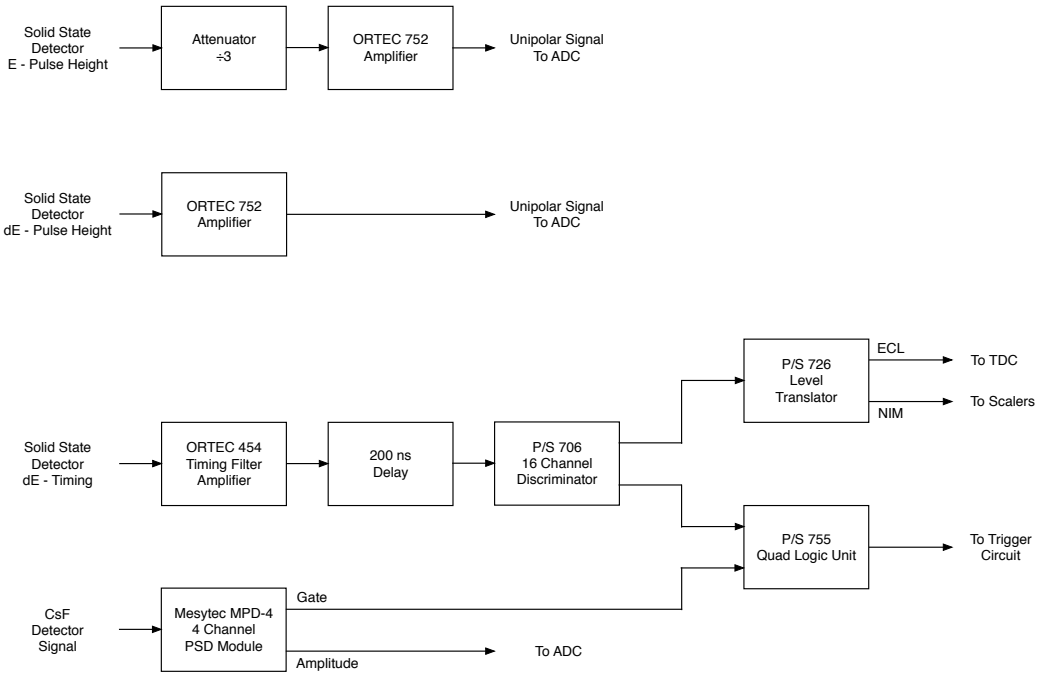

Figure 3.26: A flow diagram of the circuit used to handle signals from the E-ΔE telescope and the CsF detector. All P/S 755 quad logic units were set to coincidence level 1.

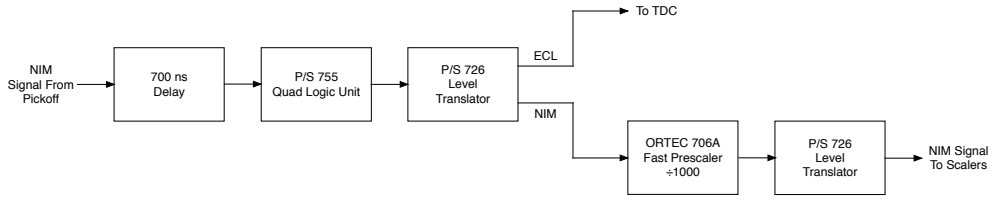

Figure 3.27: A flow diagram of the circuit used to handle signals from the beam pickoff. All P/S 755 quad logic units were set to coincidence level 1.

CHAPTER 4: Neutron Detector Efficiencies

In this experiment, the leading systematic uncertainty was in the efficiency of the 21 Bicron BC-501A (NE-213) liquid scintillator neutron detectors. Given $N_{incident}$ particles of energy E incident on a detector, the efficiency is defined as

$$\epsilon(E) \equiv \frac{N_{detected}}{N_{incident}} \tag{4.1}$$

where $N_{detected}$ is the number of particles producing a signal in the detector above some threshold. For scintillator detectors, the threshold is typically specified in terms of the energy deposited by an electron since scintillator light-output is a linear function of this energy (Dietze and Klein [1982b]).

This chapter discusses the method used to determine neutron efficiencies for the detectors. Nuclear reactions with well-established cross sections were used to measure the absolute efficiency at several neutron energies. These values were used to normalize Monte-Carlo efficiency calculations. The measured efficiencies were consistently lower than the Monte-Carlo calculations due to loss of scintillator fluid from the detector cells and oxygen contamination that has occurred over the lifetime of each. The normalized efficiencies from the Monte-Carlo calculation were then used to calculate cross sections for the Ge(^3He,n)Se reactions studied in this experiment. The uncertainty in these efficiencies contained contributions from relative efficiency measurements and dispersion between the calculated and measured absolute efficiencies. A single efficiency value at each neutron energy was assigned to all detectors for calculating the cross section from the two-proton transfer reactions.

Section 4.1: Simulations

The Monte-Carlo code NEFF7, developed by Physikalisch-Technische Bundesanstalt (PTB) in Braunschweig, Germany, is considered the gold-standard for calculating neutron detector efficiencies at a given threshold to within 1% (Dietze and Klein [1982a], Dietze and Klein [1982b], and Gonzlez-Trotter et al. [2009]). However, the maximum neutron energy for NEFF7 is 20 MeV, far below the relevant neutron energies in this experiment (22-32 MeV). The Monte-Carlo code KSUEFF, developed at Kent State University (KSU), was chosen since it can accept neutron energies from 0.1 to 300 MeV and can calculate neutron detection efficiencies to within a few percent (Cecil et al. [1979]). The calculations from the two programs were compared from 7 to 20 MeV with a PH threshold of 1x Cs applied. A ^{137}Cs source was also used to calibrate the PH spectrum of the detectors. The results are shown in fig. 4.1 and were found to agree with each other to within 5% percent.

KSUEFF uses tabulated cross sections and angular distributions of neutron-induced reactions on hydrogen and carbon (i.e., the elemental components of organic scintillators) to predict the direction and velocity of protons and heavier nuclei within the scintillator after interacting with an incident neutron of chosen energy. An experimentally determined light-output function is used to calculate the energy deposited by these secondary charged particles in terms of electron equivalent energy. Light-output is eqivalent to PH. After calculating the light-output from many incident neutrons of energy E_n, $\epsilon(E_n)$ is calculated using equation 4.1. Input parameters for KSUEFF are the scintillator geometry, scintillator composition, and the incident neutron energy (Cecil et al. [1979]).

Section 4.2: Measurements of Absolute Efficiency

The absolute efficiency of the neutron detectors was determined by measuring the neutron yield from a reaction with a well-established cross section that produces nearly mono-energetic neutrons. Efficiencies were measured in the 22-32 MeV energy range using the

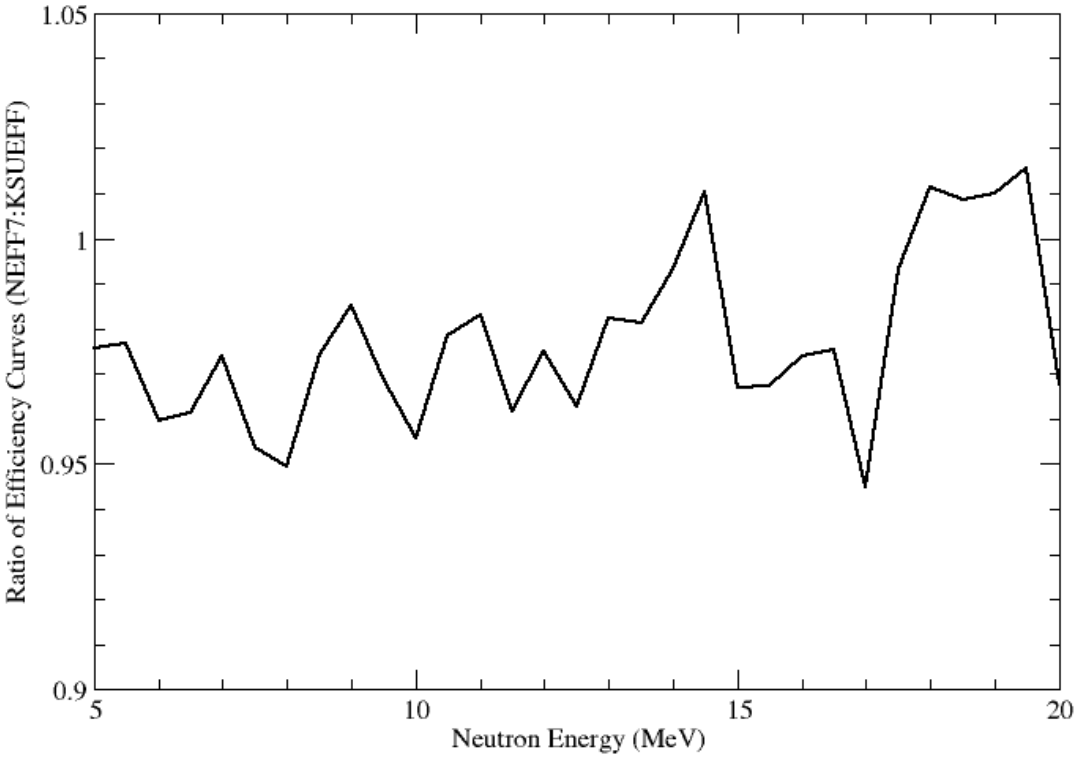

Figure 4.1: A plot of the ratio of the calculated efficiencies from the PTB code NEFF7 to the KSU code KSUEFF from 5 MeV to 20 MeV neutron energy.

^{3}H(d,n)^{4}He reaction, which has a Q-value of 17.6 MeV (Drosg and Schwerer [1987]). Because of a large uncertainty in the thickness of the ^{3}H target, efficiencies were also measured between 8 MeV and 16 MeV using the ^{2}H(d,n)^{3}He reaction, which has a Q-value of 3.3 MeV (Drosg and Schwerer [1987]).

A 50 keV deuteron beam was generated by the direct-extraction negative ion source (DENIS) in the TUNL tandem accelerator laboratory. A deuterium gas cell target was used for the ^{2}H(d,n) reaction and a tritiated foil target was used for the ^{3}H(d,n) reaction. Both targets were placed at the end of the 38-degree beamline in the neutron time of flight room at 0° relative to the beam axis. The beam was pulsed using a sine-wave chopper, a square-wave chopper, and a double-gap buncher as described in chapter 3. Beam was delivered to target with an average current of 25 nA and a time resolution of $<$ 2 ns FWHM. Six of the detectors were surveyed. These detectors were assumed to be representative of the full 21-detector array. This assumption was justified by the fact that all 21 detectors were identically constructed.

Absolute efficiencies were determined using the standard equation for experimental differential cross section, $\frac{d\sigma}{d\Omega}$,

$$\frac{d\sigma}{d\Omega}(\theta, E_n) = \frac{Y_n(\theta, E_n)}{N_{incident} \times n_{target} \times \epsilon(E_n) \times \Delta\Omega}. \tag{4.2}$$

This equation was solved for detector efficiency, ϵ,

$$\epsilon(E_n) = \frac{Y_n(E_n)}{N_{incident} \times n_{target} \times \Delta\Omega \times \frac{d\sigma}{d\Omega}(E_n)} \tag{4.3}$$

where Y_n is the neutron yields at an angle θ relative to the beam axis and a neutron energy E_n, $N_{incident}$ is the number of ^{2}H nuclei incident on the target, n_{target} is the target thickness in units of mass per area, and $\Delta\Omega$ is the detector solid angle coverage. Cross section values were taken from tables by (Drosg and Schwerer [1987]). The number of target atoms per unit area, n_{target}, was determined in two different ways depending on which target was being

used and will be discussed in the following sections. $N_{incident}$ is computed by

$$N_{incident} = BCI \times LT \times PO \times \frac{e}{charge\ state} \tag{4.4}$$

where BCI is the total charge incident on the target, LT is fraction of total run time that the DAQ was live, PO is the fraction of expected beam pickoffs that were recorded by the capacitive pickoff unit, e is the electron charge, and *charge state* is the net charge of a single beam particle in units of electron charge. BCI was measured by a beam current integrator, which produced logic pulses corresponding to 10^{-10} C/pulse. These pulses were recorded by the VME scalers. LT was typically 0.4-0.9 and PO was typically 0.9-1.0 during the absolute efficiency measurements. For the singly-ionized ^{2}H beam used, *charge state* = 1.

$\Delta\Omega$ was approximated by

$$\Delta\Omega = N_{det} \times \frac{\pi r^2}{l^2} \tag{4.5}$$

where N_{det} is the number of identical detectors at some θ, r is the radius of the detector active volume, and l is the distance from target to center of the detector active volume. This approximation is valid provided $l \gg r$. For the absolute efficiency measurements, $N_{det} = 1$, $r = 6.35$ cm, and $l = 500$ cm.

4.2.1: ^{2}H(d,n)^{3}He

The deuterium target was a stainless steel cylinder filled with deuterium gas. It measured 2.85 cm long and has a 6.35 μm thick Havar® window to allow beam particles to pass with minimal energy loss while containing the pressurized deuterium gas. At room temperature and 2 atm pressure, n_{target} may be calculated using the ideal gas equation $n_{target} = \frac{Pl}{RT}$. In this equation P is the pressure, l is the length of the target, R is the gas constant and T is the temperature. The target density was calculated to be 3.20×10^{20} d/cm^2. The efficiency was measured with this reaction for neutron energies of 8, 10, 12, 14, 15, and 16 MeV. Detectors

were placed 5 m from the end of the deuterium cell. During the measurement, the pressure was monitored for any changes which would indicate heating of the target gas due to the beam and cause a differential in pressure local to the beam, changing the effective target thickness.

Figure 4.2 shows the neutron TOF spectrum from this reaction at a few different incident deuteron energies. In all of the spectra the mono-energetic peak from the ^{2}H(d,n) reaction is clearly visible on the right side. Y_n was determined by simply integrating this peak. Above a neutron energy of 10 MeV a prominent mound caused by neutrons from the deutron-deuteron breakup reaction is visible on the left side (i.e., lower energy). Although the peak of interest is well separated from the breakup neutrons, the data rate from the detectors became too high at higher energies. At a neutron energy of 16 MeV the DAQ live time was below 40%. Additionally, at the time of this experiment, technical issues with the tandem chain charging system prevented operation with a tandem terminal voltage above 7.5 MV. In principle, this reaction could have produced neutrons up to an energy of 19 MeV at the maximum terminal voltage of approximately 9 MV.

4.2.2: ^{3}H(d,n)^{4}He

Figure 4.3 shows the neutron TOF spectrum from this reaction at a 20 MeV incident deuteron energy. The tritium target was a solid target constructed on a 0.4 mm thick disk with diameter of 19 mm of oxygen-free high-conductivity (OFHC) copper. A 2 mg/cm^2 layer of titanium was evaporated on to the copper disk and then implanted with tritium. The limiting factor in using the tritium target for absolute efficiency measurements was the uncertainty in n_{target}. The data sheet from the target manufacturer gives a thickness of 3.91×10^{19} t/cm^2 after the tritium implantation in June, 2012. Adjusting for loss due to the decay of tritium from the time of implantation until the time of this measurement (July, 2015) reduced that number by a factor of 0.839. Measurements were taken with a flight path of 5 m for neutrons of energies 20, 24, 26, and 30 MeV.

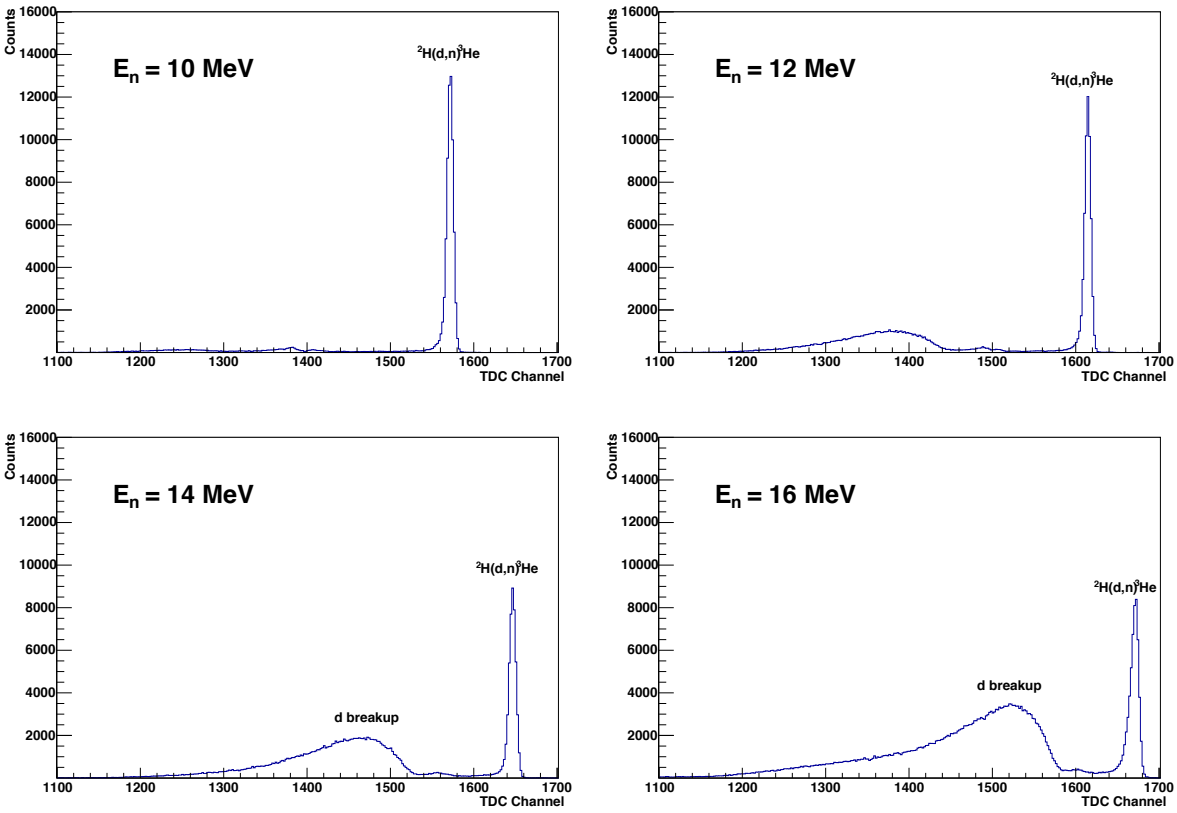

Figure 4.2: Neutron time of flight spectra from the the ^{2}H(d,n) reaction at neutron energies of 10, 12, 14, and 16 MeV. TOF increases to the left.

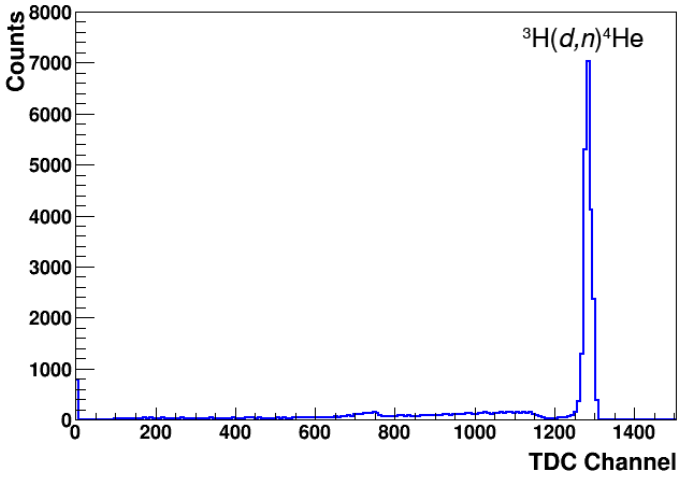

Figure 4.3: Neutron time of flight spectra from the the ^{3}H(d,n) reaction at a neutron energy of 20.0 MeV. TOF increases to the left.

Section 4.3: Comparison to Simulation

Figure 4.4 shows the measured efficiencies from the ^{2}H(d,n) and ^{3}H(d,n) reactions for neutron energies ranging from 8 MeV to 30 MeV. The plot also includes the neutron detection efficiency calculated by KSUEFF. The calculated efficiency curve was scaled down to the best match the ^{2}H(d,n) data using a least-squares fit. This was justified by the negligible ($< 1\%$) error on all terms in equation 4.3 and scintillator loss from the detector cells over the detectors' lifetimes. The standard deviation of the ^{2}H(d,n) data points about the scaled KSUEFF curve was 2.5%. This value was interpreted as the uncertainty in measured detector efficiency.

After scaling the KSUEFF curve, the ^{3}H(d,n) data was scaled up by 7.7% to best match that curve using a least-squares fit. This was justified by beam-induced tritium loss over the target's lifetime. The standard deviation of the scaled ^{3}H(d,n) data points about the scaled KSUEFF curve was 4.3%. This value was interpreted as the uncertainty in the shape of the KSUEFF curve.

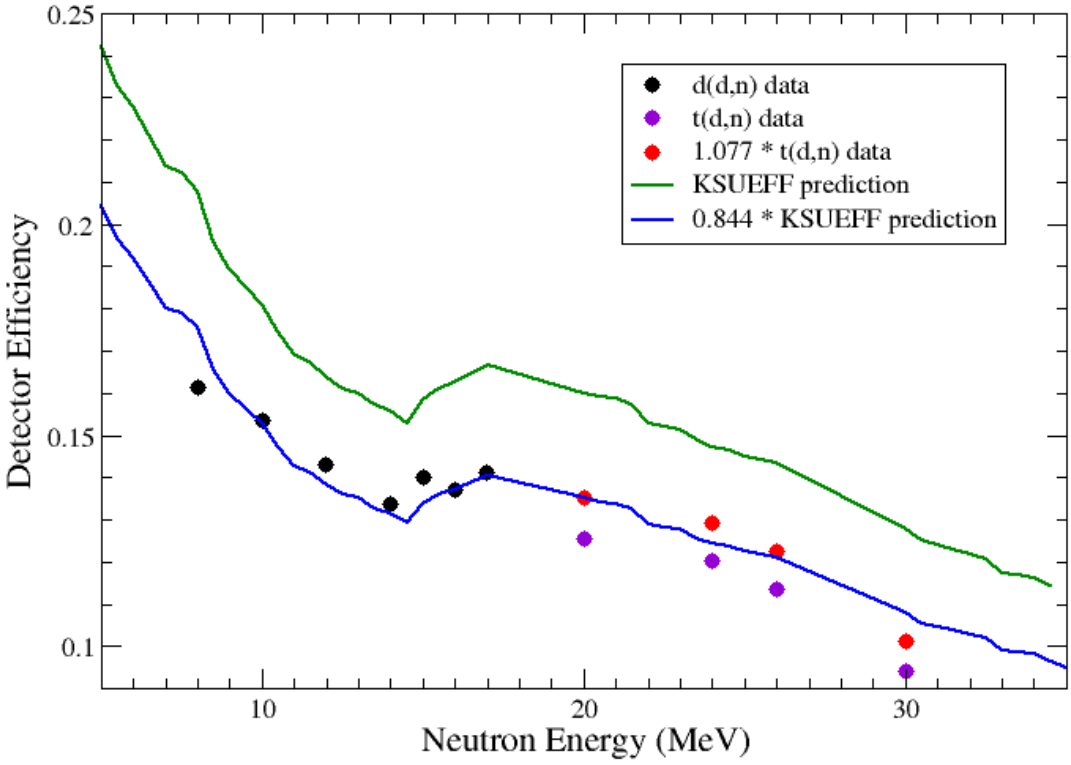

Figure 4.4: The detector efficiency at 1x Cs threshold as a function of neutron energy. Data from ^{2}H(d,n)^{3}He and ^{3}H(d,n)^{4}He are compared with the KSUEFF predictions. Statistical errors are smaller than data points. See text for details.

Section 4.4: Relative Efficiency

Absolute efficiencies were measured in 6 of the 21 detectors and a relative efficiency measurement was used to check the remaining detectors. The measurement was done using a 19.7 mCi ^{241}Am-Be neutron source placed 150 ± 0.5 cm from the front face of each detector. The PMT anode signal from each detector was processed by an Mesytec MPD-4 module. Counts were accumulated for 15 minutes per detector. PSD techniques were used to exclude gammas. Integrated counts in the PH spectrum above a 1x Cs threshold were determined for each detector. Each of these values was then divided by the average of the integrated counts from the 6 detectors used for absolute efficiency measurements. The mean efficiency for all of the detectors was found to be 0.99 relative to the 6 reference detectors with a standard deviation of 5.5%. This value was also interpreted as the uncertainty in measured detector efficiency. The results are shown in fig. 4.5.

Section 4.5: Efficiency Uncertainty

Measurements of the absolute and relative efficiencies accumulated enough counts to make statistical errors negligible ($< 1\%$). The sources of statistical error in $\epsilon(E_n)$ are listed in table 4.5. The total systematic error was determined by suming the uncertainties in the measured detector efficiencies and the shape of the KSUEFF curve in quadrature. The value of 5.5% was chosen for the uncertainty in the measurements, corresponding to the larger uncertainty between the absolute and relative measurements.

Table 4.1: Systematic Errors in $\epsilon(E_n)$

Source of Error	Size
absolute efficiency measurements	$\pm 2.5\%$
relative efficiency measurements	$\pm 5.5\%$
KSUEFF curve shape	$\pm 4.3\%$
total	$\pm 7.0\%$

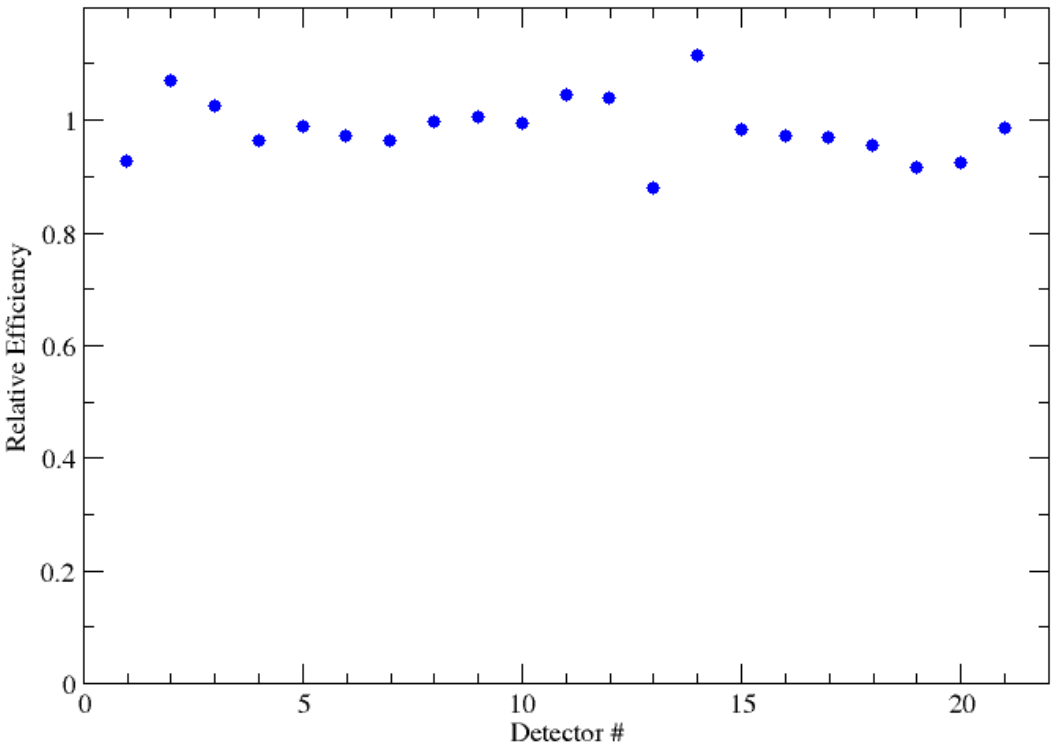

Figure 4.5: The relative efficiencies of all 21 neutron detectors. Statistical errors are smaller than data points.

CHAPTER 5: Target Fabrication and Characterization

Germanium and tellurium targets were fabricated using the TUNL evaporator system. The targets were evaporated onto gold foil backings that were mounted on tantalum rings (see Fig. 5.1). Target thickness was measured using a quartz crystal monitor during evaporation and more precisely by measuring the energy loss in alpha-particles passing through the foil targets.

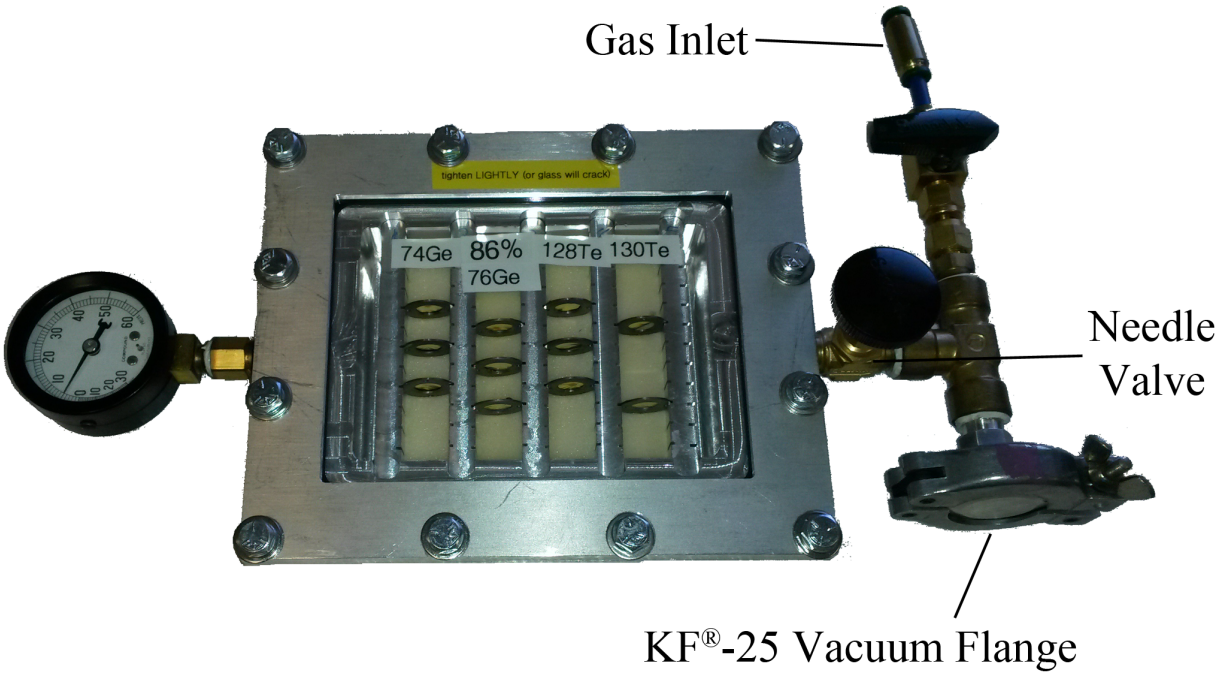

Figure 5.1: A photograph of the targets fabricated for this work. The targets are stored under argon gas to prevent oxidation. The target box was also designed and fabricated at TUNL.

Section 5.1: Target Ring and Substrate Preparation

The target rings were fabricated from tantalum sheet in the Duke instrumentation shop. A drawing of a target ring is shown in Fig 5.2. The dimensions of the rings were one of several standard ring designs used at TUNL.

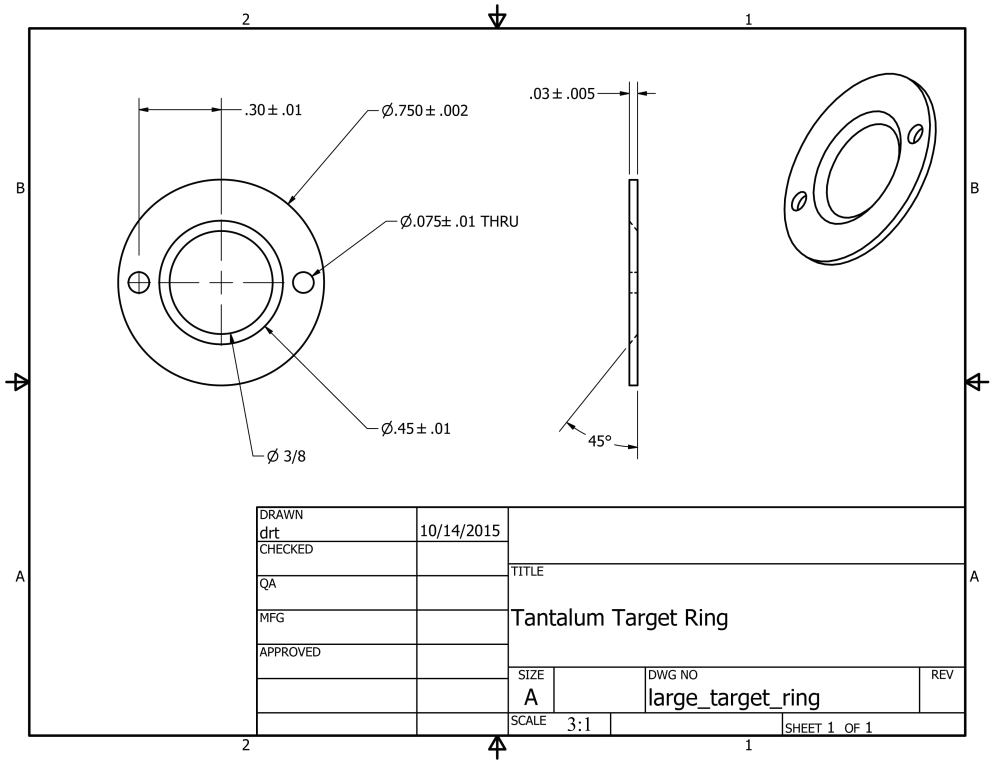

Figure 5.2: A technical schematic of a target ring, dimensions are in inches. See online version for CAD file.

The choice of tantalum was the result of optimization considering three factors: (1) the atomic number (Z) of the primary element in the material, (2) tensile strength, and (3) cost of material. A high Z material is desired to reduce the production of background neutrons from (^3He,n) by the beam halo due to collimator scattering. The rings must be made of a material with sufficient tensile strength for the rings to be thin but without substantial mechanical flexing when being mounted to the target rod. This feature is important for minimizing wrinkles in the mounted targets.

Gold backing foil with a thickness of 2 mg/cm^2 was purchased from Goodfellow in the

Table 5.1: Isotopes and Enrichment

Isotope	Isotopic Purity
^{74}Ge	98.90%
^{76}Ge	87.31% (12.69% ^{74}Ge)
^{128}Te	99.19%
^{130}Te	99.48%

form of 25 mm x 25 mm square sheets. Each sheet was cut using a razor blade into four equal sized pieces. Each piece was attached to a target ring with a small drop of 5-minute epoxy on each corner.

Section 5.2: Evaporator Operation

Isotopically enriched germanium and tellurium were purchased from the National Isotope Development Center at Oak Ridge National Laboratory in chemically pure (metallic) powdered form. A list of these isotopes and the enrichment purity are given in table 5.1.

These isotopes were deposited on the gold backing foils using the high-vacuum evaporator system at TUNL.

Target rings were placed upside down above a metal boat evaporation source in which about 500 mg of germanium or tellurium was placed. A high current was passed through the boat, resistively heating it and its contents, which evaporated onto the target backings. A movable shutter was placed between the target rings and the boat. The shutter was a thin steel disk, approximately 10 cm in diameter, that was positioned either between the boat and targets or off to the side of the bell jar. The latter position allowed a direct line of sight between the boat and the targets. The shutter allowed immediate stopping or starting of evaporation onto the targets at two times during the fabrication: (1) during the initial heating, material outgassing from the boat was prevented from depositing on the targets and (2) once the desired thickness was reached, evaporation was immediately halted. A heat shield (consisting of a sheet of metal with a several centimeter diameter hole in the center)

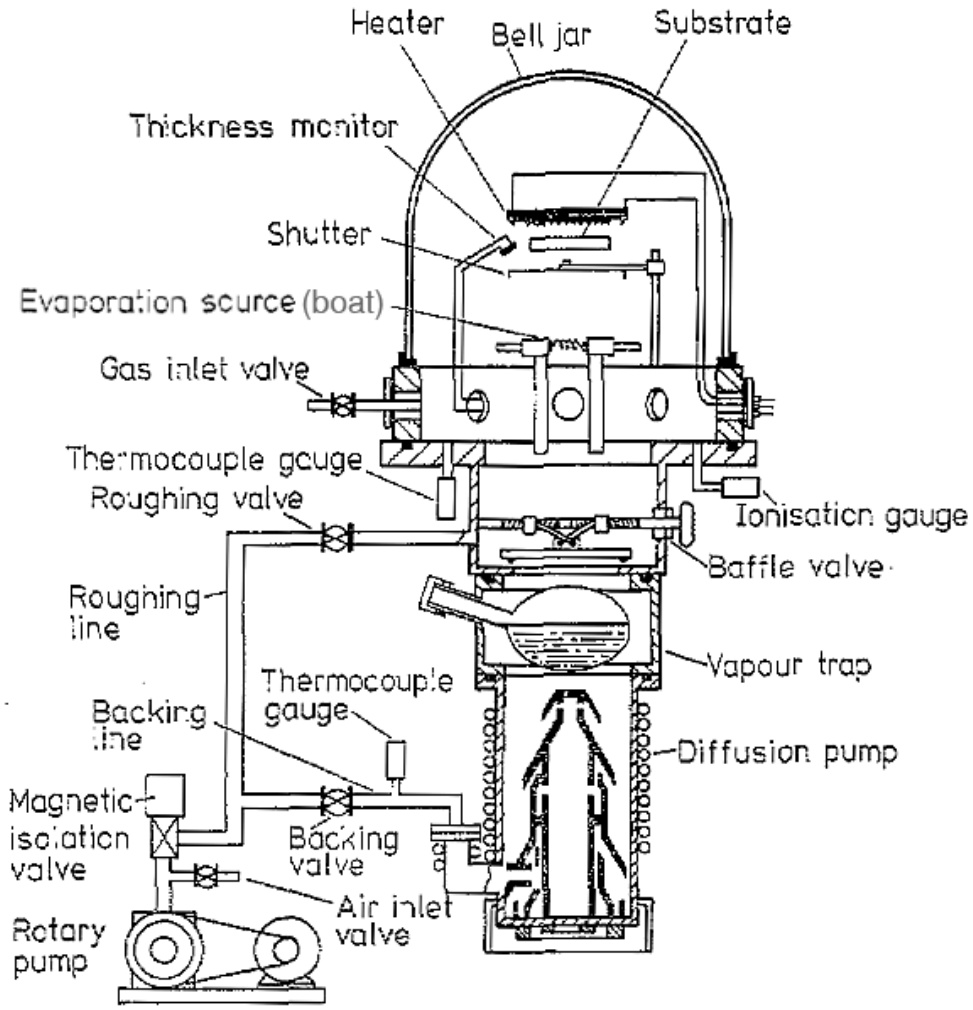

Figure 5.3: A schematic diagram of the high-vacuum evaporator at TUNL. This figure was taken from Muggleton [1979].

was placed just above the boat to reduce the radiant heating of components above the boat. In particular, the thickness monitor and epoxy on the target rings were temperature sensitive. This whole apparatus was surrounded by a glass bell jar to maintain a high-vacuum of at least 10^{-4} Torr during evaporation.

Several types of boats were considered for use in the fabrication of the targets for this research. All boats were made of tungsten, as recommended by R.D. Mathis (the boat manufacturer), to minimize chemical reactivity with their contents. The design of the boats can be characterized as being in two categories, open or closed. A short description of each

category is given here.

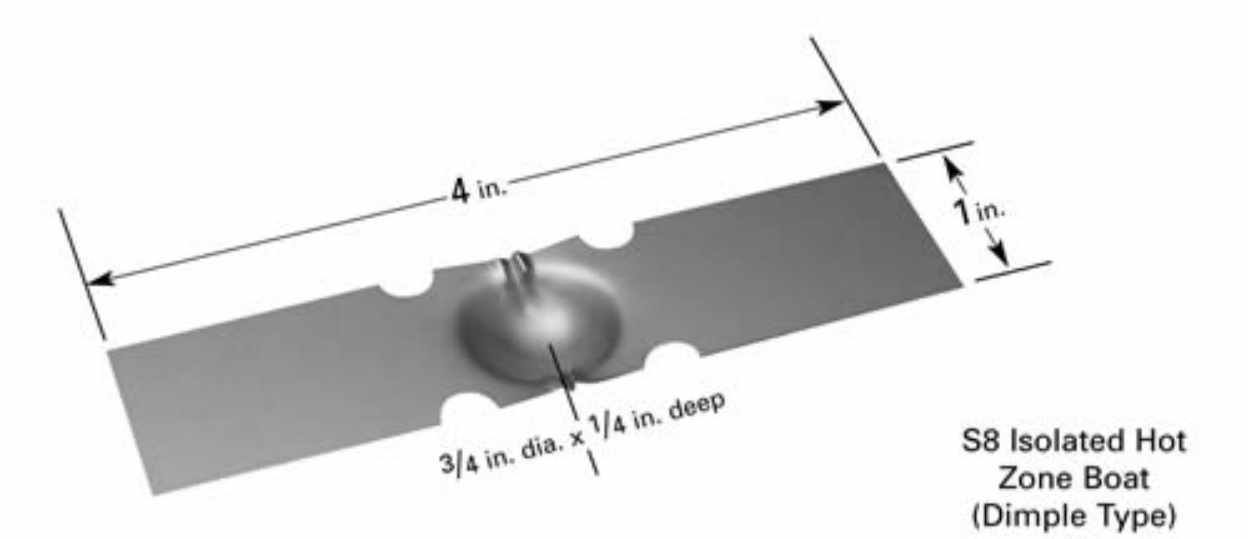

Figure 5.4: A photograph of an open boat used to hold and heat material for evaporation. This image was taken from www.rdmathis.com.

Open boats enable convenient loading of materials that are in a wide variety of physical forms, e.g., liquid, solid chunks, or powder. Also, recovery of materials and boat clean up after use are straightforward (see Fig. 5.4). However, open boats were found to be problematic for this application, as the powdered germanium and tellurium would vibrate out of the boat when heated; this was a particular problem considering these isotopically enriched materials cost several thousand dollars per gram. The closed boat design shown in Fig. 5.5 was selected to minimize the loss of materials during the evaporation process.

A water-cooled quartz crystal thickness monitor (model TM-100R by Maxtek) was placed in the evaporator at about the same distance from the boat as the target rings. The thickness monitor works on the same principle as a driven damped mechanical oscillator. That is, the resonant frequency of the oscillator depends on the mass of the system. The crystals resonant frequency, f_0 changes in proportion to the mass deposited on its face, dm.

Figure 5.5: A photograph of a closed boat used to hold and heat material for evaporation. This image was taken from www.rdmathis.com.

$$df_o = -\frac{f_0^2}{NP_q} \times \frac{dm}{F} \tag{5.1}$$

where P_q is the density of quartz, F is the area of the crystal face, and N is a frequency constant equal to 1670 kHz/mm. It is assumed that $f_o \gg \Delta f_o$ and $m \gg \Delta m$ (Muggleton [1979]).

The evaporator was operated as follows. After placing the target rings with gold foils, the filled boat, the shutter, the heat shield, and the thickness monitor inside the bell jar, the system was allowed to pump down overnight. After sufficient vacuum was achieved, the target material was outgassed by gradually raising the temperature of the boat. The current in the boat was slowly increased, in steps of 10 to 20 amps every few minutes while watching the pressure inside the bell jar. A pressure increase inside the bell jar as the boat heated was an indication of outgassing of the target material. Outgassing as the boat heated was observed by increasing pressure. The current was held constant until outgassing stopped and the pressure recovered. The current was then increased until the material in the boat melted,

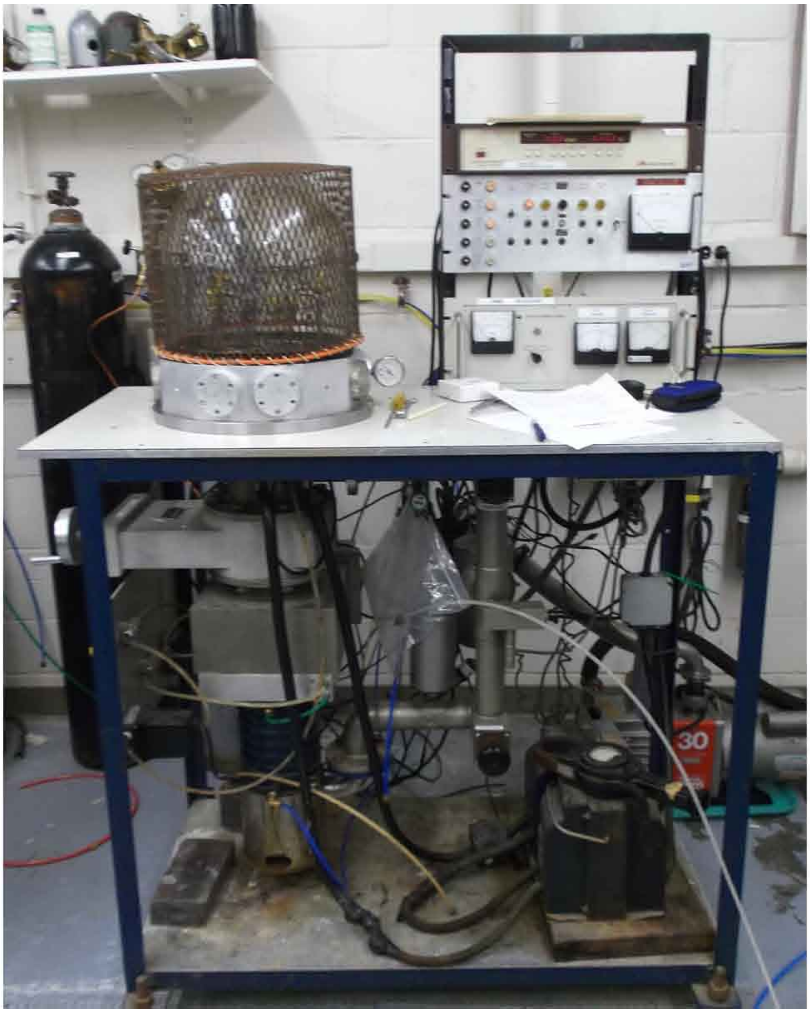

Figure 5.6: A photograph of the high-vacuum evaporator at TUNL. (Photograph by Chris Westerfeldt.)

which was visually confirmed. Tellurium melted around 210 amps, while germanium, with a higher melting temperature, melted around 290 amps (of course, the amount of current required also depended on the type of boat used). After melting, the shutter was opened and the thickness monitor turned on. The current was further adjusted to produce a reasonable rate of deposition on the thickness monitor (between one and five angstroms per second). At this evaporation rate, the desired thickness of 2 mg/cm2 was attained within several hours. After reaching this thickness the shutter was reinserted, the boat heating current was turned off, and the evaporator was allowed to sit overnight to cool.

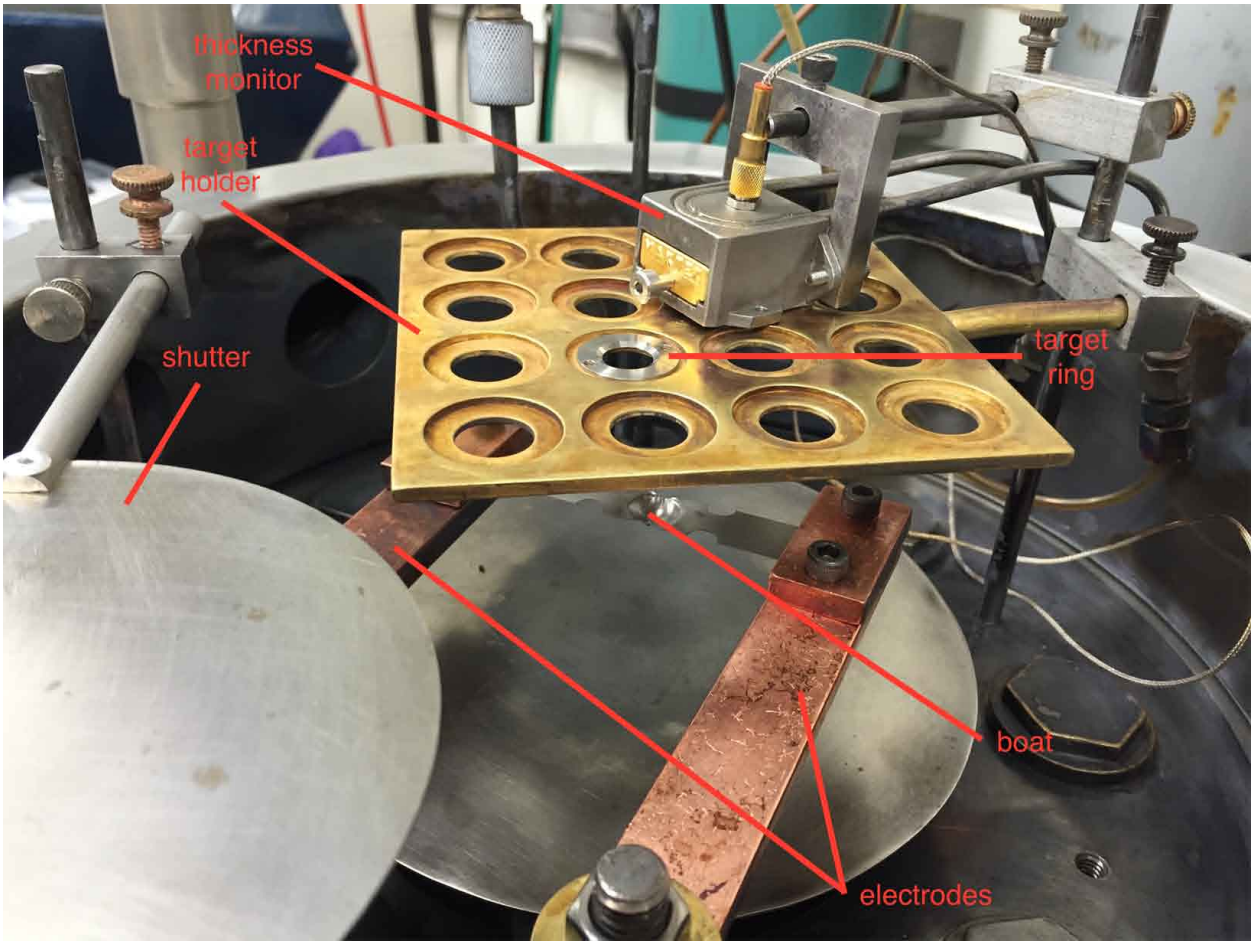

Figure 5.7: A photograph of the target fabrication setup of the high-vacuum evaporator at TUNL. The Evaporation area is enclosed by a glass bell jar during operation. (Photograph by Dustin Combs.)

The targets were then removed and placed into a target box pressurized with argon. More detailed information on evaporator operation may be found in Zawisza [2012].

Section 5.3: Target Thickness Measurements

The thickness of each fabricated target was then measured by the energy loss in alpha-particles passing through the target. The energy deposition measurements were performed in a vacuum chamber using a silicon barrier detector to measure the energy of the alpha-particles from an americium-241 source. The location of the alpha-particle peak in the energy

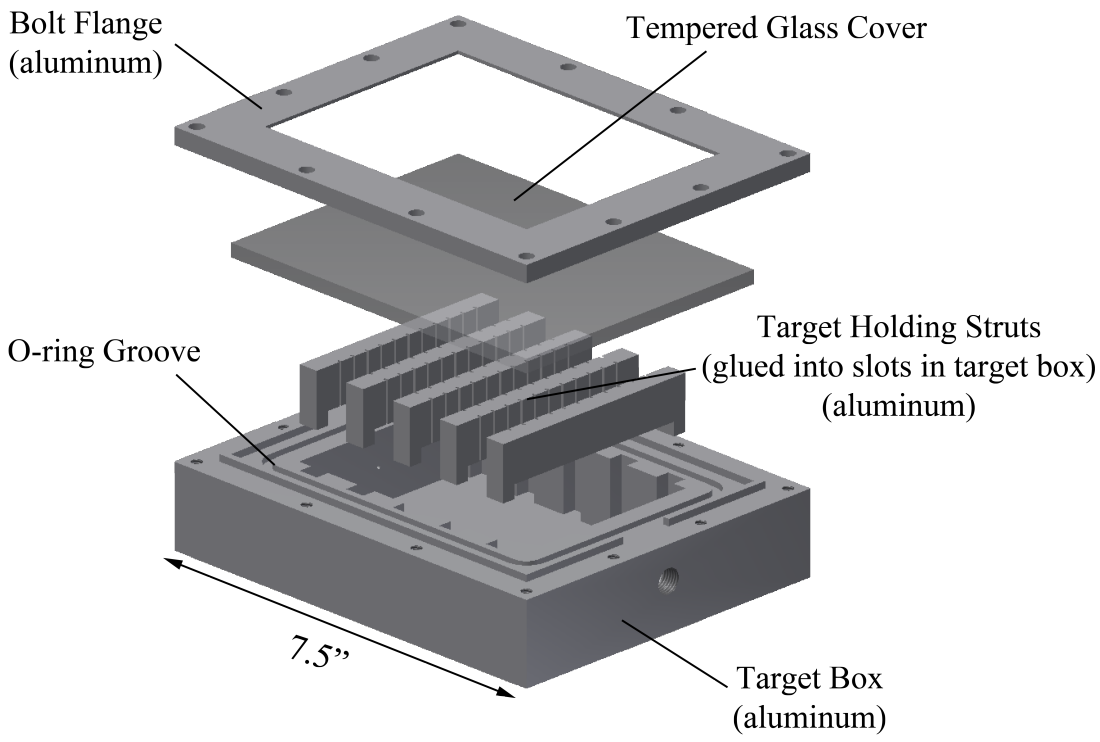

Figure 5.8: A CAD rendereding of the storage target box, which was designed and fabricated at TUNL. It has been observed to maintain 5±0.25 psig argon for at least two months. See online version for CAD file.

spectrum measured using the solid-state detector with the target between the source and detector was compared to the location of the peak without a target. The peak shift was due to the energy loss in the target foil, and the program LISE (a code developed by the National Superconducting Cyclotron Laboratory) was used to calculate the target thickness corresponding to that energy loss. The thickness of each gold foil backing was measured using the same method before evaporative coating with germanium or tellurium.

The energy loss is the foil is given by

$$E_{loss} = k(x_1 - x_2) \tag{5.2}$$

where k is a constant relating MCA channel number to energy.

The uncertainty in target thickness results from the accuracy of determining the alpha-particle peak location (+-2 channels), the ADC pedestal location (+-1 channel), and the

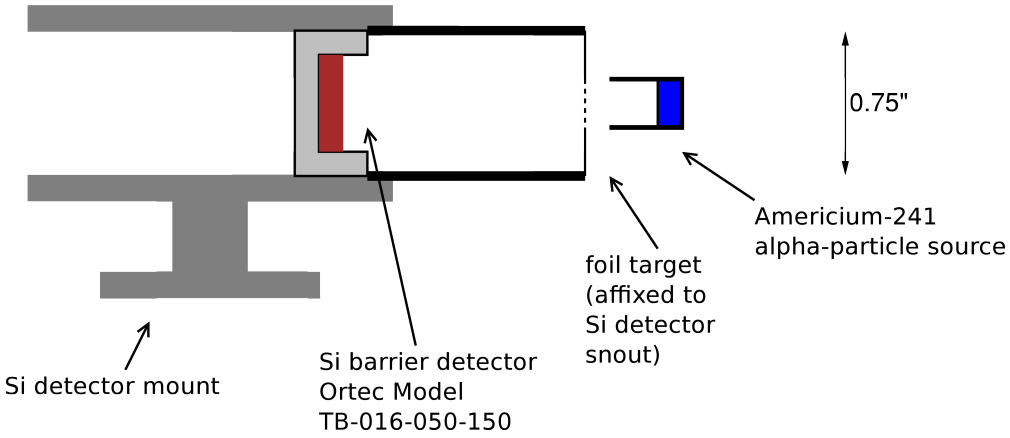

Figure 5.9: Cross-sectional diagram of the setup for the foil thickness measurements carried out using an americium-241 alpha-particle source. The Si detector was biased to +75 V through a 12 MΩ preamplifier. The PH signal was amplified with an Ortec model 572 amplifier. A PH histogram was produced using an AMETEK MCA.

calculated variation over the surface of each target (∼10%). The uncertainty due to the variation over the target surface dominates the total thickness uncertainty. This uncertainty is due to the differing distance between points on each target and the boat during evaporation (i.e., the outer edge of each target was further from the boat than the inner edge; therefore the outer edge was less thick). If the boat is considered to be a point particle source[1] radiating isotropically into 2π steradians, the mass, m, of material required in the boat to acheive a thickness n_o (mass/area) at the center of a target is given by

$$m = 2\pi n_o(r_o^2 + h^2), \tag{5.3}$$

where r_o/h are the horizontal/vertical components of the distance between the particle source and the center of the target. The thickness at some other point on the target is given by

$$n(r) = n_o \times \frac{r_o^2 + h^2}{r^2 + h^2}, \tag{5.4}$$

where r is the horizontal component of the distance between the particle source some point

[1]In actuality, since the opening in the boat has a finite size, assuming a point source overestimates the thickness variation.

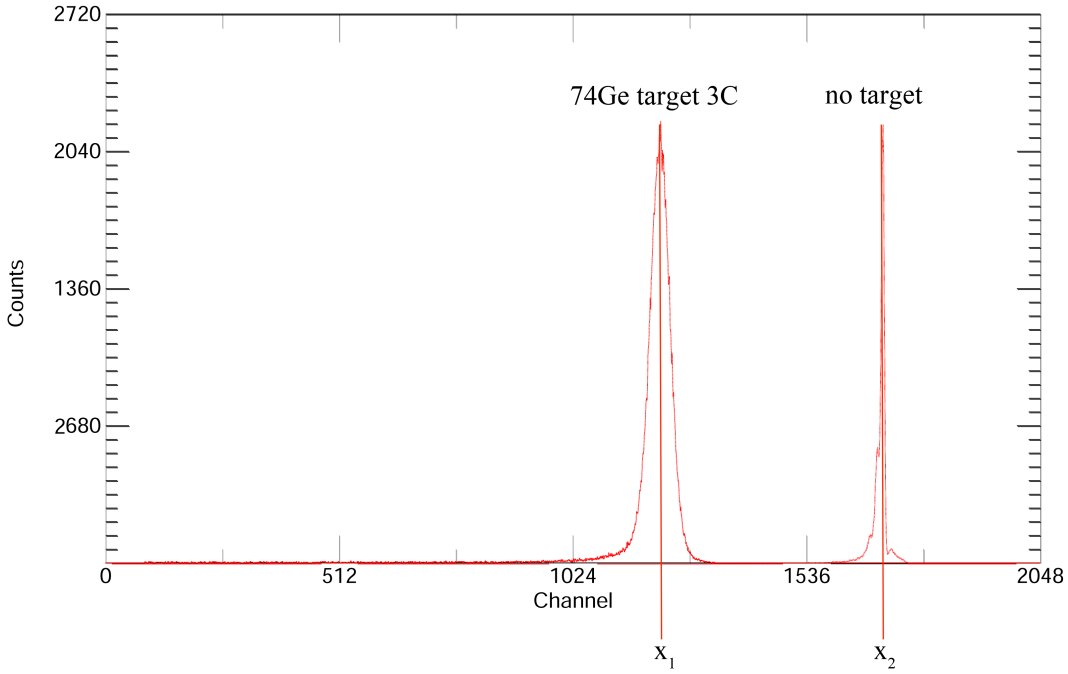

Figure 5.10: PH spectrum of alpha-particles from an americium-241 source measured: (a) without a target, and (b) with a target foil positioned between the source and detector.

on the target. The maximum fractional variation across a target's surface is therefore,

$$\Delta n = \frac{n(r_{min}) - n(r_{max})}{n(r_{max})}, \tag{5.5}$$

where $r_{max} - r_{min} = 1$ cm, the width of the hole in each target ring. Equations 5.3 and 5.5 are plotted in Fig. 5.11 for the targets fabricated for this work. For $h \sim 5.8$ cm, $\Delta n \sim 10\%$. However, because of the small beam size (< 2 mm), the total uncertainty in target thickness was estimated to be less than 5%.

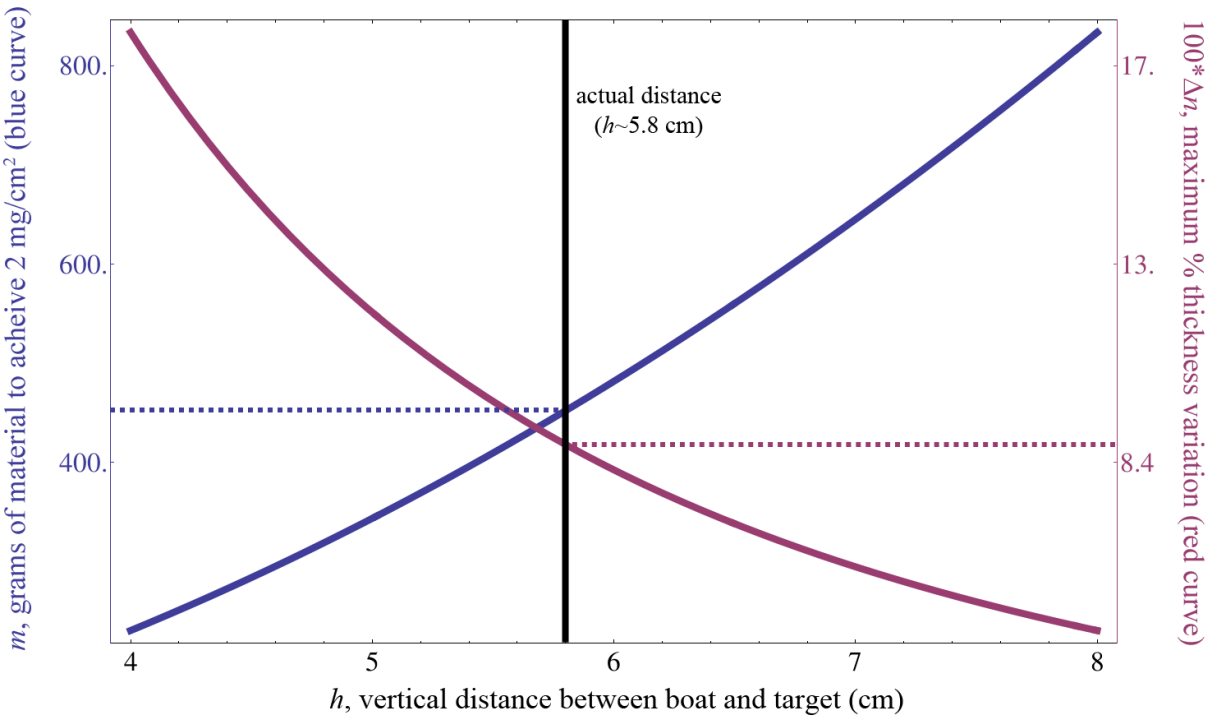

Figure 5.11: A plot of the calculated amount of material needed to acheive 2 mg/cm^2 target thickness and the calculated target uniformity vs. the vertical distance between the boat and the centers of the targets. The vertical line is located at the actual distance used to fabricate the targets.

Table 5.2: List of Targets Fabricated

Material	Date Fabricated	Monitor Thickness (mg/cm^2)	Measured Thickness (mg/cm^2)	Measured Thickness ($nuclei/cm^2$)	Substrate	Measured Substrate Thickness (mg/cm^2)	Identifier
^{74}Ge	2/28/2016	2.015	N/A	N/A	Au	not measured	1C
^{74}Ge	2/28/2016	2.015	N/A	N/A	Au	not measured	2C
^{74}Ge	2/28/2016	2.015	2.31	1.88E+19	Au	2.52	3C
^{76}Ge (86%)	3/25/2016	2.008	2.36	1.87E+19	Au	2.54	1G
^{76}Ge (86%)	3/25/2016	2.008	2.37	1.89E+19	Au	2.2	2G
^{76}Ge (86%)	3/25/2016	2.008	2.24	1.78E+19	Au	2.59	3G
^{128}Te	3/30/2016	1.999	1.86	8.76E+18	Au	2.46	1E
^{128}Te	3/30/2016	1.999	1.88	8.84E+18	Au	2.11	2E
^{128}Te	3/30/2016	1.999	1.8	8.48E+18	Au	2.48	3E
^{130}Te	4/1/2016	1.998	2.36	1.09E+19	Au	2.4	1H
^{130}Te	4/1/2016	1.998	2.17	1.01E+19	Au	2.32	2F
^{130}Te	4/1/2016	1.998	2.17	1.00E+19	Au	2.33	3F
^{nat}Au	N/A	N/A	2.06	6.30E+18	N/A	N/A	4A
^{nat}Au	N/A	N/A	2.3	7.03E+18	N/A	N/A	1F
^{nat}Au	N/A	N/A	2.5	7.64E+18	N/A	N/A	2H
^{nat}C	N/A	N/A	0.195	9.79E+18	N/A	N/A	3A

CHAPTER 6: The ^{3}He Recovery System

Given the high cost of ^{3}He gas ($600 per atm·L at present), a system to recover and recirculate the gas in the HIS at the TUNL tandem laboratory has been constructed and installed. This section describes the design, performance, and potential improvements of this system.

Section 6.1: Design

The ^{3}He recovery system collects the gas exhausted by the diffusion pump that evacuates the source box, removes all contaminants from the helium, and stores the gas in a reservoir before returning it to the duoplasmatron. The two key considerations in selecting components for the system were: (1) choosing parts that are tested to be helium leak-tight and (2) minimizing volume.

The HIS uses a Varian VHS-10 diffusion pump backed by an Edwards E2M28 two stage rotary-vane pump to evacuate the source box. For ^{4}He operation, this backing pump exhausts to atmosphere. Gas flow at the duoplasmatron was measured to be approximately 1 standard cubic centimeter per minute (sccm) under normal operating conditions using ^{4}He gas.

A schematic diagram of the new ^{3}He recovery system and the original source are shown in Fig. 6.1. To operate the ^{3}He recovery system, valve V6 is closed and valve V8 is opened, feeding the diffusion pump exhaust into the Pfeiffer rotary-vane pump instead of the Edwards rotary-vane pump. The Pfeiffer pump is hermetically sealed to reduce the loss of helium gas from the system. A molecular sieve was placed on the foreline of the Pfeiffer rotary-vane pump to prevent diffusion pump oil from entering the ^{3}He recovery system. Additionally, a liquid nitrogen filled cold trap was placed on this foreline, which serves to condense water

vapor and pump oil out of the source gas. The cold trap also improves the Pfeiffer rotary-vane throughput when the manifold pressure is low. The exhaust from the Pfeiffer rotary-vane pump is fed to a diaphragm compressor pump which is used to refill and pressurize the purifier, which feeds gas through the source manifold and into the duoplasmatron. The gas lines on either side of the compressor are secured to the laboratory floor to isolate vibrations from the compressor. The helium gas purifier is designed to filter out water vapor, hydrocarbons, and oxygen. It doubles as a high-pressure reservoir for the source gas. Gas is fed to the duoplasmatron through a flow meter. The flow rate is determined by both the needle valve (operated remotely from the control room) and regulator R1. The ^{3}He recovery system can be refilled from the ^{3}He gas bottle, which is a 500 ml lecture bottle, through regulator R2.

The rotary-vane pump used in the ^{3}He recovery system is a Pfeiffer Duo 20M. The helium compressor is a KNF N143 double-diaphragm pump. The valves in the ^{3}He recovery system (V7-V17 in Fig. 6.1) are SS-4H and SS-2H stainless steel bellows-sealed valves with Swagelok® connections . The gas lines are constructed from stainless steel tubing, primarily 1/4" diamater with 1/8" tubing on the high pressure side of the compressor to minimize volume. The helium purifier is a VICI model P-100-1 with 1/8" fittings. An electrical interlock prevents the Pfeiffer rotary-vane pump from receiving power when the compressor is not on as it may be damaged by an exhaust overpressure greater than 1.5 atm.

Gas pressure in the ^{3}He recovery manifold is monitored by an MKS 722B baratron gauge. This gauge can read absolute pressures from 400 mTorr up to 5000 Torr. The mass flow meter is an Alicat M20 mass flow meter with a range of 0.05 sccm to 20 sccm.

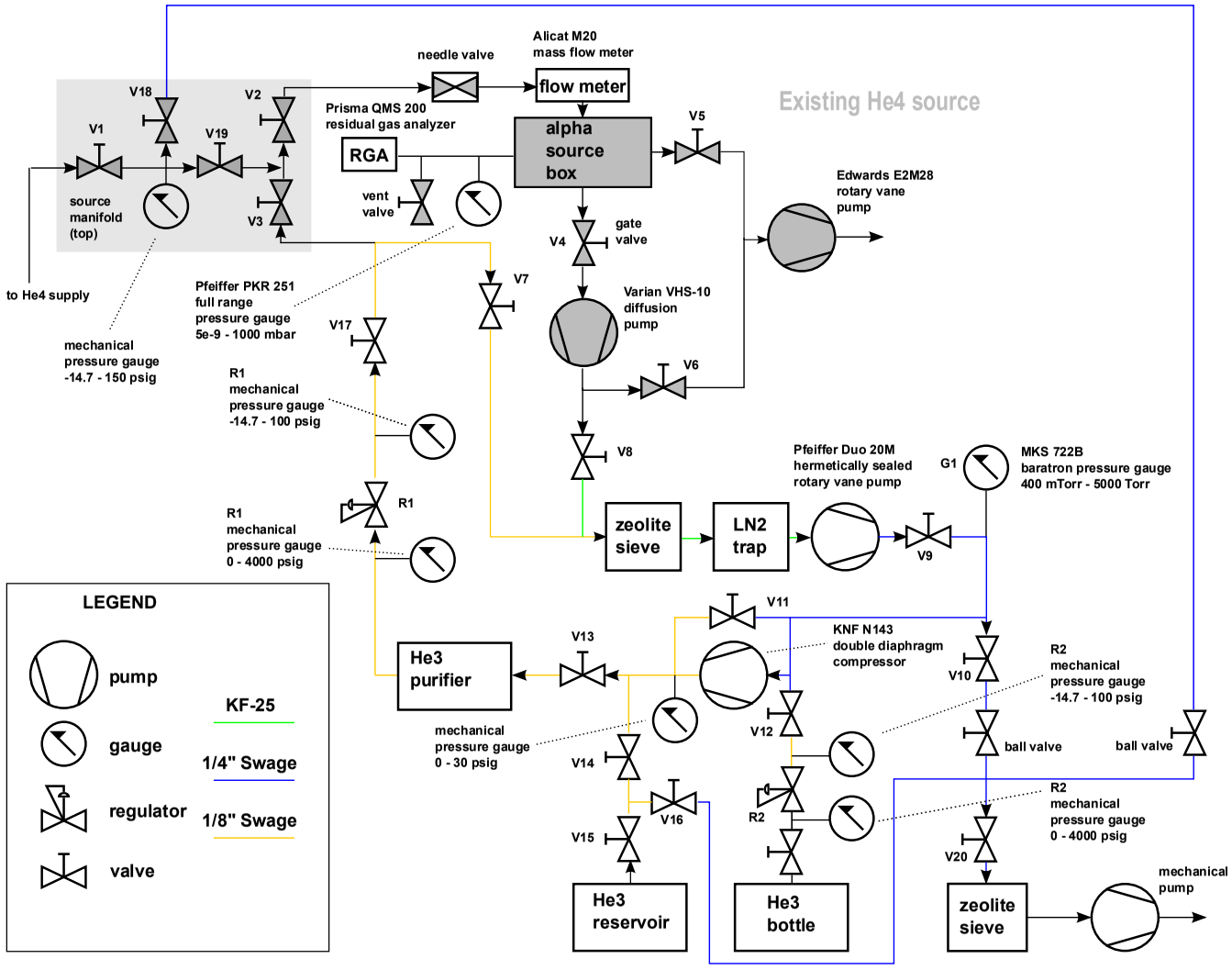

Figure 6.1: A schematic diagram of the ^{3}He ^{3}He recovery system. The shaded components are the original source parts.

Section 6.2: Performance

In order to ascertain the performance of the system, two metrics to track the consumption of gas were devised. The first is the recovery rate. The recovery rate is taken to be the final pressure in the manifold divided by the starting pressure at the beginning of the run. This number tracks the net loss of gas from the ^{3}He recovery system. The average recovery rate using the ^{3}He recovery system was measured to be 0.74±0.10 per day. This rate measurement is the average over six runs with durations from 6 hours to 17 hours. The uncertainty quoted above is the standard deviation in the measurements. A recovery rate measurement was also taken with the gate valve downstream from the source box closed, isolating the source from the beamline. The recovery rate in that configuration was over 0.95 per day, indicating that the primary mechanism for gas loss is flow down the beamline.

The second performance metric compares the actual gas consumption to the estimated consumption without recovery. The flow rate of ^{3}He during this experiment varied between 0.6 and 1.9 sccm or 830 - 2700 mL/day. Using logged flow rates and running times, the consumption without recovery would have been 72 atm·L for all of the runs over the period May 2015 to September 2016. A lecture bottle containing 15 atm·L of 99.9% ^{3}He was purchased from Linde Gas in 2013 specifically for this experiment. As of September 2016, approximately 13±1 atm·L has been consumed. Thus, the recovery system has extended the run time per atm·L of ^{3}He by a factor of about 5.5.

To assess the system's ability to remove contaminants from the source gas, a residual gas analyzer (RGA) was attached to the source box. Fig. 6.2 shows scans that were taken before the initial system loading with no gas flow (background), immediately after starting ^{3}He flow (t=0), and after recirculating for 8 hours. The dominant source of contamination in the gas was found to be primarily water vapor with smaller amounts of hydrogen and nitrogen. No hydrocarbons from pump oil are visible in this spectra.

The beam current created by the HIS when using ^{3}He is comparable to ^{4}He but generally smaller by a factor of approximately 60%. Maximum beam current on the low-energy cup

has ranged between 1.0 and 2.5 μA when using ^{3}He, although beam currents greater than 1.0 μA were never sustained for longer than 12 hours.

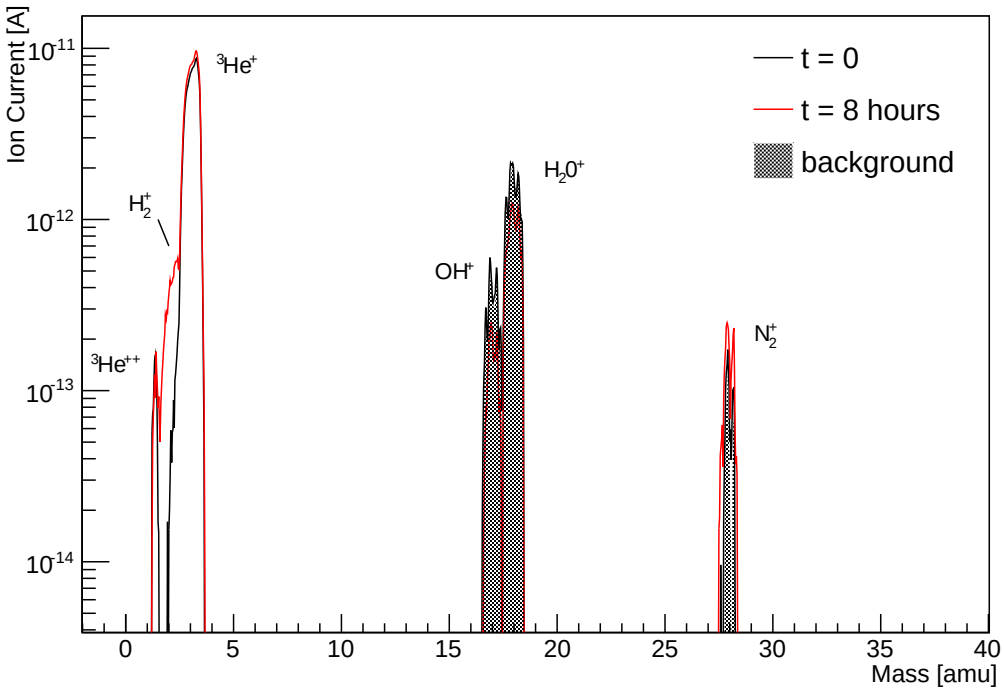

Figure 6.2: RGA scans taken at the source box with no gas flow (background), immediately after the start of gas flow (t=0) and after 8 hours of recirculation.

Section 6.3: Gas Contamination

In April of 2016 a leak in the cooling oil lines on the electrodes in the source box occurred. Fig. 6.3 shows an RGA scan, during ^{3}He operation, taken at the time of the oil leak. The oil lines were repaired and the source box was cleaned thoroughly to remove any visible traces of the oil. However, RGA scans taken during ^{3}He operation after the leak was repaired still showed signs of hydrocarbon contamination. Shortly after the oil leak, the RGA filament failed, was replaced, and failed again. These failures appeared to be directly related to the oil leak. Due to the cost of new filaments and the limited information gained, the RGA was not operated after the second failure.

There are three possible sources of hydrocarbon contamination in the system: (1) diffusion pump oil, (2) rotary-vane pump oil, or (3) electrode cooling oil. Given the lack of hydrocarbon contamination before the leak, it was concluded that the source of the contamination is either a smaller continuing leak in the oil lines or remaining oil residue in the source box. The effect of the oil contamination is a decrease in beam current over time as the gas fed to the duoplasmotron becomes more and more contaminated. This effect was mitigated by filling the system with the smallest amount of gas possible and periodically purging and refilling the system from the ^{3}He bottle when the beam current had diminished by about a factor of 5.

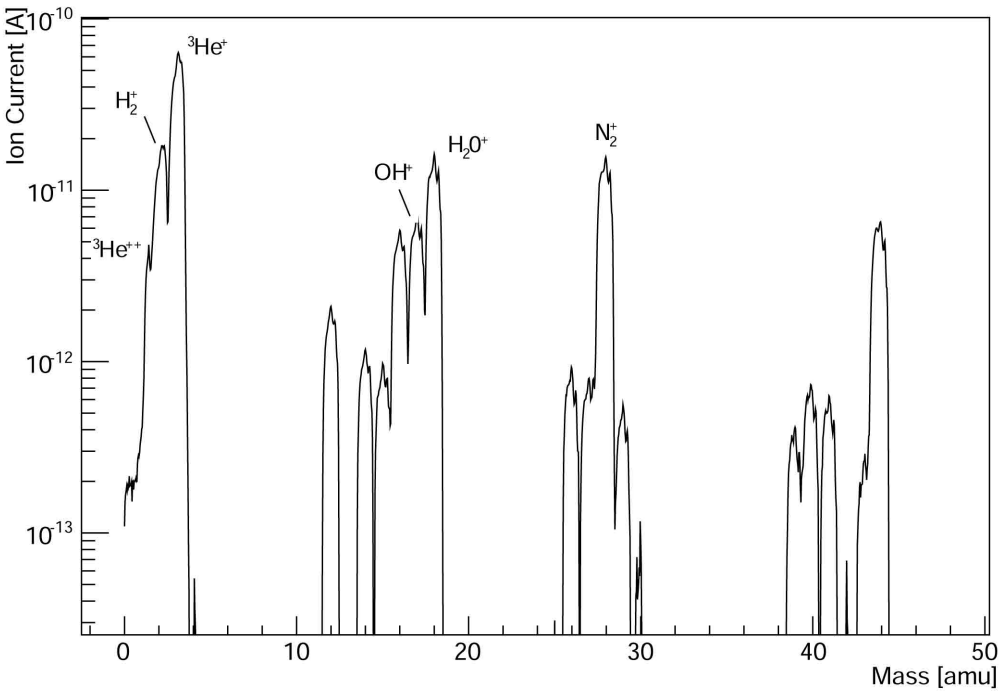

Figure 6.3: An RGA scan taken while cooling oil was leaking into the source box. Hydrocarbon contamination is evident by the peaks not present in Fig. 6.2, particularly at mass 15 (CH_3), 26 (C_2H_2), 27 (C_2H_3), 28 (C_2H_4), 40 (C_3H_4) and 41 (C_3H_5).

Section 6.4: Operation and Maintenance

To minimize ^{3}He use and reduce the effects of contamination in the source gas that happens over time, the system is loaded with 0.4 psi of ^{3}He at the beginning of a run which is enough to last 24 to 48 hours. Typically enough gas to start a run can be loaded by opening the source bottle with valve V12 closed and allowing the regulator body to fill with ^{3}He. After filling the regulator, the valve on the source bottle is closed and then valve V12 is opened, allowing gas to flow into the ^{3}He recovery manifold. If one regulator full of gas is not enough to raise the pressure at G1 to 0.4 psi, the process is repeated until sufficient pressure is built up in the manifold. After 24 to 48 hours, the gas becomes too degraded to continue running and the system must be purged and refilled. As the gas degrades, the beam current drops. The gas should be purged once the DC beam on the low energy cup drops below $\sim$100 nA.

To purge the gas, the ^{3}He recovery system must first be isolated from the source by closing V8 and then opening V6 to back the diffusion pump. Then the ^{3}He recovery manifold is evacuated with a mechanical pump through V20 for 15 minutes. The rotary-vane pump and compressor are allowed to continue running. To keep the arc struck and to prevent sodium vapor from condensing in the attachment electrodes, source gas is switched from ^{3}He to ^{4}He by closing V3 and opening V1. Once the ^{3}He recovery manifold has been evacuated, the system is refilled from the ^{3}He bottle through regulator R2. Valve V1 is closed to stop the flow of ^{4}He. The upper manifold must be evacuated with the mechanical pump through V18 before flowing ^{3}He. Once the upper manifold is evacuated, the flow of ^{3}He to the source is restored by opening V3. Finally, the backing pumps can be swapped back by closing V6 and opening V8.

At the start of each run, the oil level in the Pfeiffer rotary-vane pump must be checked. The fill level is checked by looking at the sight glass on the pump body. Marks indicate the minimum and maximum fill level. Additionally, if the oil is discolored, it should be drained and refilled.

At the end of each run, as much remaining ^{3}He as possible must be stored in a leak-tight section of the recovery system, such as the purifier.

When the ^{3}He recovery system has not been used for > 2 weeks, it must be evacuated through V20 using the mechanical pump due to small leaks, which are discussed in section 6.5.

Over time the filter media in the gas purifier becomes saturated and it will no longer remove contaminants from the gas. The helium purifier should be replaced every 1500 hours, assuming an average flow rate of 0.6 sccm to prevent it from becoming saturated.

Step-by-step procedures for operating the ^{3}He recovery system may be found in Appendix 8.3.

Section 6.5: Improvements

As of this writing, there are small leaks in the manifold and reservoir. These leaks are small enough to prevent serious contamination or ^{3}He loss on the timescale of a several day run, but cause gas stored in the system for > 2 weeks to become contaminated with air. This makes it necessary to evacuate the system at the beginning of each run. In order to reduce leaks in the recovery system, one improvement would be to replace the Swagelok® connections with welded VCR fittings Swa [2016]. VCR fittings meet a much more stringent helium leak test certification than Swagelok® fittings. VCR fittings are guaranteed to have a maximum leak rate of better than 4×10^{-11} std cm^2/s whereas Swagelok® fittings are only guaranteed to be better than 1.5×10^{-5} std cm^2/s (Swa [2008]). Swagelok® fittings are only necessary at either end of the purifier, as the purifier needs to be replaced periodically and is manufactured with those fittings. Another possible solution for reducing leaks would be to replace as much of the steel tubing as possible with a single block of stainless steel with channels machined through it. Placing a digital pressure gauge at the connection between the ^{3}He bottle and the manifold would improve the precision in determining the gas pressure in the bottle and would improve the precision in determining the consumption rate of ^{3}He.

Currently, the pressure in the ^{3}He bottle is measured with the analog pressure gauge on regulator R2. This gauge ranges from 0 to 4000 psi. Since the pressure in the gas bottle is less than 500 psi and filling the ^{3}He recovery system lowers the bottle pressure by about 10 psi, the precision for determining the bottle pressure is limited. Another improvement would be to install a hydrogen getter in the source box to eliminate hydrogen loading in the source gas.

Addressing the problem of gas loss down the beamline by attempting to recover gas from the high-vacuum pump on the negative ion source (NIS) inflection magnet might significantly improve the current 74%/day recovery rate. This high-vacuum pump, the first one downstream from the HIS, is presumed to exhaust the majority of the lost source gas.

CHAPTER 7: Data Analysis

Time-of-flight (TOF) spectra for germanium targets with gold backing and gold-only targets were accumulated at each detector angle. These spectra were 4095 channels long and data was contained in 2048 bins (i.e., in each histogram, the domain was 0-4095 and each data bin spanned 2 units). The TDC was set to an 800 ns range and the time calibration for each spectrum was 0.1808 ns per channel. The data in each spectrum were accumulated with a 1x Cs PH (477 keVee) threshold and a visually chosen PSD threshold to exclude gammas. The PH threshold settings were checked at the beginning and end of each experimental run using a ^{137}Cs gamma source. PSD thresholds were set using a ^{241}Am-Be neutron source and verified using the neutrons produced by the (^3He,n) reaction with the beam on target.

A TOF histogram accumulated with a 15-MeV ^{3}He beam incident on a ^{74}Ge target (gold foil backing) and a liquid scintillator detector positioned at 0° is shown in Fig. 7.1. A PH threshold and PSD cut were applied as described above. Each foreground TOF spectrum was characterized by a gamma peak above channel 3000, a clear peak due to two-proton transfer to the ground state of the residual nucleus between channels 2300-2600, and a large mound below the ground state peak corresponding to two-proton transfer to the continuum of states in the residual nucleus. Peaks from carbon contamination were present in the continuum region. The carbon contamination was caused by beam-induced heating of the target foil in the presence of trace hydrocarbons from pump oil. These contamination peaks were observed to grow as a target was exposed to beam. Increasing the beam energy increased the rate of growth. New targets did not exhibit contamination when first exposed to beam.

Four data sets were collected, corresponding to targets of isotopically enriched ^{74}Ge and ^{76}Ge at ^{3}He beam energies of 15 MeV and 21 MeV. The TOF spectra were shifted horizontally to overlay the gamma peaks and then summed at each angle. This was done with macros

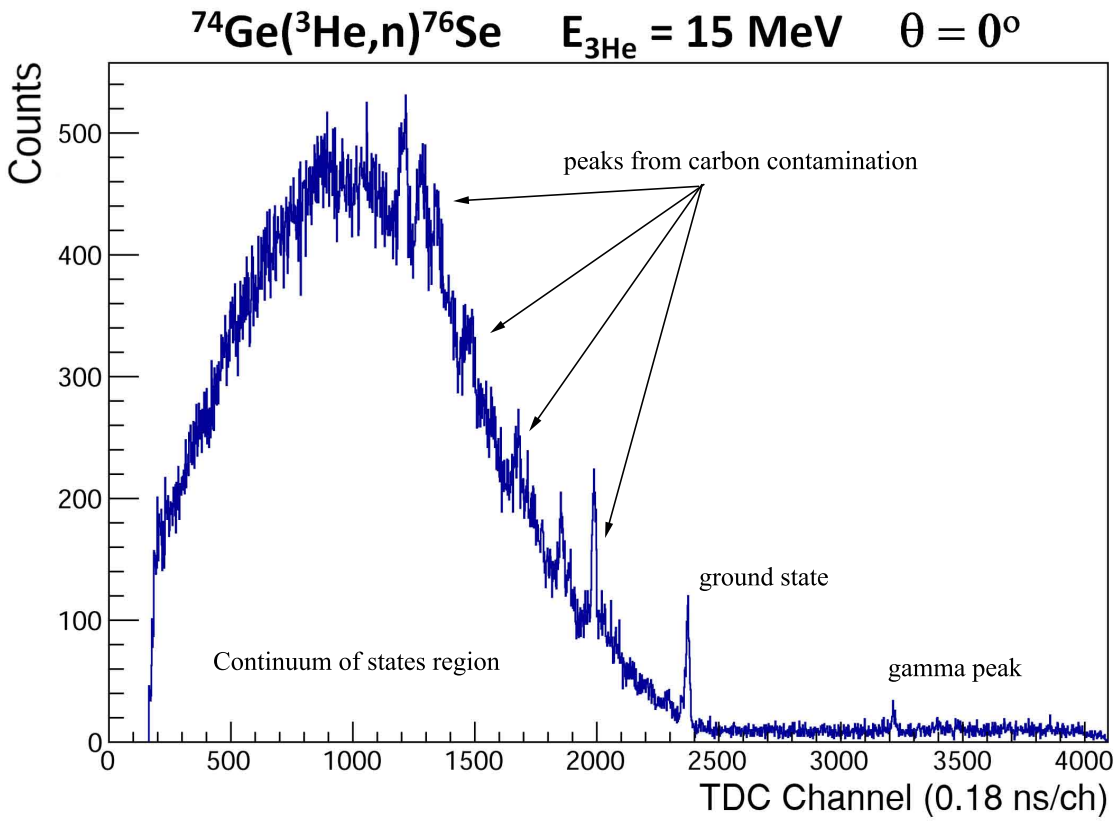

Figure 7.1: A TOF spectrum from a ^{74}Ge target with gold backing at 15 MeV. This histogram was accumulated with 1 x CS PH threshold and a PSD cut. The gamma peak, ground state, continuum of states, and carbon peaks are indicated. The small size of the gamma peak demonstrates the effectiveness of PSD.

written for the CERN ROOT data analysis software package. In all cases, TOF spectra from gold-only targets did not exhibit any structure in the region of interest (ROI) (see Fig. 7.2). Therefore, the background was approximated by fitting the counts on both sides of the ROI rather than performing an arithmetic subtraction of the normalized spectrum taken with a gold foil. This procedure results in a smaller statistical uncertainty than is obtained with the subtraction of the measured TOF with a gold target.

The differential cross section at each angle for each transition was computed from the integrated counts in the corresponding peak in the neutron TOF histograms using equation 4.2. *LT* was typically 0.8-0.9 and *PO* was typically 0.8-1.0 during this experiment. For the doubly-ionized ^{3}He beam used in this experiment, $charge\ state = 2$. At each angle, $N_{det} =$

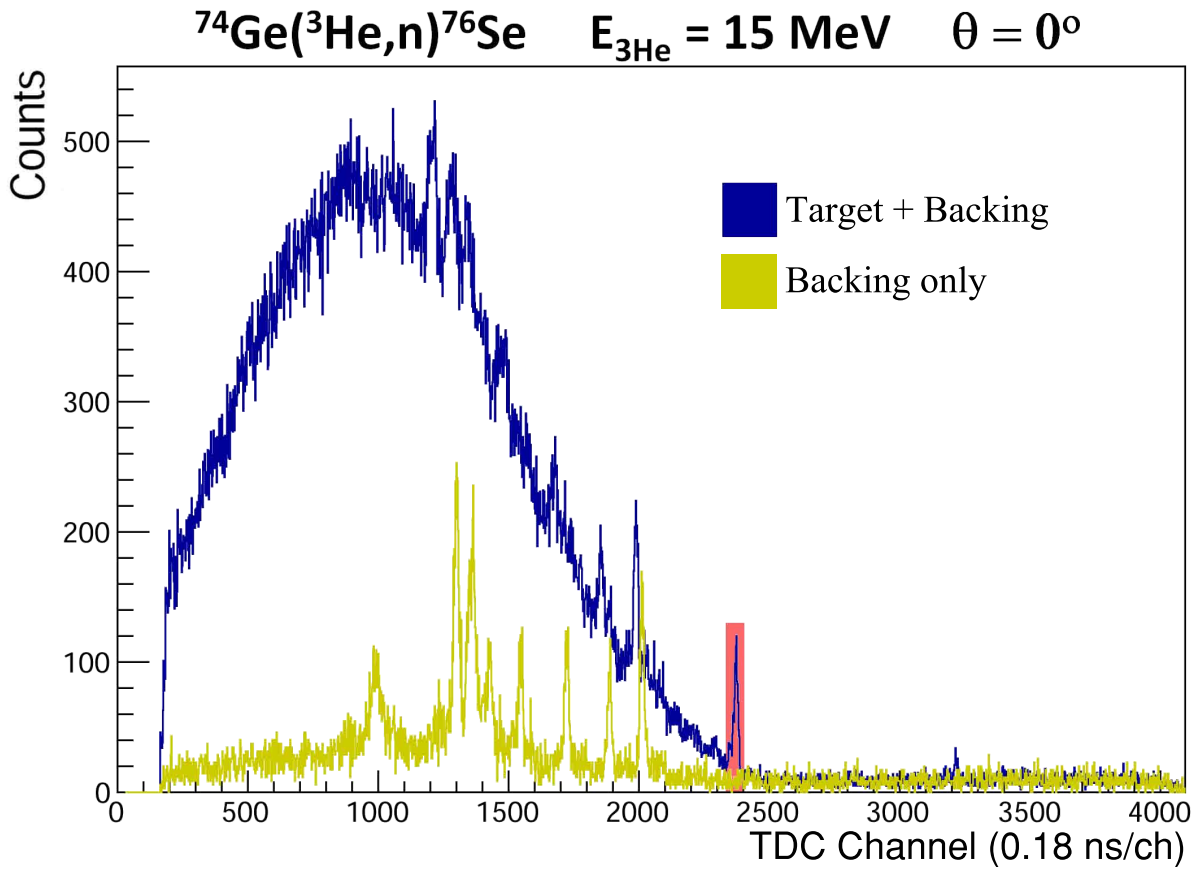

Figure 7.2: An overlay of TOF spectra from the ^{74}Ge target with ^{nat}Au backing (blue curve) and the (normalized) ^{nat}Au-only target (gold curve). The ^{nat}Au target does not exhibit any structure within the ROI (highlighted in red), justifying a fit of the foreground spectra outside the ROI rather than arithmetic background subtraction.

3, r = 6.35 cm, and l = 1,300 cm.

Neutron yields were obtained by fitting each peak of interest in the TOF histograms with a Gaussian function. The integrated peak counts for each peak is computed as the area under the Gaussian fit given by a simple form:

$$Y = \int_{-\infty}^{\infty} Ae^{-0.5\left(\frac{x-\mu}{\sigma}\right)^2} dx = \sqrt{2\pi}A\sigma \tag{7.1}$$

where A is the amplitude, μ is the centroid, and σ is the width.

Functional fits to the peaks in the ROI in the neutron TOF histograms were calculated

using the TMinuit class with the log-likelihood method in ROOT. The procedure for fitting the peaks in the ROI in the neutron TOF histograms was slightly different for the ^{74}Ge(^{3}He,n) data at 15 MeV than the other data. The two main distinctions were: (1) there was a noticeable foot on the long-time side of the ^{3}He beam pulse that created an asymmetry in the shape of the beam bunch time profile; and (2) there was significant strength for two-proton transfer to the first excited 2^{+} state in ^{76}Se. For these reasons the analysis of the ^{74}Ge(^{3}He,n) data at 15 MeV is discussed separately.

The cross sections measured in this work are reported in Tables 7.1-7.4. The data for each target and incident ^{3}He beam energy is given in a separate table. The cross sections for each angle are tabulated for two-proton transfer to the ground state and excited state in the residual nucleus. The statistical uncertainties, which are strongly angle dependent, are given in the tables. The systematic uncertainties, which are only mildly angle dependent, are summarized in Table 7.5. The determination of background and neutron yields are given in the next sections, followed by a discussion of determining the statistical and systematic uncertainties

Section 7.1: Background Determination and Histogram Fitting for ^{74}Ge(^{3}He,n) at 15 MeV

The ROI for the ^{74}Ge target at 15 MeV was sufficiently separated from the continuum of states region to allow a flat background approximation (see Fig. 7.3). The background was determined at each angle by integrating the region between the ground state peak and gamma peak, then dividing by the number of integrated bins.

The ground state peak was fit with two offset Gaussian functions to account for an asymmetric beam pulsing profile. The relative amplitudes of and horizontal offset between the two Gaussians were determined by fitting the timing peak from the elastically scattered ^{3}He particles measured with the solid state detector.

The first 2^{+} and 0^{+} excited state peaks, each much smaller than the ground state, were fit

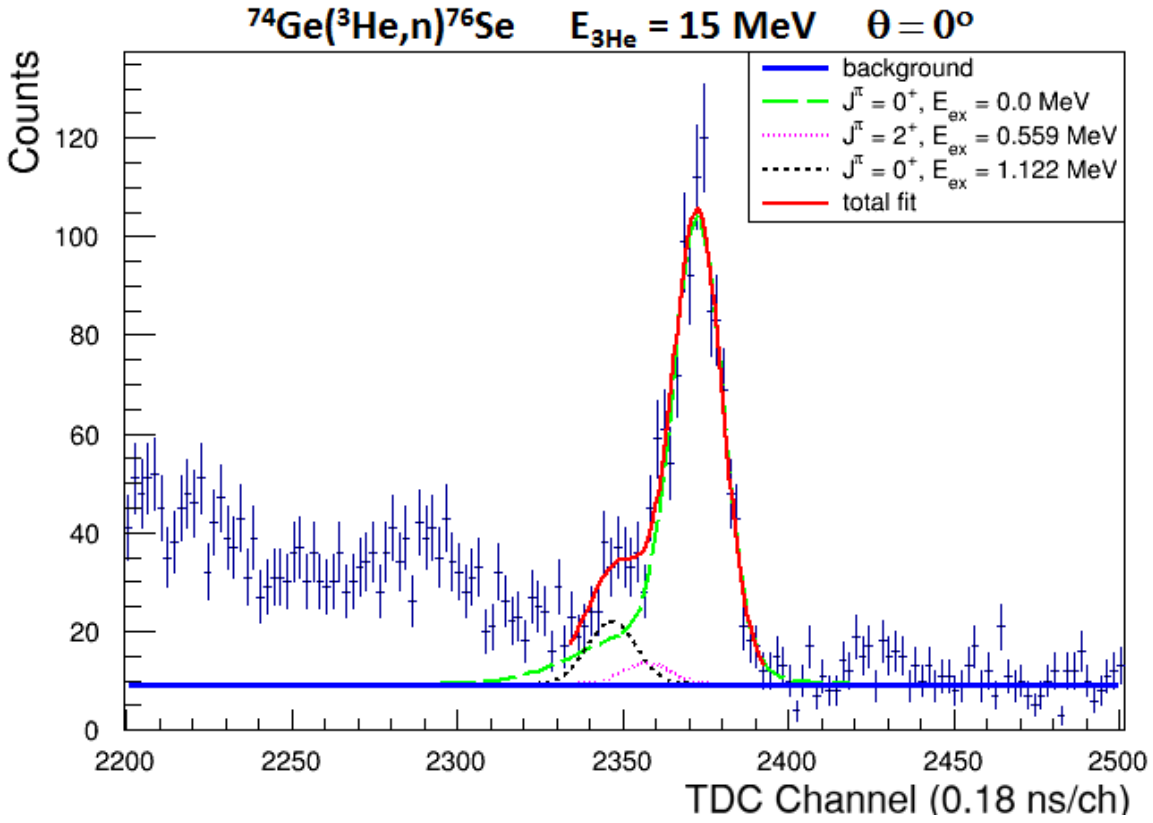

Figure 7.3: A TOF spectrum from the ^{74}Ge target at 15 MeV showing the fits used to extract cross sections.

with single Gaussians. The excited state peaks were fit by fixing the width of the Gaussian function to be the same as determined in the fit to the peak for the ground-state transfer. The centroids of the fit functions to the excited states were fixed to values calculated from the reaction kinematics.

The width of each Gaussian was fixed to the same value at all angles. This value was determined by fitting the high-energy (e.g. right) half of the ground state peak at 0°, 3°, 6°, and 9° with a single Gaussian and calculating the weighted average of the fitted widths.

At each angle, the centroid of the ground state peak was also determined by fitting the high-energy half of the ground state peak with a single Gaussian. In summary, the final fit at each angle had 4 free parameters: the ground state amplitude, the ground state centroid, the 0^{+} excited state amplitude, and the 2^{+} excited state amplitude.

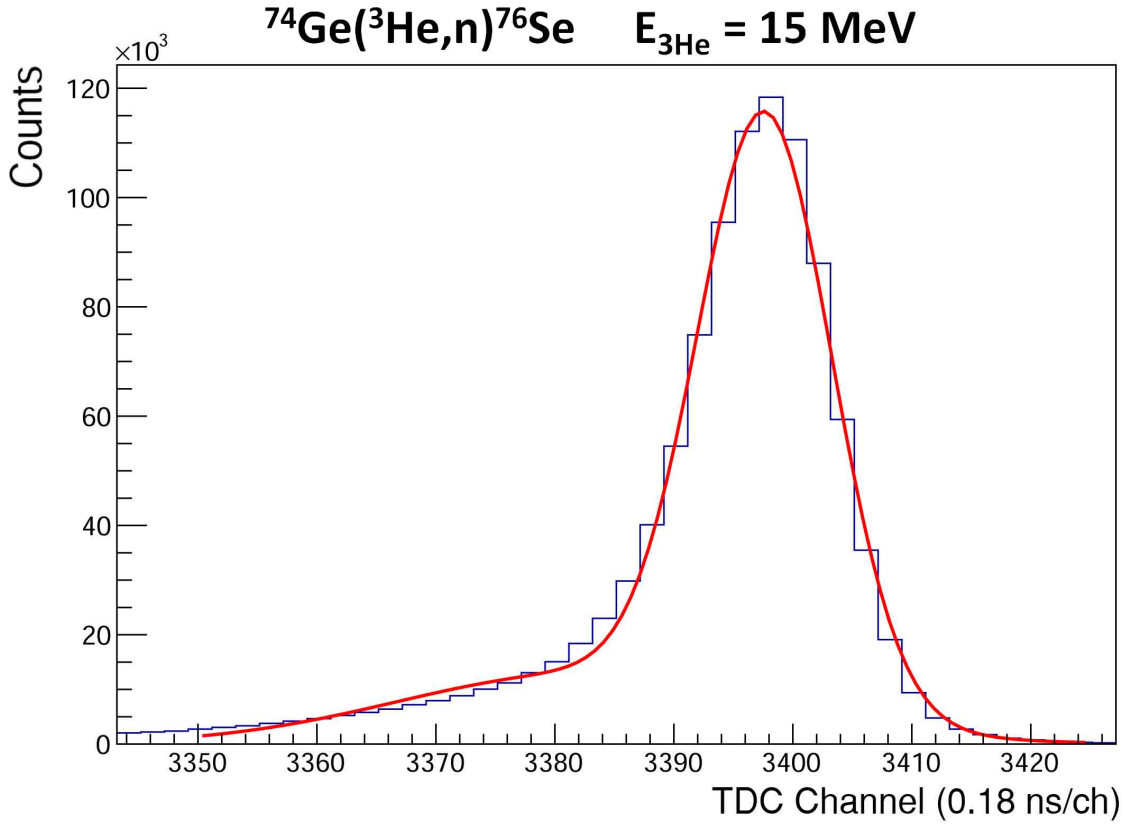

Figure 7.4: A TOF spectrum from the solid state detector overlaid with the double gaussian fit to the asymmetric timing peak for the ^{74}Ge target at 15 MeV.

Section 7.2: Background Determination and Histogram Fitting for ^{74}Ge(^{3}He,n) at 21 MeV and ^{76}Ge(^{3}He,n) at 15 and 21 MeV

A slightly different technique was used to extract yields from the ^{76}Ge data and the ^{74}Ge data at 21 MeV. These data sets each had symmetric beam pulse timing profiles but did not have a flat background in the ROI. The improvement in the symmetry of the beam bunch time profile for these data reflects the experience with ^{3}He beam pulsing acquired by our research team during the execution of the experiment. Backgrounds at 21 MeV were not flat in the ROI because of the increased number of open states available in the residual nucleus, and because the ^{76}Ge targets were only enriched to 87.31%, which means the targets are 12.69% ^{74}Ge.

The background in the ROI was modeled with a function that consisted of a Gaussian

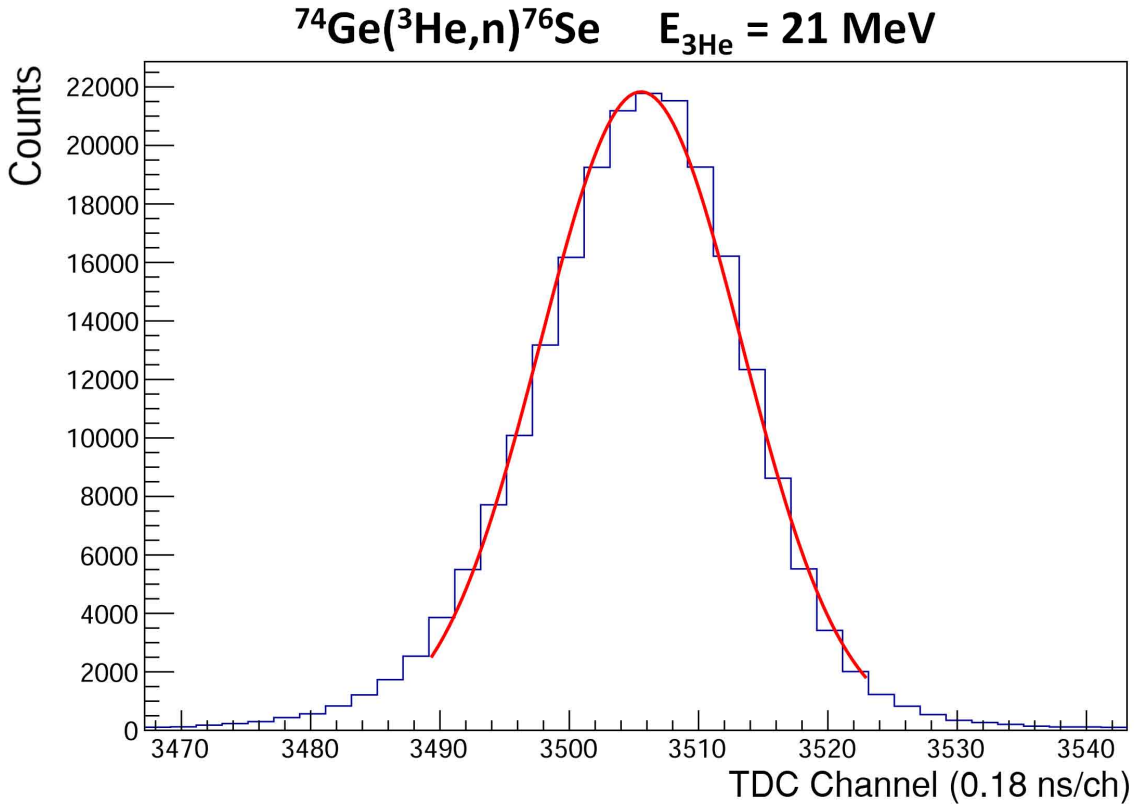

Figure 7.5: A TOF spectrum from the solid state detector overlaid with a single Gaussian fit to the symmetric timing peak for the ^{74}Ge target at 21 MeV.

function plus a constant (i.e., a vertical offset). The constant was determined by the same method as for the ^{74}Ge data at 15 MeV, i.e., by integrating the data between the ground state and gamma peaks then dividing by the number of integrated bins. The centroid, width and amplitude parameters of the Gaussian were then determined by fitting the region on the low-energy side of the ROI minus the constant level that was fitted to the counts on the high-energy side of the ROI.

The ^{3}He beam pulses were symmetric time distributions for these data sets, enabling a single Gaussian function to be used to fit the peaks in the neutron TOF spectra. For each data set, the widths of the Gaussians used to fit the peaks were fixed to the same value. This value was determined by the method described in section 7.1. The centroid of the Gaussian used to fit the ground state peak was also determined by the same method described in

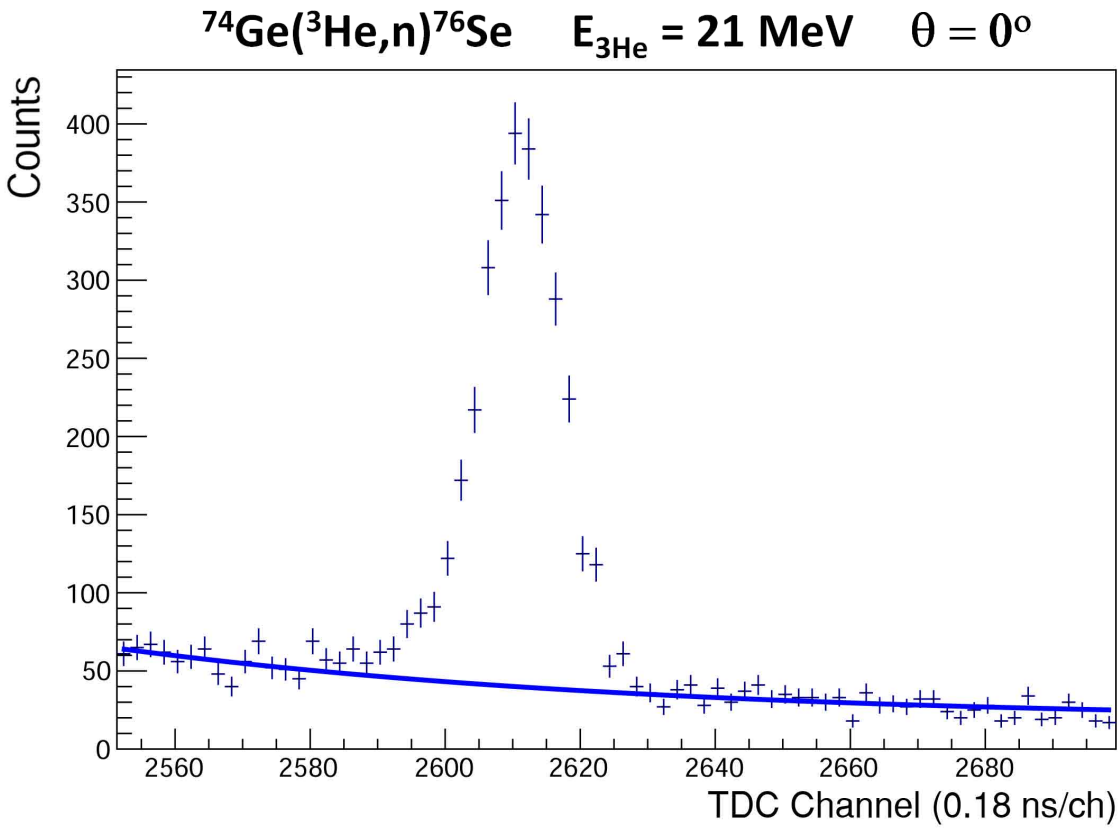

Figure 7.6: A TOF spectrum from the ^{74}Ge target at 21 MeV showing the fit used to determine background counts. The peak region was excluded from the background fit (2580-2630).

section 7.1.

These data sets were fit well without including a 2^+ excited state (see Figs. 7.7 and 7.8). The 2^+ peaks become convoluted with 0^+ peaks in these data sets. Similar to the data from ^{74}Ge at 15 MeV, the amplitude of the Gaussian fitted to the first excited 0^+ state was allowed to vary while the centroid was fixed relative to the ground state centroid using the calculated energy shift between the states.

The analysis of the data from the ^{76}Ge target had two additional considerations: (1) the presence of two closely spaced 0^+ excited states, and (2) contamination from ^{74}Ge. The first two 0^+ excited states in the residual nucleus, ^{78}Se, are spaced 360 keV apart. The spacing was too small to resolve the states, so a single Gaussian was used to fit both states.

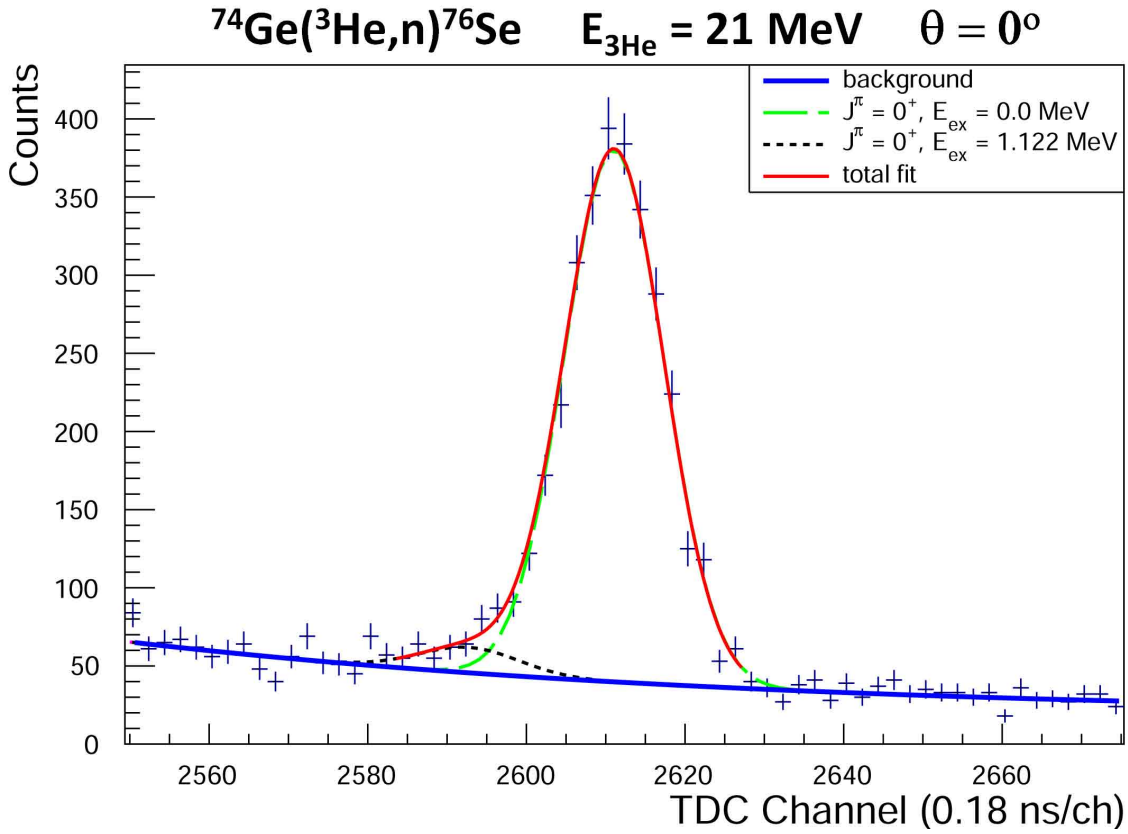

Figure 7.7: A TOF spectrum from the ^{74}Ge target at 21 MeV showing the fits used to extract cross sections.

The centroid of this Gaussian was fixed relative to the centroid of the ground state at the position calculated for the first 0^+ excited state (It was assumed that the ^{76}Ge(^3He,n)^{78}Se cross section to the second 0^+ excited state was much smaller than the cross section to the first 0^+ excited state).

Contamination from ^{74}Ge in the ^{76}Ge targets produced a peak in the TOF spectra, corresponding to the ground state in ^{76}Se, that unfortunately overlapped with the peak corresponding to the first 0^+ excited state in ^{78}Se. To account for this, cross section data from Tables 7.1 and 7.2 were used with the known amount of ^{74}Ge contamination (see Table 5.1) and equation 4.2 to calculate an expected ^{74}Ge(^3He,n)^{76}Se neutron yield at each angle and beam energy. Using these yields and the energy of these neutrons (1.981 MeV less than neutrons corresponding to the ground state of ^{78}Se), a Gaussian function with no free

parameters was defined at each angle and beam energy to represent the expected contribution from ^{74}Ge(^{3}He,n)^{76}Se to each ^{76}Ge(^{3}He,n)^{78}Se TOF spectra (e.g., the purple dashed line in Fig. 7.8). The uncertainties in the ^{74}Ge(^{3}He,n)^{76}Se cross sections were propagated to the uncertainties in the cross sections for two-proton transfer to the first 0^{+} excited states in ^{78}Se, and this accounts for the relatively larger errors in these measurements.

The cross sections measured in this work are given in Tables 7.1, 7.2, 7.3, and 7.4. The same cross sections are plotted in Figs. 7.9, 7.10, 7.11, and 7.12.

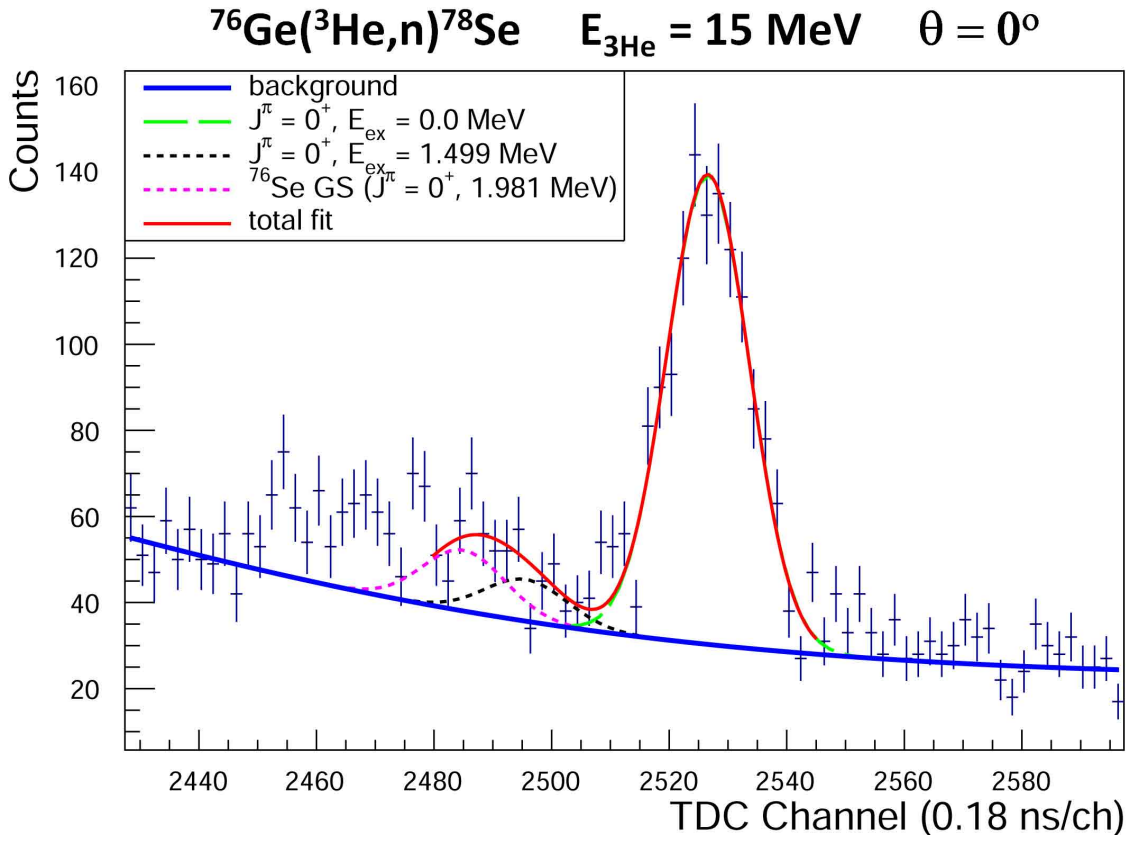

Figure 7.8: A TOF spectrum from the 76Ge target at 15 MeV showing the fits used to extract cross sections. The Gaussian function used to account for the ^{74}Ge contamination did not have any free parameters.

Section 7.3: Error Analysis

Statistical errors of the measured cross sections were propagated from the error in the fitting parameters, assuming zero correlation between parameters. For a general function $f(x_1, \ldots, x_i)$, the error in the function Δf is given by

$$\Delta f = \sqrt{\left(\frac{\partial f}{\partial x_1}\right)^2 (\Delta x_1)^2 + \ldots + \left(\frac{\partial f}{\partial x_i}\right)^2 (\Delta x_i)^2} \tag{7.2}$$

where $\Delta x_1, \ldots, \Delta x_i$ are the errors in $x_1, \ldots, x_i$.

Therefore, the statistical error in the yields (equation 7.1) is given by

$$(\Delta Y)_{stat} = Y \sqrt{\left(\frac{\Delta A}{A}\right)^2 + \left(\frac{\Delta \sigma}{\sigma}\right)^2} \tag{7.3}$$

and the statistical error in the cross section (equation 4.2) is given by

$$\Delta \left(\frac{d\sigma}{d\Omega}\right)_{stat} = \frac{d\sigma}{d\Omega} \times \frac{(\Delta Y_n)_{stat}}{Y_n} \tag{7.4}$$

since all terms besides Y_n in equation 4.2 have negligible (an order of magnitude or more smaller) statistical errors.

The main source of systematic errors in the measured cross sections were due to the uncertainties in the detector efficiencies, target thicknesses, and neutron yields. Errors in N_{3He} and $d\Omega$ were negligible ($< 0.5\%$), see table 7.5.

$$\Delta \left(\frac{d\sigma}{d\Omega}\right)_{sys} = \frac{d\sigma}{d\Omega} \sqrt{\left(\frac{\Delta \epsilon}{\epsilon}\right)^2 + \left(\frac{\Delta n_{Ge}}{n_{Ge}}\right)^2 + \left(\frac{(\Delta Y_n)_{sys}}{Y_n}\right)^2} \tag{7.5}$$

The source of $\Delta\epsilon$ is discussed in chapter 4 and the source of Δn_{Ge} is discussed in chapter 5. The source of $(\Delta Y_n)_{sys}$ is the background approximation. The systematic (i.e. shape) uncertainty in the background counts for all targets, energies, and angles is estimated to be 10%. Because the ratio $foregorund : background$ varied from about 5 at 0° to 1 at 18°, the value of $(\Delta Y_n)_{sys}$ ranged from 2% at 0° to 5% at 18°.

Table 7.1: Cross Sections Measured for the ^{74}Ge(^{3}He,n)^{76}Se reaction at E_{3He} = 15 MeV

	Ground State $J^\pi = 0^+$ $E_{ex} = 0$ MeV		Excited State $J^\pi = 2^+$ $E_{ex} = 0.559$ MeV		Excited State $J^\pi = 0^+$ $E_{ex} = 1.122$ MeV	
Lab Angle	$\frac{d\sigma_{cm}}{d\Omega}$ (mb/sr)	stat. error	$\frac{d\sigma_{cm}}{d\Omega}$ (mb/sr)	stat. error	$\frac{d\sigma_{cm}}{d\Omega}$ (mb/sr)	stat. error
0°	0.298	± 0.026	0.011	± 0.009	0.033	± 0.008
3°	0.281	± 0.024	0.024	± 0.008	0.021	± 0.006
6°	0.238	± 0.021	0.031	± 0.009	0.018	± 0.007
9°	0.177	± 0.017	0.025	± 0.008	0.022	± 0.007
12°	0.106	± 0.012	0.033	± 0.009	0.013	± 0.008
15°	0.060	± 0.009	0.019	± 0.008	0.012	± 0.008
18°	0.046	± 0.007	0.014	± 0.007	0.010	± 0.006

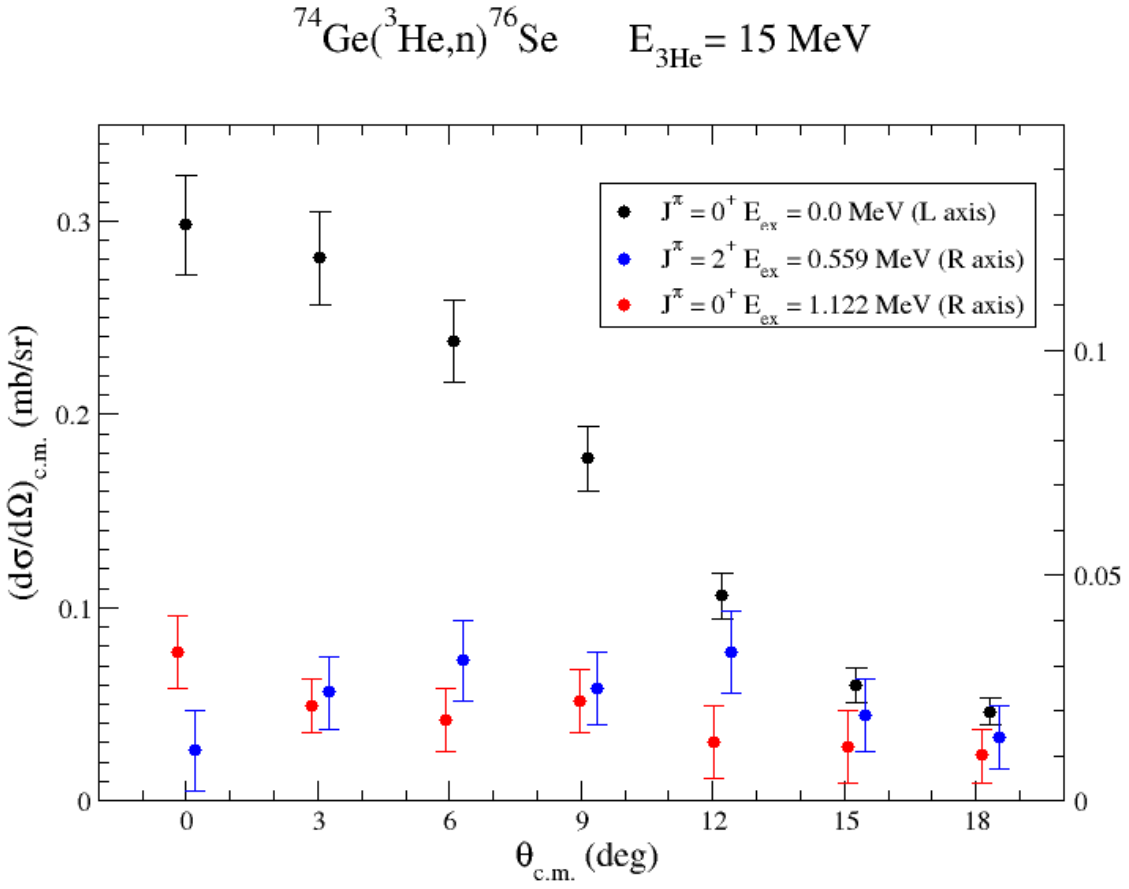

Figure 7.9: Cross Sections Measured for the ^{74}Ge(^{3}He,n)^{76}Se reaction at E_{3He} = 15 MeV. Excited state cross sections are plotted on the right axis. Errors on data points are statistical only.

Table 7.2: Cross Sections Measured for the ^{74}Ge(^{3}He,n)^{76}Se reaction at E_{3He} = 21 MeV

	Ground State $J^\pi = 0^+$ $E_{ex} = 0$ MeV		Excited State $J^\pi = 0^+$ $E_{ex} = 1.122$ MeV	
Lab Angle	$\frac{d\sigma_{cm}}{d\Omega}$ (mb/sr)	stat. error	$\frac{d\sigma_{cm}}{d\Omega}$ (mb/sr)	stat. error
0°	0.724	± 0.019	0.035	± 0.008
3°	0.600	± 0.017	0.031	± 0.006
6°	0.539	± 0.016	0.037	± 0.006
9°	0.304	± 0.011	0.018	± 0.006
12°	0.158	± 0.008	0.019	± 0.006
15°	0.044	± 0.006	0.017	± 0.006
18°	0.043	± 0.005	0.007	± 0.005

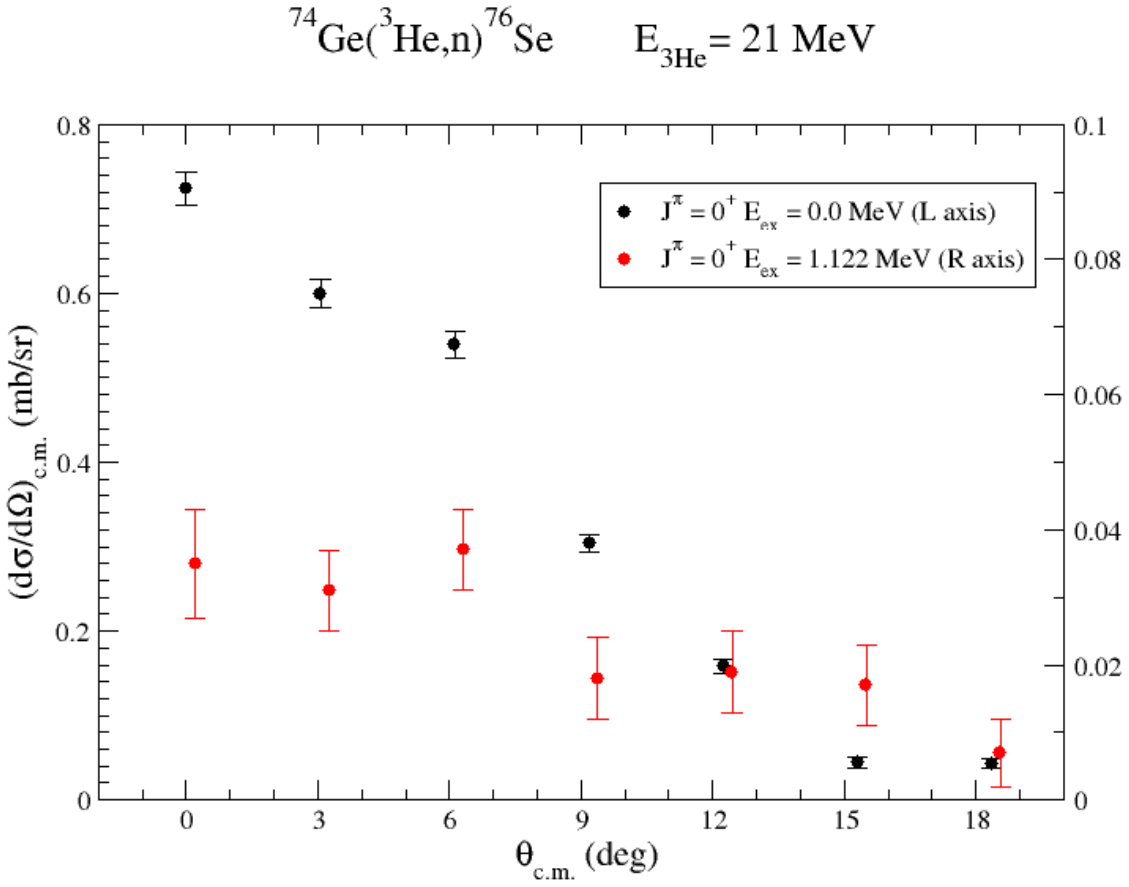

Figure 7.10: Cross Sections Measured for the ^{74}Ge(^{3}He,n)^{76}Se reaction at E_{3He} = 21 MeV. Excited state cross sections are plotted on the right axis. Errors on data points are statistical only.

Table 7.3: Cross Sections Measured for the ^{76}Ge(^{3}He,n)^{78}Se reaction at E_{3He} = 15 MeV

	Ground State $J^\pi = 0^+$ E_{ex} = 0 MeV		Excited State $J^\pi = 0^+$ E_{ex} = 1.499 MeV	
Lab Angle	$\frac{d\sigma_{cm}}{d\Omega}$ (mb/sr)	stat. error	$\frac{d\sigma_{cm}}{d\Omega}$ (mb/sr)	stat. error
0°	0.177	± 0.009	0.016	± 0.005
3°	0.159	± 0.008	0.019	± 0.004
6°	0.143	± 0.007	0.014	± 0.004
9°	0.095	± 0.006	0.008	± 0.004
12°	0.062	± 0.005	0.008	± 0.004
15°	0.035	± 0.005	0.000	
18°	0.021	± 0.004	0.000	

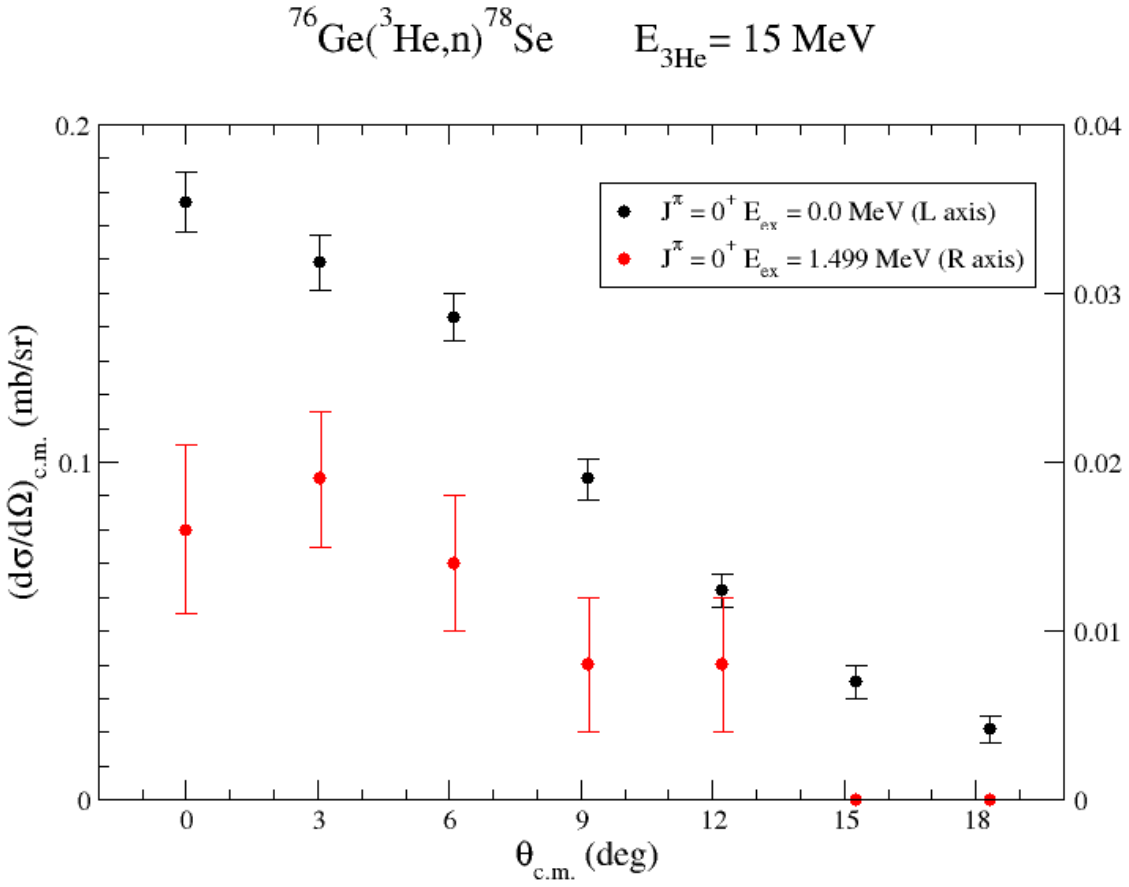

Figure 7.11: Cross Sections Measured for the ^{76}Ge(^{3}He,n)^{78}Se reaction at E_{3He} = 15 MeV. Excited state cross sections are plotted on the right axis. Errors on data points are statistical only.

Table 7.4: Cross Sections Measured for the ^{76}Ge(^{3}He,n)^{78}Se reaction at E_{3He} = 21 MeV

	Ground State $J^\pi = 0^+$ $E_{ex} = 0$ MeV		Excited State $J^\pi = 0^+$ $E_{ex} = 1.499$ MeV	
Lab Angle	$\frac{d\sigma_{cm}}{d\Omega}$ (mb/sr)	stat. error	$\frac{d\sigma_{cm}}{d\Omega}$ (mb/sr)	stat. error
0°	0.487	± 0.015	0.063	± 0.008
3°	0.415	± 0.013	0.050	± 0.006
6°	0.361	± 0.012	0.045	± 0.006
9°	0.185	± 0.008	0.017	± 0.005
12°	0.098	± 0.006	0.010	± 0.005
15°	0.015	± 0.005	0.000	
18°	0.005	± 0.004	0.000	

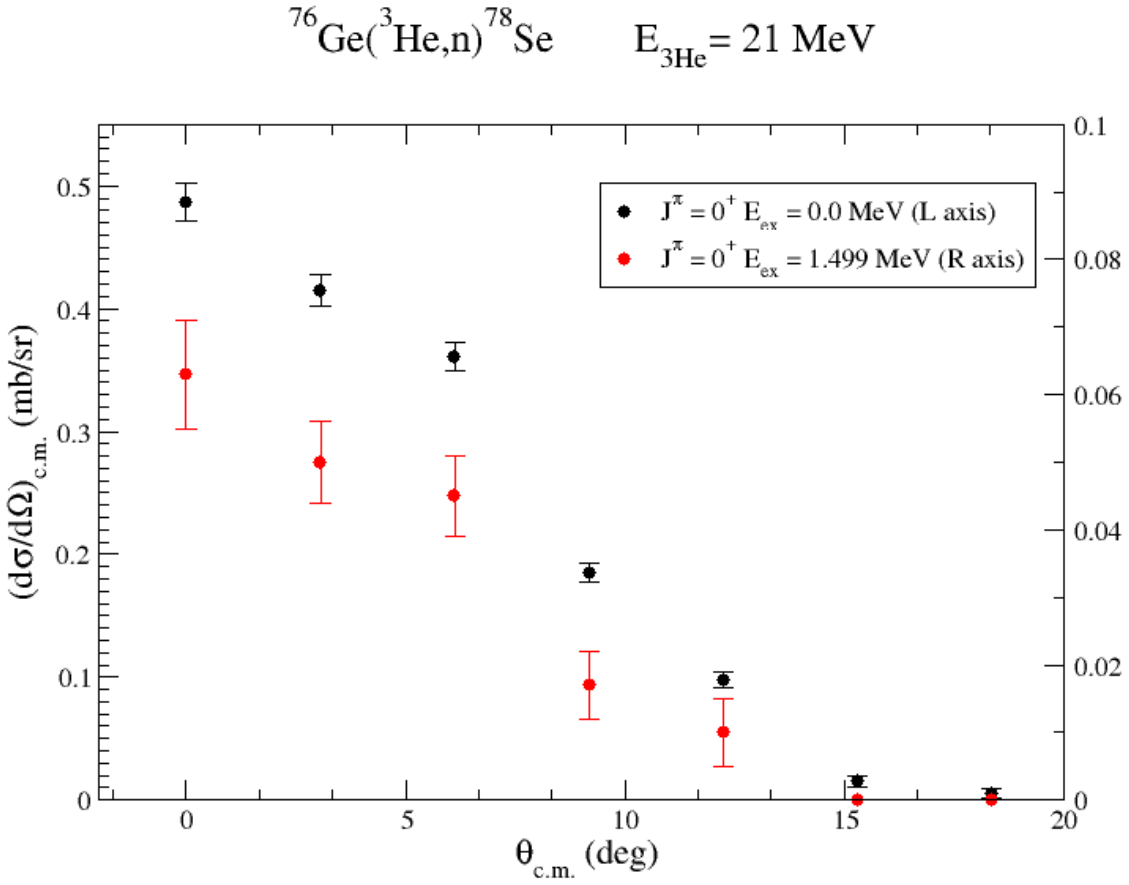

Figure 7.12: Cross Sections Measured for the ^{76}Ge(^{3}He,n)^{78}Se reaction at E_{3He} = 21 MeV. Excited state cross sections are plotted on the right axis. Errors on data points are statistical only.

Table 7.5: Summary of Systematic Errors

Quantity	Source of Error	Size Estimate
ϵ	uncertainty in absolute efficiencies	$\pm 6\%$
	uncertainty in shape of calculated efficiency curve	$\pm 4\%$
n_{Ge}	thickness variation across surface of target	$\pm 5\%$
Y_n	background approximation	$\pm 2\%$ - $\pm 5\%$
total		$\pm 9\%$ - $\pm 10\%$

CHAPTER 8: Results and Conclusions

The two main objectives of this project were: (1) to investigate the validity of applying the BCS model approximation for the wavefunctions used in QRPA calculations of nuclear matrix elements for $0\nu\beta\beta$ of ^{76}Ge, and (2) to study the particle transfer mechanisms involved in two-proton drop-off reactions. The results and conclusions for each goal are discussed in this chapter, starting with the first motivation.

Section 8.1: Assessment of BCS Approximation Using Two-Proton Drop-Off Measurements

As discussed in chapter 2, the validity of the BCS model approximation may be tested using two-nucleon transfer reactions (e.g., (t,p), (p,t), $(^3He,n)$, or $(n,^3He)$ reactions). $(^3He,n)$ differential cross-section measurements on ^{74}Ge and ^{76}Ge were performed for this work. If the two-level model of Section 2.2 is a valid approximation, then it is expected that the strengths for two-proton transfer to the 0^+ excited states will be less than $\sim$10% of the ground state strength (Freeman and Schiffer [2012]). An examination was conducted of the relative strength to the first 0^+ excited state, which should dominate the transfer to the excited 0^+ states.

The relative strength for two-proton transfer at 0° to the first 0^+ excited state in the residual nuclei of ^{76}Se and ^{78}Se that were measured in this work are summarized in Table 8.1. For both nuclei, and at both energies measured, the observed relative strengths were less than about 13%. This result supports the validity of using the BCS model approximation to describe the ground state of both ^{76}Se and ^{78}Se. These results are consistent with measurements made in 2013 of the same reaction at 16 MeV beam energy by Roberts et al. [2013]. In that experiment, the first 0^+ excited state was not discernable from the background. For

this reason they were only able to set upper limits on the relative strength for transfer to the excited states. They inferred from the background level in the region of the excited state in the TOF spectra that the strength for transfer to the 0^+ excited is less than 6% for ^{76}Se and less than 19% for ^{78}Se relative to transfer to the respective ground states in these nuclei.

Table 8.1 also compares the measured 0^+ excited state strengths to those predicted by the two-nucleon transfer code FRESCO. Although the absolute values generally do not agree, the variance in the data with beam energy matches the predicted variation (i.e., for a given target, the ratio of measured to predicted 0^+ excited state strength is constant within errors for different beam energies). The smaller measured 0^+ excited strengths for the ^{76}Ge target relative to the prediction may be due to the large uncertainty introduced from the ^{74}Ge contamination.

Table 8.1: 0^+ excited state strength as a fraction of 0^+ ground state strength at 0° for the Ge(^3He,n)Se reaction. The ratios measured in this experiment are compared with the predicted ratios from the DWBA code FRESCO.

		0^+ excited state strength		
Residual Nucleus	^{3}He Beam Energy	measured	FRESCO	measured:FRESCO
^{76}Se	15 MeV	0.111 ± 0.028	0.034	3.286 ± 0.829
^{76}Se	21 MeV	0.048 ± 0.011	0.018	2.695 ± 0.618
^{78}Se	15 MeV	0.089 ± 0.026	0.073	1.219 ± 0.356
^{78}Se	21 MeV	0.129 ± 0.016	0.078	1.645 ± 0.204

Section 8.2: Examination of the Two-proton Transfer Mechanism

The transfer mechanism for the two-proton drop-off reaction was examined by comparing the measured angular differential cross section data from this work to DWBA calculations that were made using the code FRESCO (Thompson [1988]). As discussed in chapter 2, DWBA calculations of two-nucleon transfer cross sections include contributions from simultaneous (historically referred to as direct) and sequential processes. Data are compared to DWBA calculations in Figs. 8.1, 8.2, 8.3, and 8.4. The plots illustrate the calculated and measured cross sections for the targets and ^{3}He beam energies used in this work. In all cases

the calculated contribution from the direct transfer process underpredicts the data. The total calculated cross section (i.e., direct plus sequential processes) predicts values substantially larger than the data.

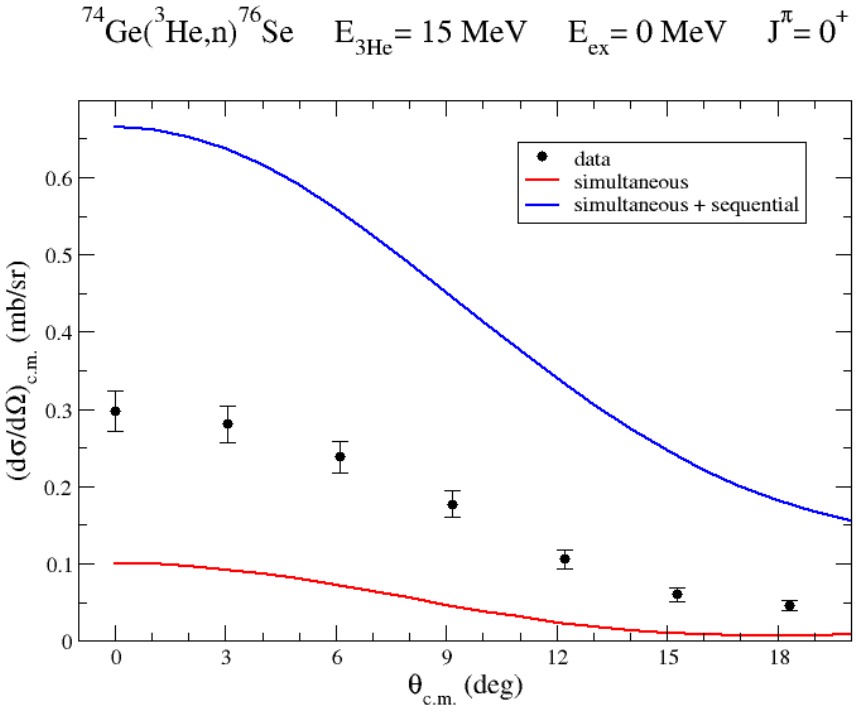

Figure 8.1: A plot of the measured and calculated differential cross section for the ^{74}Ge(^{3}He,n)^{76}Se reaction at $E_{3He} = 15$ MeV. Errors on data points are statistical only.

Both the direct and total calculations were normalized to fit the data. The DWBA calculations were normalized to the data to minimize χ^2 for each target and energy as shown in Figs. 8.5, 8.6, 8.7, and 8.8. In all cases, the shape of the data curve matches roughly to the shape of the calculated curves. However, in all cases the normalized direct-only curves have a steeper slope than the data curves. Except for ^{76}Ge(^{3}He,n)^{78}Se at 15 MeV, all of the normalized total curves have a shallower slope than the data curves. These shape variations, combined with magnitudes of the unscaled calculations relative to the data, suggests the importance of the sequential process is overestimated in the calculations. This overestimation may originate from the assumed strength of pair correlations (Potel et al. [2013]).

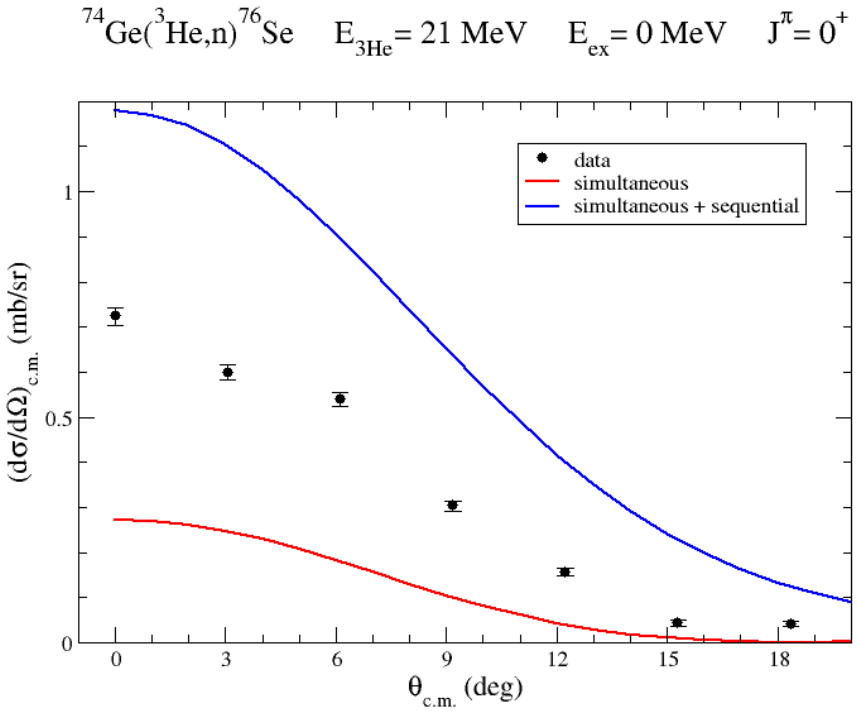

Figure 8.2: A plot of the measured and calculated differential cross section for the ^{74}Ge(^{3}He,n)^{76}Se reaction at E_{3He} = 21 MeV. Errors on data points are statistical only.

Section 8.3: Summary

In this experiment, new angular distribution cross-section data for the ^{74}Ge(^{3}He,n)^{76}Se and ^{76}Ge(^{3}He,n)^{78}Se reactions at 15 MeV and 21 MeV incident ^{3}He beam energies were measured. The measured cross sections covered the neutron emission angles from 0° to 18° in the laboratory. These data were used to evaluate the validity of the BCS approximation in QRPA calculations of nuclear matrix elements for $0\nu\beta\beta$ of ^{76}Ge and to assess the transfer processes in the two-proton drop-off reaction for the nuclei studied. Based on the observed relative strength for transfer to the first 0^{+} excited state, the data from this work confirms the validity of the BCS approximation for this nucleus. In addition, the magnitude and shape of the measured angular distributions suggest that contribution of the sequential process, which is an indicator of long-range nucleon-nucleon correlations, is overpredicted by the DWBA code FRESCO.

The data collected for this project are expected to improve calculations of $M^{0\nu}$, and, if

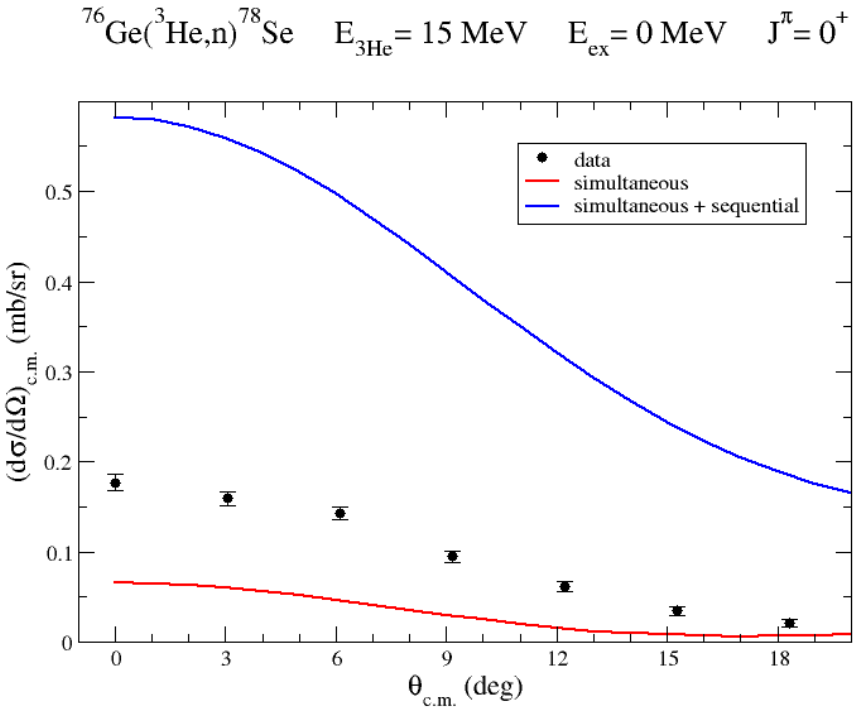

Figure 8.3: A plot of the measured and calculated differential cross section for the ^{76}Ge(^{3}He,n)^{78}Se reaction at $E_{3He} = 15$ MeV. Errors on data points are statistical only.

$0\nu\beta\beta$ is observed, calculations of the neutrino mass. These data also add to our knowledge of two-nucleon transfer reactions. Furthermore, the laboratory systems and techniques developed for this project will provide research opportunities for scientists in the future. It is hoped that this document provides a clear and thorough explanation of those systems and techniques.

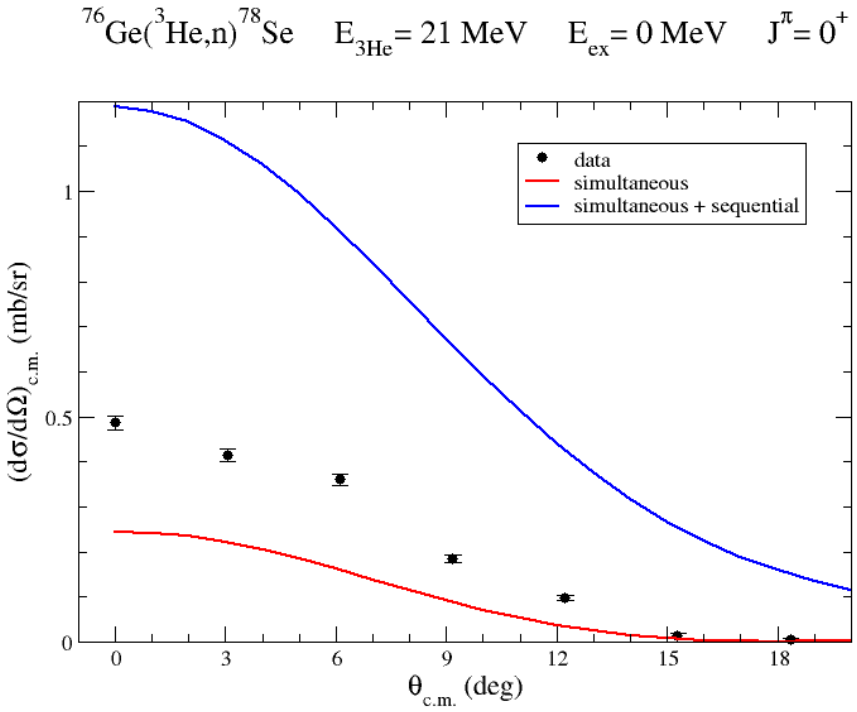

Figure 8.4: A plot of the measured and calculated differential cross section for the ^{76}Ge(^{3}He,n)^{78}Se reaction at $E_{3He} = 21$ MeV. Errors on data points are statistical only.

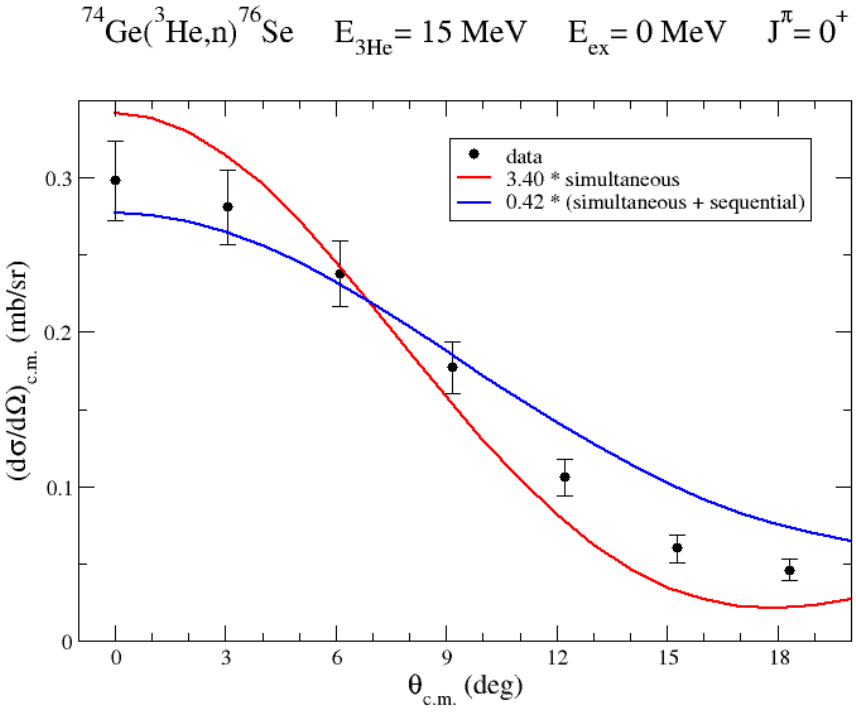

Figure 8.5: A plot of the measured and calculated differential cross section for the ^{74}Ge(^{3}He,n)^{76}Se reaction at $E_{3He} = 15$ MeV. Calculated cross sections have been normalized to fit the data. Normalization factors are given in the legends. Errors on data points are statistical only.

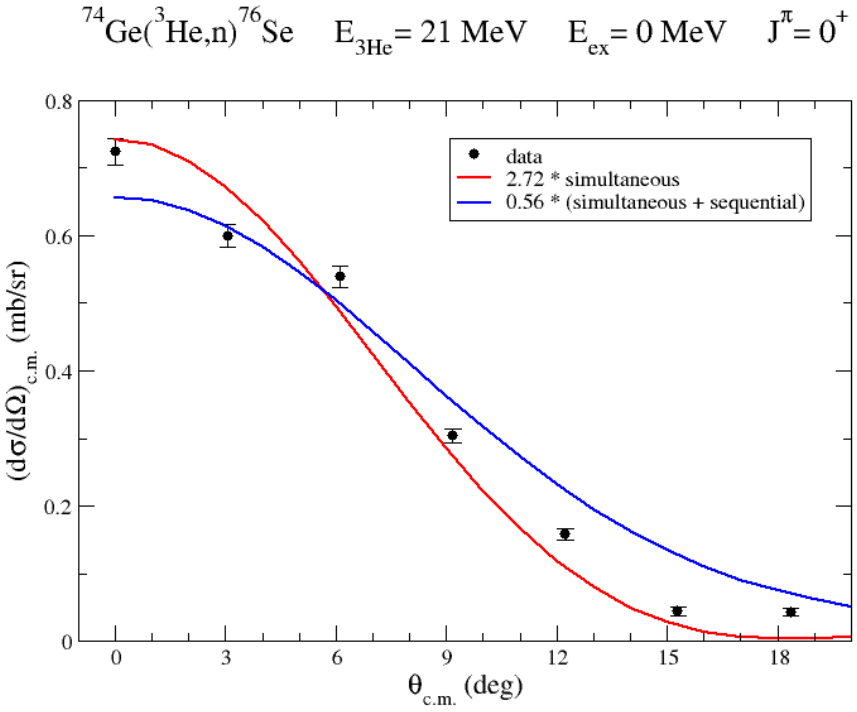

Figure 8.6: A plot of the measured and calculated differential cross section for the ^{74}Ge(^{3}He,n)^{76}Se reaction at $E_{3He} = 21$ MeV. Calculated cross sections have been normalized to fit the data. Normalization factors are given in the legends. Errors on data points are statistical only.

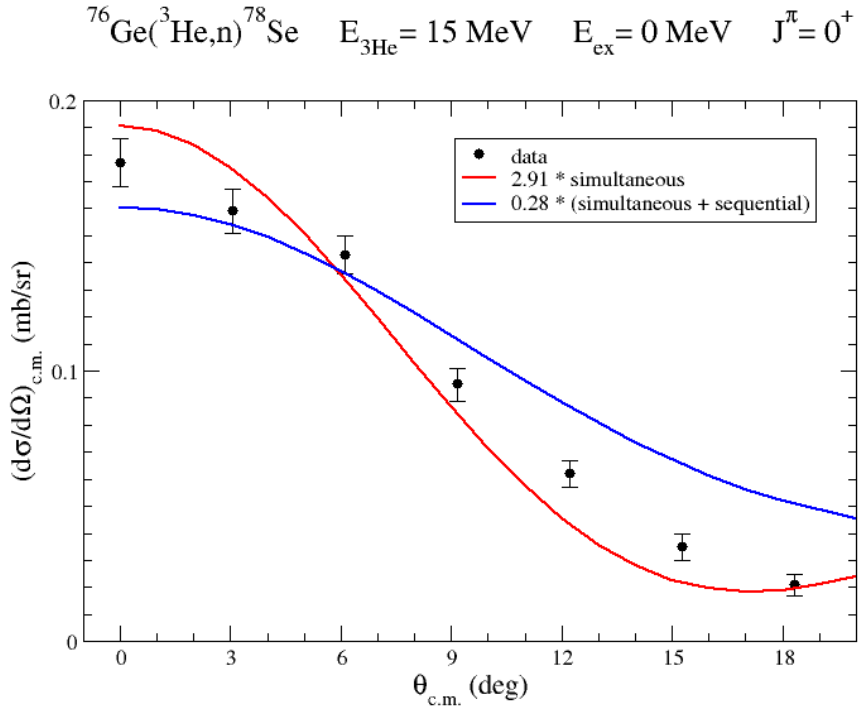

Figure 8.7: A plot of the measured and calculated differential cross section for the ^{76}Ge(^{3}He,n)^{78}Se reaction at $E_{3He} = 15$ MeV. Calculated cross sections have been normalized to fit the data. Normalization factors are given in the legends. Errors on data points are statistical only.

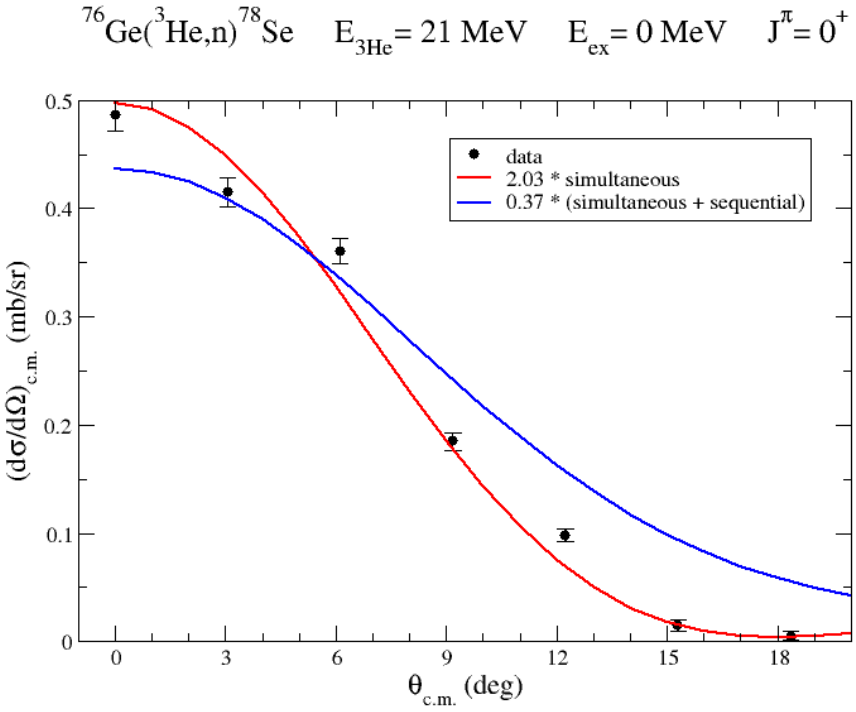

Figure 8.8: A plot of the measured and calculated differential cross section for the ^{76}Ge(^{3}He,n)^{78}Se reaction at $E_{3He} = 21$ MeV. Calculated cross sections have been normalized to fit the data. Normalization factors are given in the legends. Errors on data points are statistical only.

APPENDIX A: Research Infrastructure Improvements

This experiment required the construction and installation of several major systems:

- Two chopper plate assemblies were fabricated, then installed on the HIS. A short beamline was constructed off of the 59-degree beamline and used to optimize the beam pulsing capabilities of the HIS. Further research and development was conducted on the HIS using the new 70-degree beamline.
- A gas recovery system for ^{3}He was designed and installed on the HIS. The performance of the recovery system was characterized.
- A new beamline on the 70° port of the 20-70 magnet vacuum chamber was designed, surveyed, installed, and commissioned. A large "window" for neutrons was created in the shielding wall between the target chamber and detectors. Existing water and electrical lines were re-routed.
- An existing target chamber was modified for the needs of this experiment then installed on the end of the new beamline.
- Detector mounts were designed, fabricated, and then installed at surveyed locations around the target chamber.
- A dedicated DAQ was assembled to process and collect data from the array of detectors used in this experient and two new cable runs were made between the control room and experimental areas.
- Research was conducted to optimize the target evaporation procedure. Twelve isotopically enriched targets were fabricated and characterized. A leak-tight target storage box was designed and fabricated to store the targets in an argon atmosphere.

During the course of this project, several efforts met with failure and are qualitatively listed here in an effort to prevent repeated mistakes.

- An attempt was made to increase the maximum beam current output of the HIS by biasing the ground electrode. Voltages up to -5 kVDC on the ground electrode were not observed to change the beam current significantly.

- In an effort to increase the quantity of charge per beam pulse and achieve narrower beam pulse timing, the bias on the attachment electrode in the HIS was varied with a linear ramp circuit. This attempt to "pre-bunch" the beam caused increased sparking between the HIS electrodes, wider beam dispersion from the NIS magnet, and wider beam pulse timing.

- Beamstops and beam limiting apertures were initially lined with lead pieces cut from a ⅛" thick sheet. Because lead has a low thermal conductivity, beam-induced heating melted several of these pieces. Evaporating a thin coating of lead onto a tantalum or steel surface, while much more time-consuming to prepare, was found to disperse a greater amount of beam power without melting.

Several improvements might be made to the 70-degree beamline and the ^{3}He recovery system:

- Replacing the backing pumps on the 70-degree beamline vacuum system with oil-free scroll pumps might reduce carbon contamination on targets.

- Numerous improvements could be made to the ^{3}He recovery system and are listed in chapter 6.

- The maximum attainable HIS beam current and continual beam interruptions because of instabilities in the HIS were the primary factors limiting the counting rate and the energy resolution in this experiment. Several potential improvements to the helium souce are listed:

  - Sparking between electrodes, primarily on the oil cooling lines, caused severe source instability. Replacing the oil lines, possibly with plastic tubing might

alleviate this problem (plastic tubing would require an additional dedicated lead to bias each electrode).

- Misalignment of the duoplasmatron, source electrodes, and chopping plates may cause decreased beam output. Alignment would require sighting with an optical level through the NIS magnet.
- Oil contamination inside the source box might be related to sparking and beam degradation. Further investigation of the source of contamination is warranted.
- A thermocouple thermometer installed on the sodium oven would aid in optimizing the charge exchange process.
- The duoplasmatron filament burned out several times during this project. Before a burnout, beam current from the HIS was always observed to increase by a factor of two or more. A thinner filament or a filament made from a material other than tungsten might increase beam current.

APPENDIX B: Operational Procedures for the ^{3}He Recovery System

This appendix contains procedures for using the ^{3}He recirculation system. Included in this appendix is a procedure for evacuating and starting the system from shutdown, a procedure for evacuating and purging the system during a run, a procedure to add gas during a run and the procedure for shutting off the recirculation system.

Starting from shutdown

This is the procedure for starting the recirculation system from shutdown. This procedure assumes that the helium-ion source (HIS) has already been started using ^{4}He. It is safe practice to start with ^{4}He gas to make sure the source is operating normally before loading the more expensive ^{3}He gas into the system. At the start of the procedure valves V1, V2, V4, V6 and V19 should be open. All other valves should be closed.

1. Start the compressor and Pfeiffer rotary vane pump.
2. Open V9, V13 and V17.
3. Start the mechanical pump.
4. Open V20, V10 and the ball valve between those two valves. The pressure indicated in G1 should drop to 0.
5. Allow system to pump for at least 15 minutes to make sure the manifold is competely cleared.
6. Close V10 and the ball valve.
7. Make sure that V12 and regulator R2 are closed.
8. Crack the valve on top of the ^{3}He bottle and then close it.

9. Open V12.

10. Open R2 and note the increase in pressure in G1.

11. Close V12 and R2. If the pressure indicated at G1 is within the desired range (typically > 0.4 psia) proceed to the next step. If not, repeat steps 7-11 until desired pressure is reached.

12. Fill the LN2 dewar.

13. Close V1.

14. Open the ball valve leading to the upper manifold and V18. The flow rate in the flow meter should drop.

15. As soon as the flow rate drops to 0 sccm, close V19, V18, the ball valve and V20.

16. Shut off the mechanical pump.

17. Open V3. Given that the ^{3}He recirculation system operates at much lower pressure than the ^{4}He gas bottle, it will probably be necessary to open the source gas needle valve from the control room. Adjust the gas flow using the rocker switch on the HIS control panel until the rate is about 0.5 sccm.

18. Check the vacuum at the inlet to the rotary vane pump. If vacuum is < 100 mTorr then, close V6 and open V8. Make sure that the vacuum in the source box is still good.

Purge and reload

During a run it may be necessary to purge the recirculation system and reload it with fresh gas. This procedure assumes that the HIS is running with ^{3}He gas. The outline of the procedure is to switch the source gas from ^{3}He to ^{4}He to make sure that beam is being extracted while the recirculation manifold is evacuated. The recirculation system is then

isolated from the source and evacuated. Once the recirculation system is evacuated it is reloaded from the ^{3}He bottle. The source gas is then switched back from ^{4}He to ^{3}He. At the start of the procedure valves V2, V3, V4, V8, V9, V13 and V17 should be open. The remaining valves should be closed.

1. Close V8 and open V6.
2. Close V3.
3. Shut the source gas needle valve using the rocker switch in the HIS control panel until the flow drops to 0 sccm.
4. Open the ^{4}He gas bottle and valves V1 and V19. If necessary, adjust the source gas needle valve until the flow is between 0.6 and 0.8 sccm.
5. Start the mechanical pump.
6. Open V20, V10 and the ball valve between those two valves. The pressure indicated in G1 should drop to 0.
7. Allow system to pump for at least 15 minutes to make sure the manifold is competely cleared.
8. Close V10 and the ball valve.
9. Make sure that V12 and regulator R2 are closed.
10. Crack the valve on top of the ^{3}He bottle and then close it.
11. Open V12.
12. Open R2 and note the increase in pressure in G1.
13. Close V12 and R2. If the pressure indicated at G1 is within the desired range (typically > 0.4 psia) proceed to the next step. If not, repeat steps 7-11 until desired pressure is reached.

14. Close V1.

15. Open the ball valve leading to the upper manifold and V18. The flow rate in the flow meter should drop.

16. As soon as the flow rate drops to 0 sccm, close V19, V18, the ball valve and V20.

17. Shut off the mechanical pump.

18. Open V3. Given that the ^{3}He recirculation system operates at much lower pressure than the ^{4}He gas bottle, it will probably be necessary to open the source gas needle valve from the control room. Adjust the gas flow using the rocker switch on the HIS control panel until the rate is about 0.5 sccm.

19. Check the vacuum at the inlet to the rotary vane pump. If vacuum is < 100 mTorr then, close V6 and open V8. Make sure that the vacuum in the source box is still good.

Refill while running

This is the procedure to add gas to the system while running. At the start of this procedure valves V2, V3, V4, V8, V9, V13 and V17 should be open. The remaining valves should be closed.

1. Make sure that V12 and regulator R2 are closed.

2. Crack the valve on top of the ^{3}He bottle and then close it.

3. Open V12.

4. Open R2 and note the increase in pressure in G1.

5. Close V12 and R2. If the pressure indicated at G1 is not within the desired range (typically > 0.4 psia) repeat steps 7-11 until desired pressure is reached.

Shutdown

This is the procedure to shut down the HIS when running ^{3}He. At the start of the procedure valves V2, V3, V4, V8, V9, V13 and V17 should be open. The remaining valves should be closed.

1. Close V8 and open V6.
2. Close V3.
3. Shut the source gas needle valve using the rocker switch in the HIS control panel until the flow drops to 0 sccm.
4. Open the ^{4}He gas bottle and valves V1 and V19. If necessary, adjust the source gas needle valve until the flow is between 0.6 and 0.8 sccm.
5. Close V9, V13 and V17.
6. Turn off the Pfeiffer rotary vane pump and the compressor.
7. Follow the HIS shutdown procedure as described in the source manual.

APPENDIX C: ROOT TOF Simulation Code

```
// eres_sim.C
// Cint or Compiled
// 3/12 by D Ticehurst
// to use strengths found in Alford 1979
// in simulating Ge(3He,n)Se
// ---------------------------------------------------

#include <Riostream.h>
#include <TCanvas.h>
#include <TH1F.h> // needed to make 1D HIST
#include <TH2F.h> // needed to make 2D HIST
#include <TF1.h>
#include <TRandom3.h> //for good stats
#include <TStopwatch.h>
#include <TMath.h>
#include <TPaveText.h>
#include <TString.h>
#include <TStyle.h>
// my Objects
TCanvas *SimpleCanvas1;
TCanvas *SimpleCanvas2;
TH1F *Hist1;
TH1F *Hist2;
TH1F *Hist3;
TH1F *Hist4;
TH1F *Hist5;
TH1F *Hist6;
TH1F *Hist7;
TH1F *Hist8;
TH1F *myhistarray[10];
```

```
TPaveText *MyText;

//returns def if user just hits enter
Float_t get_num(Float_t def){
  Float_t temp = def;

  std::string input;
  std::getline(std::cin, input);
  if(!input.empty()){
     temp = atof(input.c_str());
  }
  return temp;
}
//
//calculates energy of emitted neutron = 3he energy + Q-value - random energy
    loss
Float_t calc_n_en(Float_t E_init, Float_t E_loss, Float_t Q){
  TRandom3 random_1;
  random_1.SetSeed(0);

  Float_t lost = random_1.Uniform(0, E_loss);
  Float_t temp2 = E_init + Q - lost;

  return temp2;
}
//
//convert neutron energy in MeV into neutron velocity in cm/ns
Float_t e2v(Float_t e){
  Float_t v = 29.9792458 * sqrt(1 - pow(1 / (1 + (e / 939.565560)),2));
  return v;
}
//
```

```
//convert TOF to neutron energy using average path length
Float_t t2e(Float_t t, Float_t path){
  Float_t v = path / t;
  Float_t e = 939.565560 * (sqrt(1 / (1 - pow(v / 29.9792458,2))) - 1);
  return e;
}
//
// some input data
  Int_t num_ev = 1000000;

  //some energy loss values
  //
  // nuclide  energy  eloss thickness
  // 74 Ge      15    0.172    1
  //            17    0.157    1
  //            20    0.140    1
  //            25    0.119    1
  //            10    0.459    2
  //            13    0.382    2
  //            15    0.345    2
  //            17    0.315    2
  //            20    0.280    2
  //            25    0.238    2
  // 76 Ge      15    0.167    1
  //            17    0.153    1
  //            20    0.136    1
  //            25    0.116    1
  //            10    0.447    2
  //            13    0.372    2
  //            15    0.336    2
  //            17    0.307    2
  //            20    0.273    2
  //            25    0.231    2
```

```
// Q-values and energy loss for 74Ge, 76Ge, and 130Te (Te using 1.10 mg/cm2)
Float_t dat[3][2] = {{8.69, 0.117}, {10.67, 0.114}, {8.79, 0.104}};

// level J-pi, energy, and strength at 0deg for 132Xe from Alford
// 0+ 0.00 1.00
// 0+ 1.85 0.38
// 2+ 1.85 0.09 (14 deg)
// 0+ 2.49 0.24
// 2+ 2.49 0.16 (14 deg)
// (note that there seem to be a number of non-0+ level missing,
// such as 2+ levels 0.67 and 1.30 MeV
// I will assume only 0+ levels appear in a TOF spectra a 0deg
// and non-GS 0+ levels appear at 0.2 GS strength
// Further assume only 2+ levels appear at ~14deg with roughly equal
 strengths

// Non-GS level energies, J-pi, and strengths (relative to GS) for 76Se, 78
 Se, and 132Xe
Float_t levels[3][5][3] = {{{0.559, 2, 1}, {1.122, 0, 0.1}, {1.216, 2, 0.1},
  {1.788, 2, 1}, {-1, -1, -1}},
        {{0.614, 2, 1}, {1.309, 2, 1}, {1.499, 0, 0.2}, {1.759, 0, 0.2},
 {1.996, 2, 1}},
        {{1.85, 0, 0.38}, {1.85, 2, 0.09}, {2.49, 0, 0.24}, {2.49, 2,
 0.16}, {-1, -1, -1}}};


//3He beam energy, MeV
Float_t beamE = 21.0;
//neutron detector thickness, cm
Float_t det_thick = 5;
//FWHM of time resolution from electronics, beam, etc. ns
Float_t base_res = 1.5;
```

```
  //flight path, cm
  Float_t flight_path = 1300;
  //position in detector neutron interacts, neutron energy, neutron velocity,
   and tof
  Float_t det_pos = 0, nen = 0, nvel = 0, tof = 0;

  Int_t choice = 0;

//the main function
void eres_sim(){
  cout << "Choose target material:" << endl
       << "0 - 74Ge (Q = 8.69 MeV, " << dat[0][1] << " MeV energy loss)" <<
   endl
       << "1 - 76Ge (Q = 10.67 MeV, " << dat[1][1] << " MeV energy loss)" <<
   endl
       << "2 - 130Te (Q = 8.79 MeV, " << dat[2][1] << " MeV nergy loss, Alford
    data)" << endl;
  choice = (Int_t)get_num((Float_t)choice);

  cout << "Beam energy? (Default: " << beamE << " MeV)";
  beamE = (Int_t)get_num((Float_t)beamE);

  cout << "number of events going to GS? (Default: " << num_ev << ")";
  num_ev = (Int_t)get_num((Float_t)num_ev);

  cout << "target-detector distance? (Default = " << flight_path << " cm)";
  flight_path = get_num(flight_path);

  cout << "base time resolution? (Default FWHM = " << base_res << " ns)";
  base_res = get_num(base_res);

  cout << "detector thickness? (Default = " << det_thick << " cm)";
  det_thick = get_num(det_thick);
```

```
cout << "Would you like to assign a different energy loss? (hit enter if no)
  ";
dat[choice][1] = get_num(dat[choice][1]);

Float_t sigma = base_res / 2.3548;

Float_t avg_path = flight_path + (det_thick / 2);

Int_t width=1000;
Int_t height = 1000;
Int_t whereX=100;
Int_t whereY=10;

// some variables to make a Histogram

Int_t bins=1000;
Float_t low_t=0;
Float_t hi_t=0;
Float_t low_E, hi_E;
//get min/max possible neutron TOF and TOF calculated energy for bin range
low_t = 0.95 * ((flight_path / e2v((beamE + dat[choice][0]))) + (det_thick /
   29.9792458));

hi_t = 1.05 * (flight_path + det_thick) / e2v((beamE + dat[choice][0] - dat[
  choice][1]));

low_E = t2e((hi_t + (2 * base_res)), avg_path);
hi_E = 1.2 * (beamE + dat[choice][0]);

printf("low_t = %f, hi_t = %f, low_E = %f, hi_E = %f\n", low_t, hi_t, low_E,
   hi_E);
```

```
//elapsed time
Float_t realt;

//number of events to consider
Int_t numev = num_ev;
Int_t frac = Int_t(numev/10);

Hist1 = new TH1F("0 deg energy composite","0 deg energy composite",bins,
 low_E,hi_E);
Hist2 = new TH1F("14 deg energy composite","14 deg energy composite",bins,
 low_E,hi_E);
Hist3 = new TH1F("Hist3","TOFex1",bins,low_t,hi_t);
Hist4 = new TH1F("Hist4","TOFex2",bins,low_t,hi_t);
Hist5 = new TH1F("Hist5","TOFex3",bins,low_t,hi_t);
Hist6 = new TH1F("Hist6","TOFex4",bins,low_t,hi_t);
Hist7 = new TH1F("Hist7","TOFex5",bins,low_t,hi_t);
Hist8 = new TH1F("Hist7","",bins,low_t,hi_t); //TOF composite at 14deg


//set up an array of histos to store composite and excited state data
  Char_t *histname = new char[10];
  myhistarray[0]=new TH1F("0 deg composite","0 deg composite",bins, low_t,
 hi_t);
  myhistarray[1]=new TH1F("14 deg composite","14 deg composite",bins, low_t,
  hi_t);
  for (Int_t iii=2;iii<10; iii++) {
  sprintf(histname, "TOF%i",iii-2);
  myhistarray[iii]=new TH1F(histname, histname, bins, low_t, hi_t);

  myhistarray[iii]->GetXaxis()->SetTitle("TOF (ns)");
  myhistarray[iii]->GetYaxis()->SetTitle("Counts");
  myhistarray[iii]->GetYaxis()->SetTitleOffset(1.3);
  }
```

```
Hist1->GetXaxis()->SetTitle("Neutron Energy (MeV)");
Hist1->GetYaxis()->SetTitle("Counts");
Hist1->GetYaxis()->SetTitleOffset(1.3);

Hist2->GetXaxis()->SetTitle("Neutron Energy (MeV)");
Hist2->GetYaxis()->SetTitle("counts");
Hist2->GetYaxis()->SetTitleOffset(1.3);

TStopwatch sw;
char temp[10], ltext[50];

TRandom3 random;
random.SetSeed(0);

sw.Start(1);
Int_t i = 0;
for(i = 0; i < numev; i++) {
  if(i%frac == 0 || i == numev-1)
    {
sw.Stop();
realt = sw.RealTime();
realt = (Float_t)frac / realt;
sprintf(temp,"%4.2f", (Double_t)i / (Double_t)numev *100.);
cout << "\r "<< temp << " % completed,  " << realt << " Hz";
cout.flush();
sw.Start();
    }

  //random location of detector interaction
  det_pos = random.Uniform(0, det_thick);
  //neutron energy, random energy loss in target
  nen = beamE + dat[choice][0] - random.Uniform(0, dat[choice][1]);
```

```
  nvel = e2v(nen);
  tof = ((flight_path + det_pos) / nvel) + ((det_thick - det_pos) /
 29.9792458);
  tof += random.Gaus(0, sigma);

  myhistarray[0]->Fill(tof);
  myhistarray[2]->Fill(tof);

  nen = t2e(tof, avg_path);
  Hist1->Fill(nen);

  //gamma background
  tof = ((flight_path + det_thick) / 29.9792458);
  tof += random.Gaus(0, sigma);
  myhistarray[0]->Fill(tof);
  myhistarray[1]->Fill(tof);

  //fill excited state histos
  for(Int_t j = 0; j < 5; j++){

    nen = beamE + dat[choice][0] - levels[choice][j][0] - random.Uniform(0,
  dat[choice][1]);
    nvel = e2v(nen);
    tof = ((flight_path + det_pos) / nvel) + ((det_thick - det_pos) /
 29.9792458);
    tof += random.Gaus(0, sigma);

//apply strength to excited 0+ states
if(levels[choice][j][1] == 0){
  if(i < (Int_t)(levels[choice][j][2]*numev)){
    myhistarray[j+3]->Fill(tof);
    myhistarray[0]->Fill(tof);
    nen = t2e(tof, avg_path);
```

```
    Hist1->Fill(nen);
  }
}
else if(levels[choice][j][1] != -1 && i < (Int_t)(levels[choice][j][2]*numev
 )){
  myhistarray[j+3]->Fill(tof);
  myhistarray[1]->Fill(tof);
  nen = t2e(tof, avg_path);
  Hist2->Fill(nen);
}

  }

}
cout << "got to end of loop" << endl;
sw.Stop();

MyText = new TPaveText(0.6,0.5,0.95,0.8,"NDC");
sprintf(ltext, "3He beam energy = %.1f MeV", beamE);
MyText->AddText(ltext);
sprintf(ltext, "Q-value = %.2f MeV", dat[choice][0]);
MyText->AddText(ltext);
sprintf(ltext, "flight path = %.0f cm", flight_path);
MyText->AddText(ltext);
sprintf(ltext, "detector thickness = %.2f cm", det_thick);
MyText->AddText(ltext);
sprintf(ltext, "Max energy loss in target = %.3f MeV", dat[choice][1]);
MyText->AddText(ltext);
sprintf(ltext, "base time resolution FWHM = %.1f ns", base_res);
MyText->AddText(ltext);

cout << "made table" << endl;
```

```
SimpleCanvas1 = new TCanvas("SimpleCanvas1","Simulated TOF spectra",
            whereX,whereY,width,height);
SimpleCanvas1->Divide(2,2);
gStyle->SetOptStat(0);
SimpleCanvas1->ToggleEventStatus();


SimpleCanvas2 = new TCanvas("SimpleCanvas2","Simulated neutron E spectra",
            whereX + 20,whereY + 20,width,height/2);
SimpleCanvas2->Divide(2,1);
SimpleCanvas2->ToggleEventStatus();

cout << "made canvases" << endl;

// Draw the  HISTOs
Int_t k = 0, count = 0;


SimpleCanvas1->cd(1);

myhistarray[2]->Draw();
MyText->Draw();

SimpleCanvas1->cd(2);

myhistarray[0]->SetLineWidth(2);
myhistarray[0]->SetLineColor(2);

myhistarray[0]->Draw();
myhistarray[2]->Draw("SAME");

SimpleCanvas1->cd(3);
```

```
  SimpleCanvas1->cd(4);
  myhistarray[1]->SetLineWidth(2);
  myhistarray[1]->SetLineColor(2);

  myhistarray[1]->Draw();

  for(k = 0; k < 5; k++){
    if(levels[choice][k][1] == 0){
        SimpleCanvas1->cd(1);
  myhistarray[k+3]->Draw("SAME");
  SimpleCanvas1->cd(2);
  myhistarray[k+3]->Draw("SAME");
    }
    else{
      if(count == 0) sprintf(histname, "");
      else sprintf(histname, "SAME");
      SimpleCanvas1->cd(3);
      myhistarray[k+3]->Draw(histname);
      SimpleCanvas1->cd(4);
      myhistarray[k+3]->Draw("SAME");
      count++;
    }
  }

  SimpleCanvas2->cd(1);
  Hist1->Draw();
  SimpleCanvas2->cd(2);
  Hist2->Draw();
  // Updates the Canvas with the changes
  SimpleCanvas1->Modified();
  SimpleCanvas2->Modified();

}
```

APPENDIX D: Tables of Cable Runs and Detector Patching

Table 2: New cable runs made for this project

Cable Type	Number of Cables
Cables run from target chamber area to Control Room	
RG-62 (93Ω)	15
RG-58 (50Ω)	5
RG-213/U (low-loss 50Ω RG-8 equivalent)	2
RG-59 (high voltage with SHV connectors)	5
Cables run from Target Room 1 to Control Room	
RG-213/U (low-loss 50Ω RG-8 equivalent)	21

Table 3: Cabling between target chamber area and Control Room

Device	Cable Type
ΔE detector timing signal	RG-58 (50-Ω)
ΔE detector PH signal	RG-62 (93Ω)
E detector PH signal	RG-62 (93Ω)
CsF detector anode signal	RG-58 (50Ω)
Micrometer aperture slits	RG-62 (93Ω)
Beam pickoff	RG-8 equivalent low-loss (50Ω)
Beamstop before target chamber	RG-62 (93Ω)
Suppressor grid high voltage	RG-62 (93Ω)
Beamstop behind target	RG-62 (93Ω))

Table 4: Detector Cabling Map

detector #	Angle, position	HV supply chan	HV	cable #	MPD-4 module #	MPD-4 chan #	PH ADC chan	PSD ADC chan	Scaler chan
21	0 deg, top	0	-1380	1	1	1	1	2	26
18	0 deg, middle	1	-1375	2	1	2	3	4	26
15	0 deg, bottom	2	-1375	3	1	3	5	6	26
7	3 deg, top	3	-1505	4	1	4	7	8	27
5	3 deg, middle	4	-1775	5	2	1	9	10	27
11	3 deg, bottom	5	-1485	6	2	2	11	12	27
20	6 deg, top	6	-1350	7	2	3	13	14	28
22	6 deg, middle	7	-1400	8	2	4	15	16	28
16	6 deg, bottom	8	-1365	9	3	1	17	18	28
10	9 deg, top	9	-1630	10	3	2	19	20	29
13	9 deg, middle	10	-1335	11	3	3	21	22	29
2	9 deg, bottom	11	-1745	12	3	4	23	24	29
19	12 deg, top	12	-1370	13	4	1	25	26	30
14	12 deg, middle	13	-1505	14	4	2	27	28	30
23	12 deg, bottom	14	-1480	15	4	3	29	30	30
1	15 deg, top	15	-1785	16	4	4	31	32	31
12	15 deg, middle	16	-1515	17	5	1	33	34	31
4	15 deg, bottom	17	-1500	18	5	2	35	36	31
3	18 deg, top	18	-1715	19	5	3	37	38	32
6	18 deg, middle	19	-1680	20	5	4	39	40	32
9	18 deg, bottom	20	-1690	21	6	1	41	42	32
CsF	below 70 R chamber			50ohm #2 to #21 opposite side of room	6	2	43		24
CP E E	inside 70 R chamber			93ohm #11 to /3 attenuator to 572 amp to #26 opposite side of room			44		
CP E dt	inside 70 R chamber			50ohm #1					
CP de E	inside 70 R chamber			93ohm #13 to 572 amp to #22 opposite side of room			45		
CP de dt	inside 70 R chamber			50ohm #3 to TFA to discriminator to 200 ns delay to #25 opposite side of room					25

APPENDIX E: Tables of Neutron Detector Calibration Data

Table 5: Detector Cabling Map

HV supply channel	Angle, position	HV	pedestal	Cs edge	threshold	threshold (fraction Cs)
0	0 deg, top	-1330	126	247	194	0.56
1	0 deg, middle	-1325	154	261	162	0.07
2	0 deg, bottom	-1325	142	254	156	0.13
3	3 deg, top	-1455	160	282	220	0.49
4	3 deg, middle	-1725	138	277	220	0.59
5	3 deg, bottom	-1435	138	301	254	0.71
6	6 deg, top	-1300	151	298	232	0.55
7	6 deg, middle	-1350	162	299	224	0.45
8	6 deg, bottom	-1315	160			1.00
9	9 deg, top	-1580	150	338	273	0.65
10	9 deg, middle	-1285	286	462	359	0.41
11	9 deg, bottom	-1695	174	386	292	0.56
12	12 deg, top	-1320	170	285	208	0.33
13	12 deg, middle	-1455	170	298	216	0.36
14	12 deg, bottom	-1430	174	303	207	0.26
15	15 deg, top	-1735	190			1.00
16	15 deg, middle	-1465	94	234	157	0.45
17	15 deg, bottom	-1450	110	236	156	0.37
18	18 deg, top	-1665	122	260	200	0.57
19	18 deg, middle	-1630	118	261	189	0.50
20	18 deg, bottom	-1640	110	269	195	0.53

APPENDIX F: Checklist for Setting Up the 70° beamline

Experiment: _____

Dates: _____

- ☐ Hook up buncher and choppers
- ☐ Set buncher length: _____ for _____ keV _____ particles
- ☐ Tune buncher and main chopper LC circuits
- ☐ Patch Beamline Devices
- ☐ Control slits
- ☐ 20-70 cup select knob (located on 20-70) to 70 degrees
- ☐ 20-70 steerer → station 3, 3A →power supply 5-6
- ☐ Downstream steerer → station 3, 3A → power supply 7-8
- ☐ Quad → station 2 QA/Q1 → power supply Q4C
- ☐ Upstream slits → 93 ohm #9 →Keithley 8
- ☐ Pickoff → amplifiers (plug these in) → low loss #1
- ☐ Downstream slit → 93 ohm #10 →Keithley 9
- ☐ Downstream beamstop → 93 ohm #3 →Keithley 10
- ☐ Beam dump → 93 ohm #1 → BCI (10E-_____ C/pulse)
- ☐ Suppressor → 93 ohm #2 → HV supply in control room (turn on bias +175V)
- ☐ Check HE Quad polarity (should be in normal polarity)
- ☐ Hook up post 20-70 beam scanner (may be hooked to 20 deg leg)
- ☐ Remove poly blocks from TR1 wall
- ☐ Place targets in Chamber:

	Material	Backing Identifier	Thickness (mg/cm^2)	Q-value
Top				
Middle				
Bottom				

☐ Bias Detectors

☐ CsF +1500V

☐ Si ΔE +10.0V $\sim$0.06 μA

☐ Si E -500V $\sim$1.48 μA (turn up slowly, may overload when recently biased)

☐ Check neutron detector biases (listed in daq_info/detector_map.xlsx)

☐ Ensure DAQ operation

☐ Check neutron detector gains and set software thresholds with Cs source (name and location of excel file: _____)

☐ Ensure over range bit is set in nme.crl prestart (c792overrange(0,1))

☐ Check PSD cuts with AmBe source

☐ Check scaler functionality

☐ Set ADC thresholds in crl_3610.h to eliminate pedestals: _____ x 16 = _____

☐ Set 20-70 magnet

☐ Calculate beam energy (_____ MeV) given energy loss (_____keV) in target ☐ Calculate 20-70 magnet setting: _____ mT

☐ Open tube valves on 70 degree line

☐ Set rf delay to place gamma peak around channel 3500: _____ ns

REFERENCES

N. Abgrall et al. The MAJORANA DEMONSTRATOR neutrinoless double-beta decay experiment. *Adv. High Energy Phys.*, 2014:1–18, 2014. ISSN 1687-7357. doi: 10.1155/2014/365432. URL http://www.hindawi.com/journals/ahep/2014/365432/.

M. Agostini et al. Measurement of the half-life of the two-neutrino double beta decay of ^{76}Ge with the GERDA experiment. *J. Phys. G*, 40(3):035110, 2013. doi: 10.1088/0954-3899/40/3/035110.

Q. R. Ahmad et al. Direct evidence for neutrino flavor transformation from neutral-current interactions in the Sudbury Neutrino Observatory. *Phys. Rev. Lett.*, 89:011301, Jun 2002. doi: 10.1103/PhysRevLett.89.011301. URL http://link.aps.org/doi/10.1103/PhysRevLett.89.011301.

M. W. Ahmed, C. R. Howell, and A. S. Crowell. CODA at TUNL (C@T) and the TUNL Real-Time Analysis Package (TRAP). Technical report, TUNL, 2003.

J. B. Albert et al. Improved measurement of the $2\nu\beta\beta$ half-life of ^{136}Xe with the exo-200 detector. *Phys. Rev. C*, 89:015502, Jan 2014. doi: 10.1103/PhysRevC.89.015502. URL http://link.aps.org/doi/10.1103/PhysRevC.89.015502.

W. P. Alford et al. The $(^3He,n)$ reaction on n = 82 targets and even isotopes of neodymium. *Nucl. Phys. A*, 321(1):45–61, 1979a. ISSN 03759474. doi: 10.1016/0375-9474(79)90684-5.

W. P. Alford et al. The $(^3He,n)$ reaction on tellurium isotopes. *Nucl. Phys. A*, 323(2):339–348, 1979b. ISSN 03759474. doi: 10.1016/0375-9474(79)90114-3.

J. Argyriades et al. Measurement of the double-β decay half-life of ^{150}Nd and search for neutrinoless decay modes with the nemo-3 detector. *Phys. Rev. C*, 80:032501, Sep 2009. doi: 10.1103/PhysRevC.80.032501. URL http://link.aps.org/doi/10.1103/PhysRevC.80.032501.

R. Arnold et al. First results of the search for neutrinoless double-beta decay with the nemo 3 detector. *Phys. Rev. Lett.*, 95:182302, Oct 2005. doi: 10.1103/PhysRevLett.95.182302. URL http://link.aps.org/doi/10.1103/PhysRevLett.95.182302.

R. Arnold et al. Measurement of the $\beta\beta$ decay half-life of ^{130}Te with the nemo-3 detector. *Phys. Rev. Lett.*, 107:062504, Aug 2011. doi: 10.1103/PhysRevLett.107.062504. URL http://link.aps.org/doi/10.1103/PhysRevLett.107.062504.

F. T. Avignone, S. R. Elliott, and J. Engel. Double beta decay, Majorana neutrinos, and neutrino mass. *Rev. Mod. Phys.*, 80:481–516, Apr 2008. doi: 10.1103/RevModPhys.80.481. URL http://link.aps.org/doi/10.1103/RevModPhys.80.481.

R. H. Bassel et al. Analysis of the inelastic scattering of alpha particles. *Phys. Rev.*, 128(6):

2693–2707, 1962.

R. A. Battye and A. Moss. Evidence for massive neutrinos from cosmic microwave background and lensing observations. *Phys. Rev. Lett.*, 112(5), 2014. ISSN 00319007. doi: 10.1103/PhysRevLett.112.051303.

T. Bloxham et al. Pair correlations in the neutrinoless double-β decay candidate ^{130}Te. *Phys. Rev. C*, 82(2):27308, 2010. ISSN 05562813. doi: 10.1103/PhysRevC.82.027308.

D. M. Brink and R. A. Broglia. *Nuclear Superfluidity*. Cambridge University Press, Cambridge, UK, 2005.

Rene Brun and Fons Rademakers. ROOT An object oriented data analysis framework. *Nucl. Instrum. Meth. A*, 389(1-2):81–86, apr 1997. ISSN 01689002. doi: 10.1016/S0168-9002(97)00048-X. URL http://linkinghub.elsevier.com/retrieve/pii/S016890029700048X.

R. A. Cecil, B. D. Anderson, and R. Madey. Improved predections of neutron detection efficiency for hydrocarbon scintillators from 1 mev to about 300 mev. *Nucl. Instrum. Methods*, 161(3):439–447, 1979.

A. S. Crowell. *Cross-Section Measurements of Star Configurations in Neutron-Deuteron Breakup at 16.0 MeV*. PhD thesis, Duke University, 2001.

G. Danby et al. Observation of high-energy neutrino reactions and the existence of two kinds of neutrinos. *Phys. Rev. Lett.*, 9(1):36–44, jul 1962. ISSN 0031-9007. doi: 10.1103/PhysRevLett.9.36. URL http://link.aps.org/doi/10.1103/PhysRevLett.9.36.

R. Davis. Nobel lecture: A half-century with solar neutrinos. *Rev. Mod. Phys.*, 75(3):985–994, 2003. ISSN 00346861. doi: 10.1103/RevModPhys.75.985.

R. Davis, D. S. Harmer, and K. C. Hoffman. Search for neutrinos from the sun. *Physical Review Letters*, 20(21):1205–1209, 1968. ISSN 00319007. doi: 10.1103/PhysRevLett.20.1205.

G. Dietze and H. Klein. Technical report ptb-nd-22. 1982a.

G. Dietze and H. Klein. Gamma-calibration of ne 213 scintillation counters. *Nucl. Instrum. Methods*, 193(3):549–556, 1982b. doi: 10.1016/0029-554X(82)90249-X. URL https://www.scopus.com/inward/record.uri?eid=2-s2.0-0020102663&partnerID=40&md5=9936046528b61fd2f57bdb42061fe64b. cited By 133.

M. Drosg and O. Schwerer. *Production of monoenergetic neutrons between 0.1 and 23 MeV*, volume 18. IAEA, 1987. ISBN 9201350872.

B. A. D'yachkov and V. I. Zinenko. High-intensity source of He^- ions. *Sov. Phys. - Tech. Phys.*, 16(2):305–306, 1971.

L. P. Ekstrom and R. B. Firestone. Www table of radioactive isotopes. http://ie.lbl.gov/toi/index.htm, 2004.

J. L. Elliot et al. The recent expansion of Pluto's atmosphere. *Nature*, 424(6945):165–8, 2003. ISSN 1476-4687. doi: 10.1038/nature01762. URL http://www.ncbi.nlm.nih.gov/pubmed/12853949.

S. R. Elliott et al. Direct evidence for two-neutrino double-beta decay in ^{82}Se. *Phys. Rev. Lett.*, 59:2020–2023, Nov 1987. doi: 10.1103/PhysRevLett.59.2020. URL http://link.aps.org/doi/10.1103/PhysRevLett.59.2020.

J. Engel and J. Menéndez. Status and future of nuclear matrix elements for neutrinoless double-beta decay: A review. *arXiv preprint arXiv:1610.06548*, 2016.

E. Fermi. Nuclear physics. In *A course given by Enrico Fermi at the University of Chicago, 1949, Chicago: University of Chicago Press, 1950, Rev. ed.*, volume 1, 1950.

H. W. Fielding et al. Two-proton transfer near Z = 40. *Nucl. Phys. A*, 269(1):125–137, 1976. ISSN 03759474. doi: 10.1016/0375-9474(76)90401-2.

S. J. Freeman and J. P. Schiffer. Constraining the $0\nu2\beta$ matrix elements by nuclear structure observables. *J. Phys. G*, 39(12):124004, 2012. ISSN 0954-3899. doi: 10.1088/0954-3899/39/12/124004. URL http://stacks.iop.org/0954-3899/39/i=12/a=124004?key=crossref.bcae90e2d9254862e91064c3750da055.

Y. Fukuda et al. Evidence for oscillation of atmospheric neutrinos. *Phys. Rev. Lett.*, 81:1562–1567, Aug 1998. doi: 10.1103/PhysRevLett.81.1562. URL http://link.aps.org/doi/10.1103/PhysRevLett.81.1562.

M. Goeppert-Mayer. Double beta-disintegration. *Phys. Rev.*, 48:512–516, Sep 1935. doi: 10.1103/PhysRev.48.512. URL http://link.aps.org/doi/10.1103/PhysRev.48.512.

D.E. Gonzlez-Trotter et al. Neutron detection efficiency determinations for the TUNL neutronneutron and neutronproton scattering-length measurements. *Nucl. Instrum. Methods*, 599(23):234 – 242, 2009. ISSN 0168-9002. doi: http://dx.doi.org/10.1016/j.nima.2008.10.036. URL http://www.sciencedirect.com/science/article/pii/S0168900208015878.

R. Henning. Current status of neutrinoless double-beta decay searches. *Reviews in Physics*, 1:29 – 35, 2016. ISSN 2405-4283. doi: http://dx.doi.org/10.1016/j.revip.2016.03.001. URL http://www.sciencedirect.com/science/article/pii/S2405428316000034.

J. Högaasen-Feldman. A study of some approximations of the pairing force. *Nucl. Phys.*, 28:258–269, 1961.

C. R. Howell. *Neutron Scattering from ^{28}Si and ^{32}S: Cross Sections and Analyzing Powers from 8 to 40 MeV*. PhD thesis, Duke University, 1984.

H. Johnstad. Physics Analysis Workstation. *IEEE Transactions on Nuclear Science*, 36 (5):1568–1571, 1989. ISSN 00189499. doi: 10.1109/23.41103. URL http://ieeexplore.ieee.org/document/41103/.

G. F. Knoll. *Radiation detection and measurement*. John Wiley & Sons, 2010.

K. Kodama et al. Observation of tau neutrino interactions. 2001.

K. S. Krane. *Introductory Nuclear Physics*. John Wiley & Sons, New York, USA, 1987.

J. G. Learned et al. Hanohano: A deep ocean anti-neutrino detector for unique neutrino physics and geophysics studies. *arXiv Preprint*, pages 1–42, 2008. URL http://arxiv.org/abs/0810.4975v1.

C. Lejeune. Theoretical and experimental study of the duoplasmatron ion source. *Nucl. Instrum. Meth.*, 116(3):417–428, apr 1974a. ISSN 0029554X. doi: 10.1016/0029-554X(74)90821-0. URL http://linkinghub.elsevier.com/retrieve/pii/0029554X74908210.

C. Lejeune. Theoretical and experimental study of the duoplasmatron ion source. *Nucl. Instrum. Meth.*, 116(3):429–443, apr 1974b. ISSN 0029554X. doi: 10.1016/0029-554X(74)90822-2. URL http://linkinghub.elsevier.com/retrieve/pii/0029554X74908222.

E Majorana. Symmetrical theory of electrons and positrons. *Nuovo Cimento*, 14:171–184, 1937.

R. McKeown et al. Report to the nuclear science advisory committee: Neutrinoless double beta decay. (unpublished), 2014. URL http://science.energy.gov/~/media/np/nsac/pdf/docs/2014/NLDBD_Report_2014_Final.pdf.

W. T. Milner. Double-Drift Beam Bunching Systems. *IEEE Transactions on Nuclear Science*, 26(1):1445–1449, feb 1979. ISSN 0018-9499. doi: 10.1109/TNS.1979.4330407. URL http://ieeexplore.ieee.org/document/4330407/.

R. N. Mohapatra and G. Senjanović. Neutrino mass and spontaneous parity nonconservation. *Phys. Rev. Lett.*, 44:912–915, Apr 1980. doi: 10.1103/PhysRevLett.44.912. URL http://link.aps.org/doi/10.1103/PhysRevLett.44.912.

A H F Muggleton. Preparation of thin nuclear targets. *J. Phys. E*, 12(9):780–807, sep 1979. ISSN 0022-3735. doi: 10.1088/0022-3735/12/9/001. URL http://stacks.iop.org/0022-3735/12/i=9/a=001?key=crossref.2f1e6f92aca845eaf6d8458dcf7be07c.

G Potel et al. Cooper pair transfer in nuclei. *Rep. Prog. Phys.*, 76(10):106301, oct 2013. ISSN 0034-4885. doi: 10.1088/0034-4885/76/10/106301. URL http://stacks.iop.org/0034-4885/76/i=10/a=106301?key=crossref.7bfd289cf22e760a9d32402c9d2e2afe.

G. Racah. Symmetry between particles and anti-particles. *Nuovo cimento*, 14:322–328, 1937.

F. Reines and C. L. Cowan. The neutrino. *Nature*, 178(4531):446–449, 1956.

F. Reines and C. L. Cowan. The reines-cowan experiments: detecting the poltergeist. *Los Alamos Science*, (25):4–6, 1997.

T. C. R. Rhea. *Polarization and Cross-Section Studies of the* $^{12}C(^3He,n_o)$ *and* $^{13}C(^3He,n_o)$ *Nuclear Reactions and of* $^{13}C(^3He,^3He)$ *Elastic Scattering*. PhD thesis, Duke University, 1973.

A. Roberts et al. Proton pair correlations and the neutrinoless double-β decay of ^{76}Ge. *Phys. Rev. C*, 87(5):51305, 2013. ISSN 05562813. doi: 10.1103/PhysRevC.87.051305.

J.J. Sakurai and J. Napolitano. *Modern Quantum Mechanics*. Addison-Wesley, San Francisco, USA, 2011.

J. Schechter and J. W. F. Valle. Neutrinoless double-β decay in su(2)xu(1) theories. *Phys. Rev. D*, 25:2951–2954, Jun 1982. doi: 10.1103/PhysRevD.25.2951. URL http://link.aps.org/doi/10.1103/PhysRevD.25.2951.

D. D. Stancil et al. Demostration of communication using neutrinos. *Mod. Phys. Lett. A*, 27 (12):1250077, 2012. ISSN 0217-7323. doi: 10.1142/S0217732312500770. URL http://www.scopus.com/inward/record.url?eid=2-s2.0-84859365414{&}partnerID=tZOtx3y1.

M. P. Stockli. Adaptation of dependex fittings to International Standards Organization fittings. *Journal of Vacuum Science & Technology A: Vacuum, Surfaces, and Films*, 7(5): 3124, sep 1989. ISSN 07342101. doi: 10.1116/1.576326. URL http://scitation.aip.org/content/avs/journal/jvsta/7/5/10.1116/1.576326.

J. Suhonen and O. Civitarese. Effects of orbital occupancies and spinorbit partners on $0\nu\beta\beta$-decay rates. *Nucl. Phys. A*, 847(3-4):207–232, dec 2010. ISSN 03759474. doi: 10.1016/j.nuclphysa.2010.08.003. URL http://linkinghub.elsevier.com/retrieve/pii/S0375947410006305.

Inboard Helieum Leak Test of 316 Stainless Steel Swagelok Tube Fittings at Cryogenic Temperature. Swagelok Company, 8 2008. URL hhttp://www.swagelok.de/downloads/WebCatalogs/EN/PTR_1369.PDF.

VCR Metal Gasket Face Seal Fittings. Swagelok Company, 2016. URL https://www.swagelok.com/downloads/webcatalogs/EN/MS-01-24.PDF.

I. J. Thompson. Coupled reaction channels calculations in nuclear physics. *Computer Physics Reports*, 7(4):167 – 212, 1988. ISSN 0167-7977. doi: http://dx.doi.org/10.1016/0167-7977(88)90005-6. URL http://www.sciencedirect.com/science/article/pii/0167797788900056.

I. J. Thompson. Reaction mechanisms of pair transfer. *Fifty Years of Nuclear BCS: Pairing in Finite Systems*, page 455, 2013.

P. Vogel. Nuclear physics aspects of double beta decay. pages 1–55, 2008. URL http://arxiv.org/abs/0807.2457.

P. Vogel. Anatomy of double beta decay nuclear matrix elements. *J. Phys.: Conference Series*, 173:012010, 2009. ISSN 1742-6596. doi: 10.1088/1742-6596/173/1/012010. URL http://stacks.iop.org/1742-6596/173/i=1/a=012010?key=crossref.6b3f7c8ccf14e78bdc048a1965fed247.

S. A. Wender et al. A high efficiency bunching system for polarized beams. *Nucl. Instrum. Methods*, 174(3):341–347, 1980. ISSN 0029554X. doi: 10.1016/0029-554X(80)91083-6.

S. E. Woosley and A. Heger. Nucleosynthesis and remnants in massive stars of solar metallicity. *Phys. Rep.*, 442(1):269–283, 2007.

I. Zawisza. Evaporation procedure. (unpublished), 2012.

K. Zuber. *Neutrino Physics*. CRC Press, Boca Raton, USA, 2012.